5-2019

Experimental Study of Condensation in Different 3D Printed Regenerators in a Thermoacoustic Cooler

Aibek Bekkulov

The University of Texas Rio Grande Valley

Recommended Citation

Bekkulov, Aibek, "Experimental Study of Condensation in Different 3D Printed Regenerators in a Thermoacoustic Cooler" (2019). *Theses and Dissertations*. 412.
https://scholarworks.utrgv.edu/etd/412

EXPERIMENTAL STUDY OF CONDENSATION IN DIFFERENT 3D PRINTED REGENERATORS IN A THERMOACOUSTIC COOLER

A Thesis

by

AIBEK BEKKULOV

Submitted to the Graduate College of
The University of Texas Rio Grande Valley
In partial fulfillment of the requirements for the degree of

Master Of Science in Engineering

May 2019

Major Subject: Mechanical Engineering

EXPERIMENTAL STUDY OF CONDENSATION IN DIFFERENT 3D PRINTED REGENERATORS IN A THERMOACOUSTIC COOLER

A Thesis
by
AIBEK BEKKULOV

COMMITTEE MEMBERS

Dr. Ben Xu
Chair of Committee

Dr. Stephen Crown
Committee Member

Dr. Yingchen Yang
Committee Member

Dr. Isaac Choutapalli
Committee Member

May 2019

ABSTRACT

Bekkulov, Aibek, Experimental study of condensation in different 3d printed regenerators in a thermoacoustic cooler. Master of Science in Engineering (MSE), May, 2019, 111 pp., 23 tables, 103 figures, references, 42 titles.

Thermoacoustics (TA) deals with the conversion of heat into sound and vice versa. Device that converts heat into acoustic work is called TA heat engine, while the device that transfers energy from a low temperature reservoir to a high temperature one by utilizing acoustic work is called TA cooler. A simple construction of TA cooler includes an acoustic speaker, a resonator tube and a regenerator stack in which the temperature gradient is being imposed. Such a TA cooler has several advantages over traditional compression/expansion cooling machine such as its simplicity of the construction, high reliability and lack of toxic refrigerants. Operating on air as the working fluid at standard atmospheric pressure, a standing wave thermoacoustic cooler was built to investigate water condensation enhancement when compared with a reference system without TA phenomena. Also, three different 3D printed stacks were used in the experiments to analyze the correlation between their performances and geometries.

DEDICATION

I dedicate this thesis to my family, without their constant support and words of encouragement my academic path would not be feasible. Thank you for always being my personal beacon in life.

ACKNOWLEDGMENTS

I immensely thankful to Dr. Ben Xu, chair of my thesis committee, for all his mentoring, support and advice. From the initial idea to the analysis of the experimental results he guided me with great level of professional expertise and infinite patience. I wholeheartedly thank my dissertation committee members: Dr. Stephen Crown, Dr. Yingchen Yang and Dr. Isaac Choutapalli. Their advice, input, and comments on my dissertation helped to ensure the quality of my intellectual work. I want to express my deepest gratitude to the UTRGV and the mechanical engineering department for allowing me to conduct my research and providing any assistance requested. I also give a special thanks to associates from our lab for all the time we spent working together and all the valuable contribution for the experimental part of my work. I am grateful for all my teachers and professors whose student I had honor to be in different time periods, in different schools, countries and continents, for the obtained knowledge and capability to design and conduct such research.

TABLE OF CONTENT

LIST OF TABLES

LIST OF FIGURES

CHAPTER I

INTRODUCTION

1.1 Motivation

In 2010, Tetra Tech prepared a report (Corbett, Harter and Sneed 2011) with a countrywide analysis using annual water use data at the U.S. county level and using global climate model outputs for temperature and precipitation, both projected 20-40 years into the future. The prediction made in the report stated that under the business-as-usual scenario of demand growth, water supplies in 70% of counties in the U.S. may be at risk due to climate change, and approximately one-third of counties may be at high or extreme risk of demanding an unsustainable water supply.

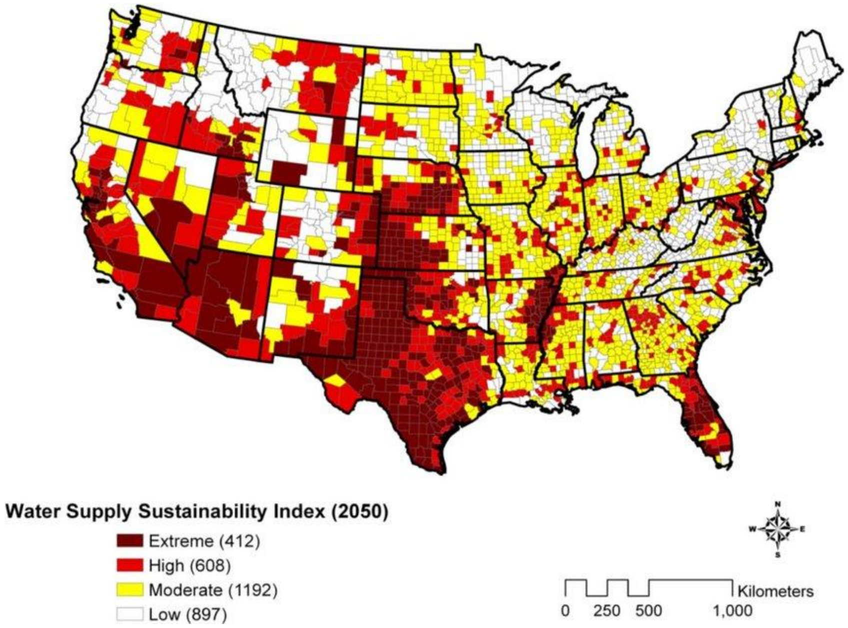

Figure 1: Water Sustainability Index by 2050 (Corbett, Harter and Sneed 2011)

Therefore, there is a significant demand to develop new ways of providing water to the most affected areas which are, not surprisingly, in the arid zones mostly in the southern part of USA. The proposed approach was to investigate the concept of water harvesting from the air. Thus, as one of the routes to harvest the water from the air is to simply condensate the water vapor on the cold surface, and the use of thermoacoustic engines was considered.

1.2 Background

Thermoacoustic engines (TA engines) are the class of devices that utilize acoustic waves to pump heat from one place to another or contrariwise creates an acoustic wave from the applied temperature gradient. One of the categories of such TA devices is thermoacoustic cooler (TAC), also known as thermoacoustic refrigerator (TAR), where the acoustic power is used to pump heat from a low temperature source to a high temperature sink, according to Swift (Swift 1988). TACs found its niche applications in various peculiar projects from small and medium scale experimental research cryogenic apparatuses to commercial gas liquefiers (Hou, et al. 2018).

Thermoacoustic coolers possess number of advantages over traditional refrigeration technologies. Such advantages include mechanical simplicity of the construction, usage of non-hazardous inert gases, almost no moving parts and high reliability coupled with little to no maintenance (Yu, Dai and Luo 2010). Therefore, as such system can create a temperature gradient due to heat pumping, it can be used in different applications. For instance, thermoacoustic engine that utilizes a heat from solar energy to create an acoustic wave coupled with a TAC that utilizes such acoustic wave to create a temperature gradient, has a potential to be used for autonomous water harvesting in sparsely populated areas like deserts. Such TAC coupled with another TA engine that supplies it with an acoustic power is called thermoacoustic driven thermoacoustic cooler, or TADTAC (Babaei and Siddiqui 2008). Another similar application based on forced condensation in virtue of TA enabled temperature gradient could be a dehumidifier.

In general, as shown in Figure 2, TAC contains three main components for the use of thermoacoustic phenomena to generate cooling power: an acoustic speaker, a resonator tube filled with gas and a stack of plates along which, due to thermal interaction between oscillating gas undergoing compression/expansion cycles and the surface of the plates, the temperature gradient is created (Kang, Zhou and Li 2010).

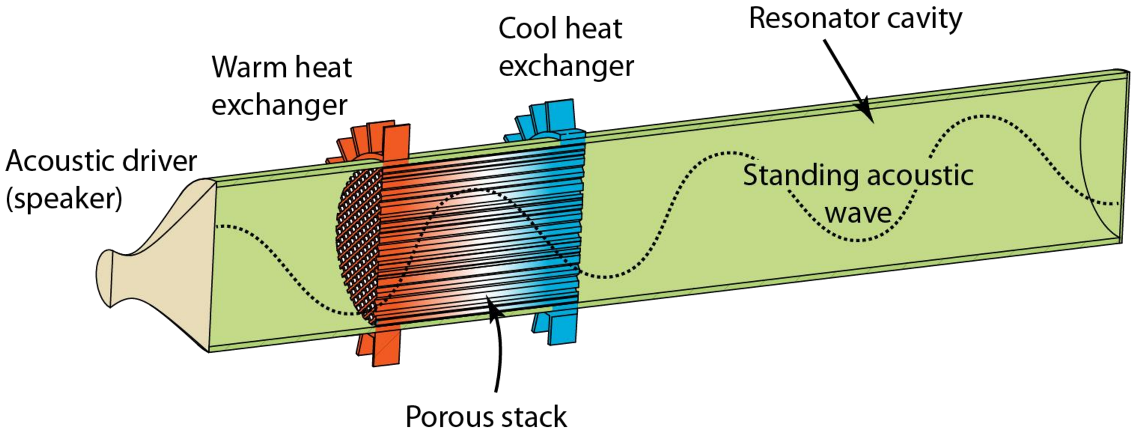

Figure 2: An illustration of half-wavelength standing-wave TAC (Jordan 2017)

The aim of this work was to build a TAC using humid air as the working fluid and by conducting a set of experiments analyze a possible condensation enhancement due to thermoacoustic phenomena in cooler. Also, as the stack is one of the most important key components of TAC and paramount for obtaining temperature gradient, three stacks with different geometries were produced to experimentally observe the effect of stack design on TAC performance and condensation rate. Therefore, the entire project was divided into two stages:

- Design and build a working TAC
- Conduct experiments with different stacks to analyze TAC performance and condensation rate.

1.3 Thermoacoustic principle

An interaction between pressure, displacement and temperature oscillations in a gas, caused by an acoustic wave, in the proximity of solid surface produces thermoacoustic oscillations and thus thermoacoustic phenomena occurs (Atis, Sarker and Ehsan 2014). Consequently, the heat from the gas can be absorbed by the surface or oppositely the surface can supply the heat to the gas. Therefore, thermoacoustic engines can be divided into two categories:

- Prime movers (convert temperature gradient into acoustic power)
- Heat pumps (convert acoustic wave into temperature gradient)

Another name for the heat pump is the thermoacoustic cooler. Figure 3 provides schematics to display the difference between two.

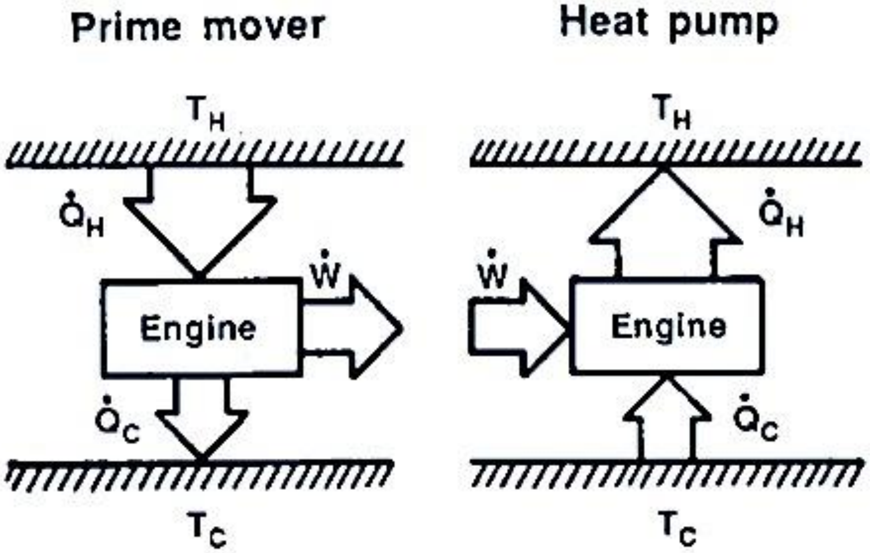

Figure 3: Types of TA engines (Swift 1988)

One of the simplest variations of the TAC is a standing wave thermoacoustic cooler. As it follows from its name, there is a standing acoustic wave that drives the whole process. In general, there two types of standing wave TAC: half-wavelength and quarter-wavelength depending whether the length of the resonator set to be equal to half or quarter of the acoustic standing wavelength (Babaei and Siddiqui 2008). Consequently, there are two crucial conditions important for its proper operation (Backhaus and Swift 1999):

- Pressure should lag the velocity by 90° phase (determined by standing wave acoustic field).
- The imperfect thermal contact between the gas and the solid plates in stack to separate the compression/expansion of the gas from heating and cooling of the solid surface.

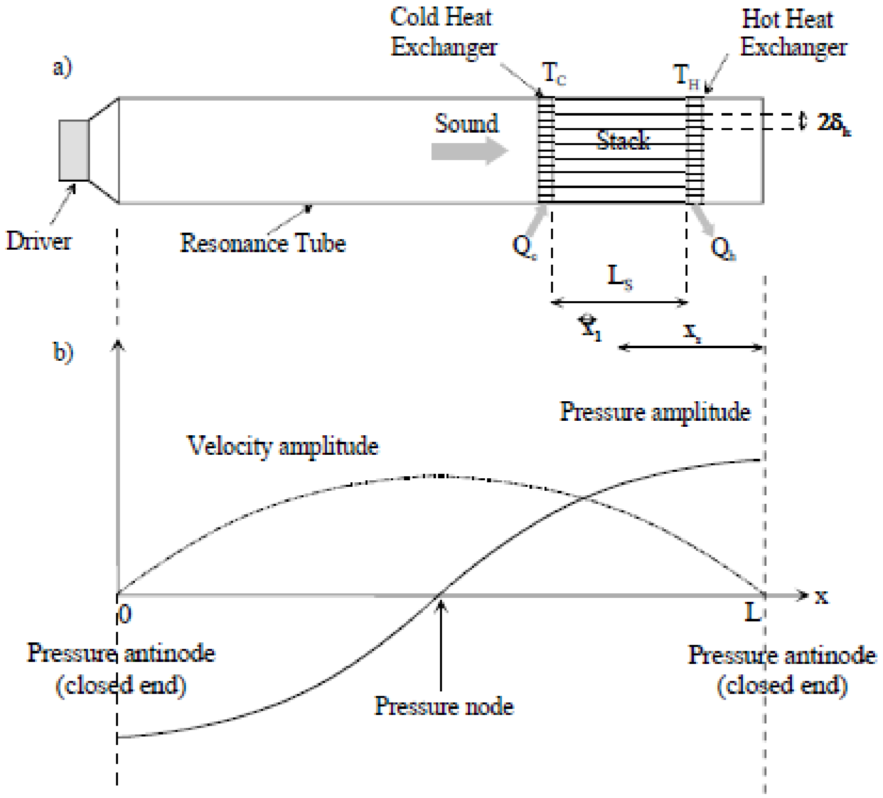

Figure 4: Standing wave TAC schematic (Jinshah, Ajith Krishnan and Eep 2013)

Figure 4 illustrates half-wavelength standing wave TAC (part a) and the phase lag between pressure and velocity (part b). Stack consists of two heat exchangers (T_c and T_H) attached to hot (left) and cold (right) sides. L_s and x_s correspond to the length and position of the stack. δ_k is a thermal penetration depth, a quantity that characterizes the level of thermal contact between the gas and the solid plate in the stack. These parameters are discussed in more details later in this work.

To understand how the thermoacoustic cycle works, small volume of gas (parcel) motion can be tracked alongside the solid surface. Such motion of gas parcel can be represented with the help of analogy as expansion/compression and corresponding heating/cooling of the gas in the moving piston inside the cylinder example (the acoustic wave is an analogue of the piston) provided in Figure 5.

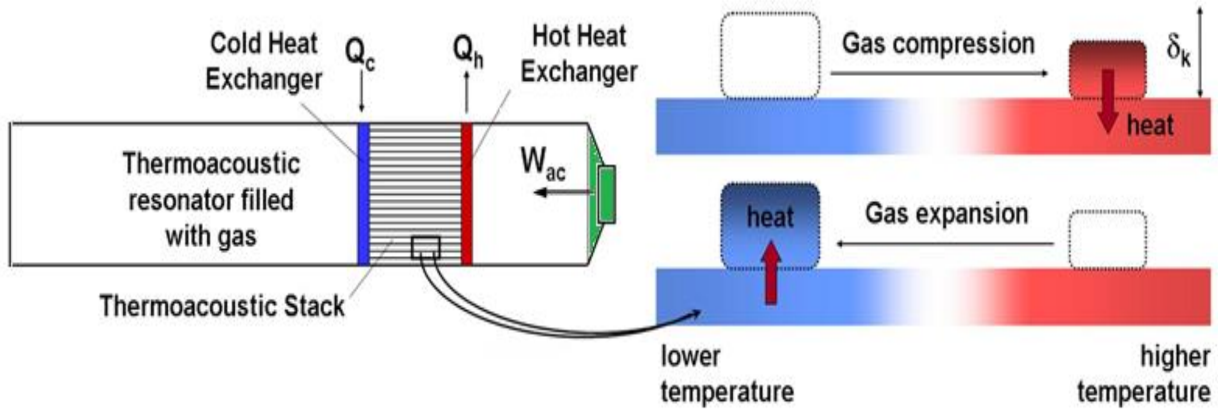

Figure 5: Half-wavelength TAC gas compression/expansion (Jaworski n.d.)

The thermodynamic cycle of thermoacoustic phenomena is the reversed Brayton cycle (Jin, et al. 2015). Figure 6 demonstrates this cycle, where step 1-2 and step 3-4 are reversible adiabatic steps, and step 2-3 and step 4-1 are two isobaric heat transfer steps.

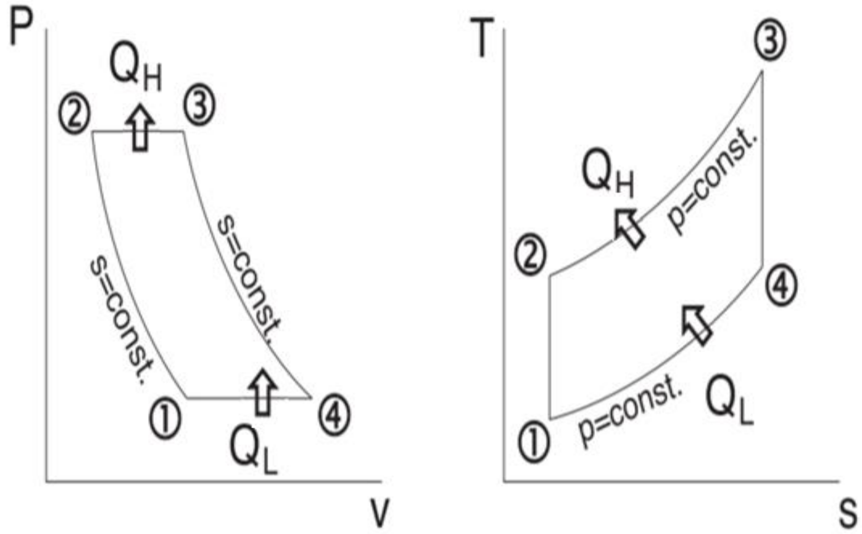

Figure 6: Reversed Brayton cycle (Culham 2011)

In more details, the gas and the wall initially have the same temperature. Then, when the acoustic wave (piston) supplied, the cycle begins:

- Step 1-2: Gas parcel is being compressed and thus heats. The temperature of the gas is higher than the temperature of the wall $T_g(x) > T_w(x)$.
- Step 2-3: The heat is irreversibly transferring from the gas to the wall.
- Step 3-4: Gas parcel expands and cools. The temperature of the gas is lower than the temperature of the wall $T_g(x) < T_w(x)$.
- Step 4-1: The heat flows from the wall to the gas. The cycle starts all over again.

However, as it was mentioned before, one of the important conditions for the proper operation of TAC is its imperfect thermal contact between the gas and plate. Also, as the stack of such plates is the actual component in the TAC where the temperature gradient is obtained, there are a few important concepts that need to be mentioned:

- Not all the gas in the tube is equally effective to the TA effect.

- Gas particles far away from the wall have no thermal contact and are simply compressed and expanded adiabatically and reversibly by the sound wave.
- Gas particles too close to the wall have a good thermal contact and are simply compressed and expanded isothermally.
- Gas particles at about the distance of a thermal penetration depth δ_k from the wall, have enough thermal contact to exchange some heat with the wall and thus produce a lag between motion and heat transfer which is necessary for the heat pump process. Figure 7 provides visual schematic to understand this concept.

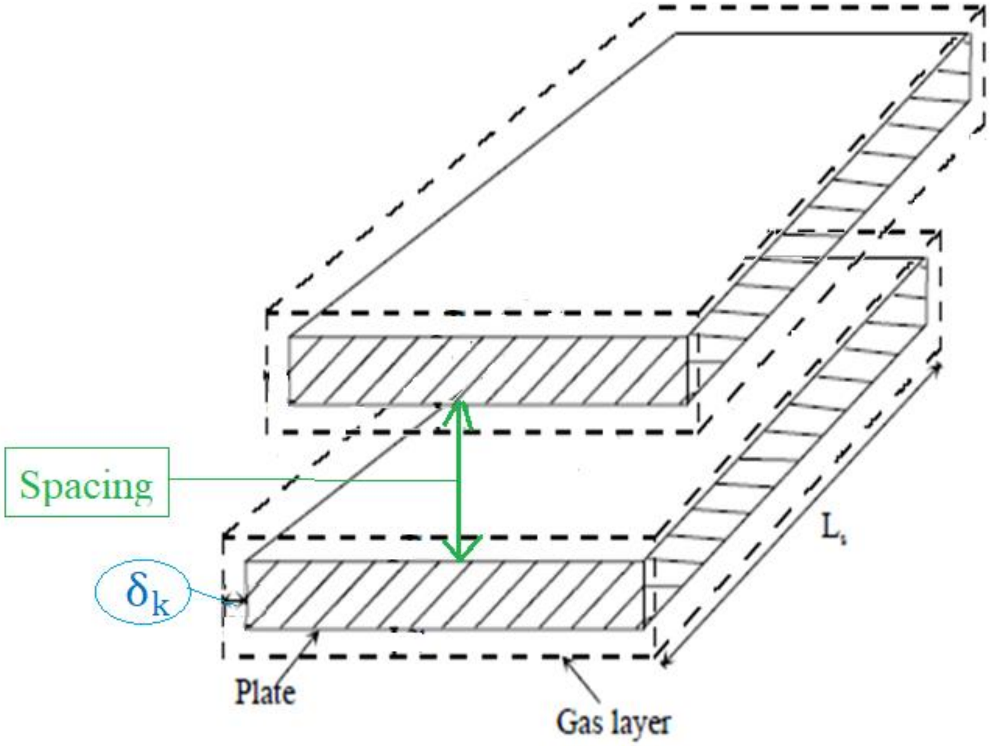

Figure 7: Schematic of the stack's plates (Jinshah, Ajith Krishnan and Eep 2013)[1]

---

[1] Modified from the reference

1.4 Relative Humidity

Relative Humidity can be simply defined as the percentage amount of water in the air relative to the saturation amount the air can hold at the given temperature (Relative Humidity 2019)

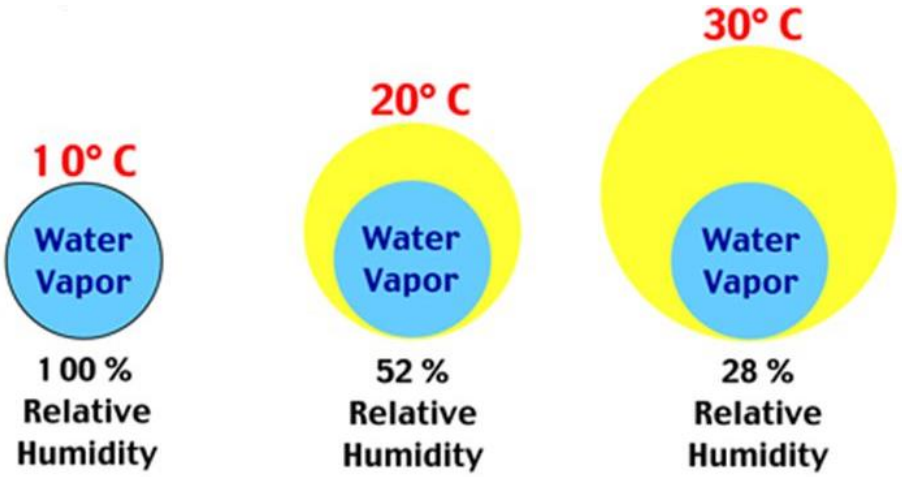

Figure 8: Relative Humidity (Relative Humidity 2019)

Therefore, to condense water from the air, the temperature should be lower to the saturation point (or to the point when RH becomes 100%). For the lab air, the saturation temperature (also known as dew point) was approximately about 14°C and the lowest temperature that was achieved in the built experimental TAC in this research was around 17°C. Thus, for this work, it was decided to use an additional humidifier to increase the humidity of air that could facilitate to achieve noticeable condensation and provide more accurate data for analysis.

CHAPTER II

THERMOACOUSTIC COOLER DESIGN

2.1 Thermoacoustic cooler design overview

In this work, the TAC was built to experimentally investigate possible water harvesting/dehumidification performance. As the TAC was built to be studied in the lab, it was decided to use speaker as the source of acoustic wave for the experimental purposes, instead of developing a solar-thermal-driven TAE. The TAC design was based on the same strategy of reducing the number of parameters using dimensionless parameters as did by Tijani and his team in 2001 (Jina, et al. 2015). In general, it was claimed that the gas with high ratio of specific heat and lower value of Prandtl number improves the performance of TAC (Ke, et al. 2012) and thus many TACs are built using gas mixtures or some inert gases like helium or argon. In fact, in most of the practical application of TACs or TARs, the working fluid is Helium or Helium-Xeon (Tasnim, Mahmud and Fraser 2012). It is typical for a high-performance TAC to be operated at charged pressure (Kalra, et al. 2015). However, for the sake of simplicity and as the practical applications for the experimental TAC were considered water harvesting and dehumidifier, the air under normal conditions (room temperature and atmospheric pressure) was chosen as the working gas. The choice for components design was restricted by the availability of materials. For instance, the stack was decided to be 3D printed as it allowed to create three different geometries. Also, the advantage of using 3D printed stack over alternative such as hand-fabricated Mylar or ready-made

Celcor Ceramic was recently proved by Universiti Teknologi Malaysi research team (Zolpakar, et al. 2017). However, the thickness of the plates and the spacing between them were limited by the printing resolution. Consequently, the length of the resonator was specified as half-wavelength of the acoustic wave as it allowed to use lower sound frequency and thus wider spacing between plates in the 3D printed stack. Thermal insulation (mineral wool) was chosen to use as the cover for the system to minimize the heat loss and sound loss due to vibration.

2.2 Thermoacoustic cooler design parameters – speaker and resonator

The experimental TAC was designed according to the materials available on the market. Prior to the final design, several prototypes were made and tested to obtain enough practical experiences. Figure 9 illustrates the schematic of the finalized TAC that was built for this study.

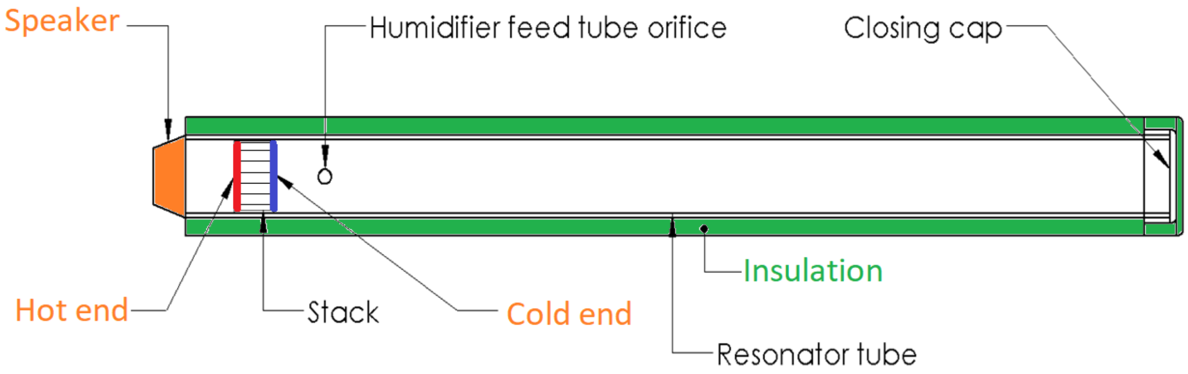

Figure 9: Final TAC design schematic

Several types of speakers including Bluetooth speakers were rejected prior to the final design since either not powerful enough, having overheating problem when put in the continuous playing mode or poor range of operating frequency (as it appeared that the final design TAC required relatively low frequency). In the end, the car speaker connected to an amplifier was chosen by satisfying three requirements: to be powerful, to be able to operate long time without shutting down due to overheating and to have a convenient range of operating frequency. The specifications for the speaker are given in the Table 1 below.

Table 1: Car speaker and amplifier specifications

	Speaker	Amplifier
Name	BOSS P45.4C	AOSHIKE
Max Power	125W RMS	100 W (2 channels)
Nominal Impedance	4 Ω	-
Voltage		8-25V
Frequency Response	85 Hz-20 kHz ±3 dB	-
Sound Pressure Level (SPL)	83 dB	-

The resonator was build using 5-ft 4’’ PVC pipe and, knowing air properties in the lab, the operating frequency to create a standing wave in the half-wavelength configuration was found.

$$Operating\ frequency, f = 0.5\frac{speed\ of\ air}{resonator\ length} \tag{2.1}$$

The parameters for the resonator and air properties are presented in the Table 2 and Table 3 correspondingly.

Table 2: Resonator parameters

PVC pipe (length)	1.52 m (5 ft)
PVC pipe (diameter)	0.10 m (4’’)
PVC pipe (working temperature ranges)	0-60°C (32-140 F)
Operating frequency (*f*)	110 Hz

Table 3: Air properties

Lab air temperature	22-23°C
Lab relative humidity (RH)	60%
Speed of air (a_{air})	344
Wavelength, λ (half-wavelength, 0.5λ)	3.12 m (1.56 m)
Angular velocity of sound wave (ω_{wave})	$2\pi f$ (691.15 rad/s)
Thermal conductivity of air (k_{air})	0.02624 $\mathrm{W/m \cdot K}$
Air density (ρ_{air})	1.2 $\mathrm{kg/m^3}$
Air dynamic viscosity (μ_{air})	0.000018 $\mathrm{Pa \cdot s}$
Isobaric specific heat capacity of air ($C_{p_{air}}$)	1010 $\mathrm{J/kg \cdot K}$

Isochoric specific heat capacity of air ($C_{v_{air}}$)	718 $\mathrm{J/kg \cdot K}$
Air heat capacity ratio (γ_{air})	1.4

There was a concern that the TAC was designed based on the dry air properties, the humid air provided by humidifier could drastically change the behavior of the system. In general, at the same pressure humid air has lower density than the dry air (Legg 2017). However, as the average operating temperatures was assumed to be around ambient air temperature in the lab, according to Figure 10, there is a negligible difference between dry and humid air at such temperature. Therefore, it was assumed that it was safe to use dry air properties for the system design and for both dry and humid air cases.

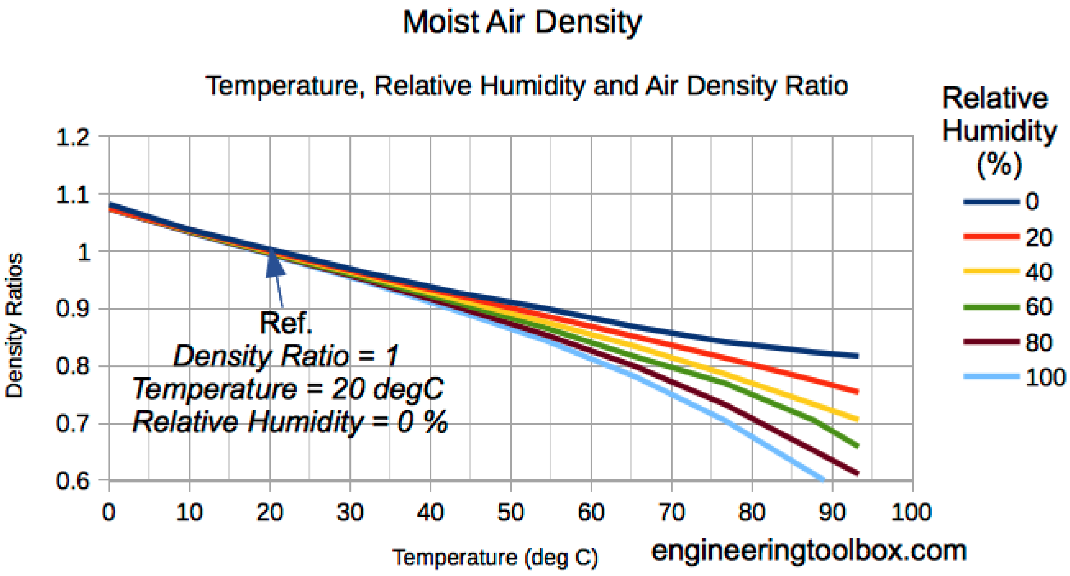

Figure 10: Moist and dry air density (Engineering ToolBox 2004)

Also, it is important to notice that the operating frequency was recalculated from 113 Hz (theoretical) to 110 Hz (practical) after the system was assembled, and it appeared that the distance between the speaker and the bottom of the closing cap was slightly bigger than the resonator itself due to the layer of adhesive material used to connect speaker to the resonator body and the parabolic bottom of the closing cap (Figure 11).

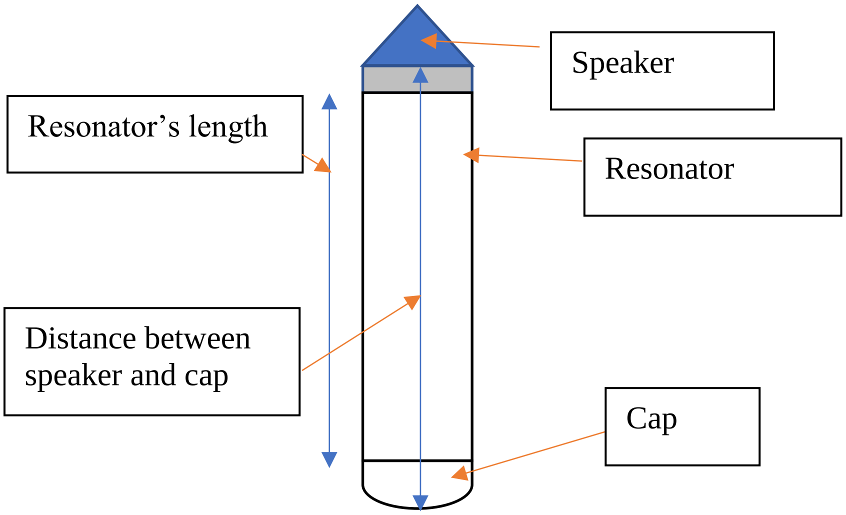

Figure 11: Difference between theoretical and practical resonator length in TAC

2.3 TAC design parameters – stack

The initial stack design was chosen to consist a number of parallel plates. The stack's position, length and the spacing between the plates were calculated through the same approach of using boundary layer and short-stack approximation as discussed in Tijani's paper (Tijani, Zeegers and De Waele 2002):

- The acoustic field is assumed to not be disturbed by the presence of the stack as the stack's length (L_s) is much smaller than the reduced acoustic wave ($\lambda/2\pi$).
- Rott's functions can be simplified (complex hyperbolic tangents set to be equal to one) with the assumption that spacing between the parallel plates is greater than both thermal and viscous penetration depths (δ_k, δ_v correspondingly).

- The gas properties inside the system are assumed to remain constant as the temperature changes are small compared to an average temperature.

Therefore, in order to choose the optimal length and position of the stack (L_{stack} and x_{stack} respectfully), the set of governing parameters was normalized. The position of the stack represents a distance between the speaker and the center of the stack, and it can be normalized with the length of the stack (x_{stack_n} and L_{stack_n} respectfully) via wavenumber ($2\pi/\lambda$):

$$x_{stack_n} = x_{stack}\left(\frac{2\pi}{\lambda}\right) \tag{2.2}$$

$$L_{stack_n} = L_{stack}\left(\frac{2\pi}{\lambda}\right) \tag{2.3}$$

The spacing between parallel plates (ss_{stack}) depends on the thermal penetration depth (δ_k). Other two important thermodynamic parameters that are linked with the thermal penetration depth are the viscous penetration depth (δ_v) and Prandtl number (Pr).

$$\delta_k = \sqrt{\frac{2k_{air}}{\rho_{air}C_{p_{air}}\omega_{wave}}} \tag{2.4}$$

$$\delta_v = \sqrt{\frac{2\mu_{air}}{\rho_{air}\omega_{wave}}} \tag{2.5}$$

$$Pr = \left(\frac{\delta_v}{\delta_k}\right)^2 \tag{2.6}$$

Typically, to not affect the acoustic field, the spacing between parallel plates is chosen to be between $2\delta_k$ and $4\delta_k$ (Wheatley, et al. 1985). For the manufactured stack, the spacing was selected to be $3\delta_k$.

$$ss_{stack} = 3\delta_k \tag{2.7}$$

The half spacing (y_0) was taken for normalization of thermal penetration depth (δ_{k_n}).

$$y_0 = 0.5(ss_{stack}) \tag{2.8}$$

$$\delta_{k_n} = \frac{\delta_k}{y_0} \tag{2.9}$$

Furthermore, each plate has a thickness (t_{plate}) that depends on the material and manufacturing technique used. In this study, Tornedo 3D printer was used for producing the stack. It had 0.5 mm layer resolution and used PLA as a printing material (it is easy to print from PLA and it has low thermal conductivity (SD3D.com 2017) which is important to sustain temperature gradient along the stack). Therefore, the blockage ratio or porosity (B_{stack}) could be calculated knowing the thickness of the plate and a spacing.

$$B_{stack} = \frac{y_o}{y_0 + 0.5 t_{stack}} \tag{2.10}$$

Table 4 below contains calculated parameters for the air and stack.

Table 4: *Stack geometry and working gas (air) parameters.*

Thermal penetration depth (δ_k)	0.25 mm
Viscous penetration depth (δ_v)	0.21 mm
Prandtl number (σ)	0.7
PLA thermal conductivity (k_{PLA})	0.13 W/K·m
Spacing between plates (ss_{stack})	0.75 mm
Half spacing (y_0)	0.375 mm
Theoretical porosity of the stack (B_{stack})	0.6
Normalized thermal penetration depth (δ_{k_n})	0.667

2.4 Performance and optimization of the stack

Two key pressure parameters in thermoacoustic are mean pressure (p_m) and acoustic pressure (p_A). They play a vital role as they basically compressional energy stored in the fluid (Hou, et al. 2018) and thus directly correspond to the available acoustic power (Tang, et al. 2009). The ratio between them is called the drive ratio (D).

$$D = \frac{p_A}{p_m} \tag{2.11}$$

In the experiment, the mean pressure inside a resonator was assumed to be 1 bar as the air is not pressurized. Whereas the acoustic pressure could be found via acoustic Mach number (M).

$$p_A = M(\rho_{air})(a_{air})^2 \tag{2.12}$$

For gases, due to nonlinear effects, acoustic Mach number is limited and can be taken as 0.1 (Swift 1988). Because the TAC in the experiment was designed to operate with unpressurized air as a working gas, the temperature gradient and temperature drop on the cold end of the stack were not expected to be great. Therefore, temperature difference (ΔT_m) of 10 degrees between hot and cold end was expected to be reasonably good. Considering that the room temperature was around 22-23°C (295-296K), it was assumed to have something near 290K on the cold end (T_c) and 300K on the hot end (T_h). Correspondingly, the mean temperature (T_m) along the stack should be something close to 295K.

$$\Delta T_m = T_h - T_c \tag{2.13}$$

$$T_m = \frac{T_h + T_c}{2} \tag{2.14}$$

The temperature difference could be normalized via mean temperature.

$$\Delta T_{m_n} = \frac{\Delta T_m}{T_m} \tag{2.15}$$

The calculated design operating parameters are given in Table 5 below.

Table 5: *Design operating parameters.*

Mean pressure (p_m)	1 bar (101.33 kPa)
Acoustic pressure (p_A)	0.14 bar (14.35 kPa)
Acoustic Mach number (M)	0.1
Drive ratio (D)	0.141
Stack’s hot end temperature (T_h)	300K (27°C)
Stack’s cold end temperature (T_c)	290K (17°C)
Mean temperature along the stack (T_m)	295K (22°C)
Temperature difference (ΔT_m)	10K
Normalized temperature difference (ΔT_{m_n})	0.034

Then, in order to find optimal stack's length and position, the COP calculations should be performed and analyzed via different variants of stack's length and position. The COP can be basically found as a ratio between normalized heat flow (Q_n) and acoustic power (W_n).

$$Q_n = \frac{\delta_{k_n} D^2 \sin 2x_n}{8\gamma_{air}(1+\sigma)\Lambda} \left(\frac{\Delta T_{m_n} \tan x_n}{(\gamma_{air}-1) B_{stack} L_{stack_n}} \frac{1+\sqrt{\sigma}+\sigma}{1+\sqrt{\sigma}} - \left(1 + \sqrt{\sigma} - \sqrt{\sigma}\delta_{k_n}\right) \right) \tag{2.16}$$

$$W_n = \frac{\delta_{k_n} L_{stack_n} D^2}{4\gamma_{air}} \left[(\gamma_{air} - 1) B_{stack} \cos^2 x_n \left(\frac{\Delta T_{m_n} \tan x_n}{(\gamma_{air}-1) B_{stack} L_{stack_n} (1+\sqrt{\sigma})\Lambda} - 1 \right) - \frac{\sqrt{\sigma} \sin^2 x_n}{B\Lambda} \right] \tag{2.17}$$

where

$$\Lambda = 1 - \sqrt{\sigma}\delta_{k_n} + \frac{1}{2}\sigma\delta_{k_n}^2 \tag{2.18}$$

$$COP = \frac{Q_n}{W_n} \tag{2.19}$$

Therefore, as most of the parameters were already defined, the COP could be represented as a function of stack's length and position. Consequently, a MATLAB code (see Appendix A) based on the aforementioned equations was developed. By plotting them in a 3D manner, a set of length and position to achieve the peak COP was found (thus optimizing length and position to achieve the best performance).

Figure 12 displays COP against normalized stack's length and position, Figure 13 displays COP against non-normalized stack's length and position.

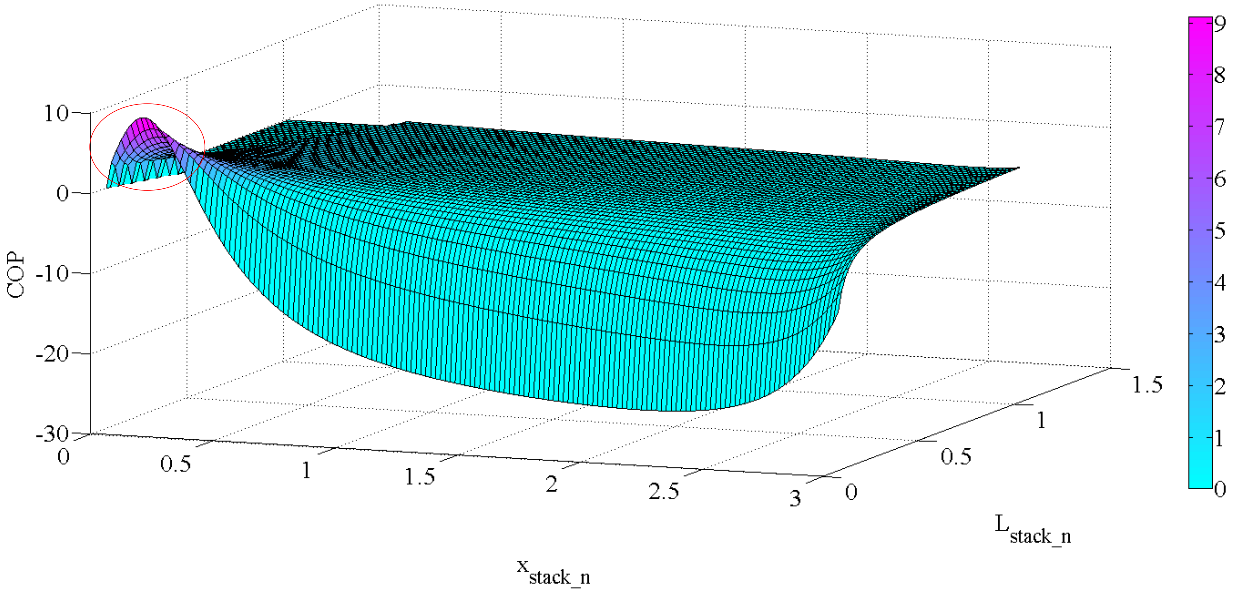

Figure 12: COP against normalized stack's length and position

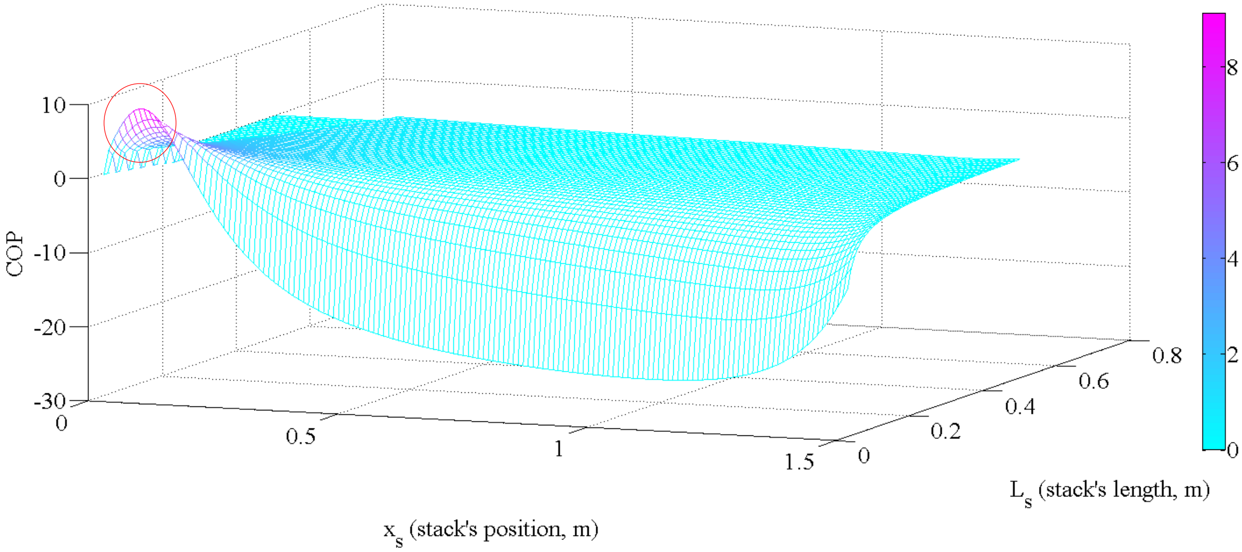

Figure 13: COP against stack's length and position

The red bump (marked with the red circle) on the surface of the COP plot in Figure 12 and Figure 13 represents the area where the COP above zero (also has violet coloring) and thus a stack with particular length at particular position the speaker that correspond to the marked area should experience TA phenomena and achieve heat pumping.

In more details, Figure 14 and Figure 15 represent COP against stack’s length and COP against stack’s position accordingly.

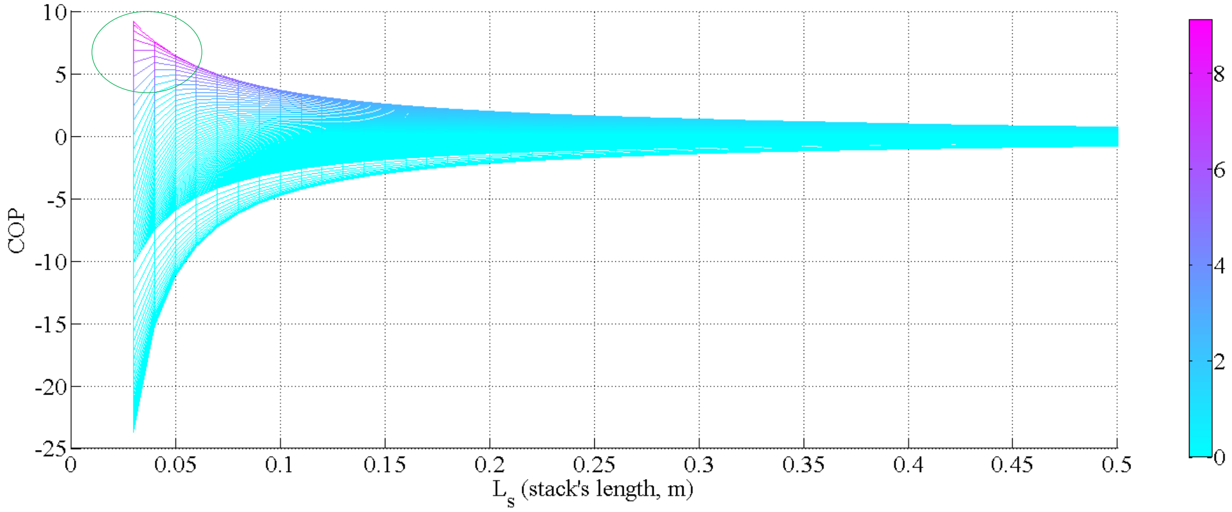

Figure 14: COP against stack’s length

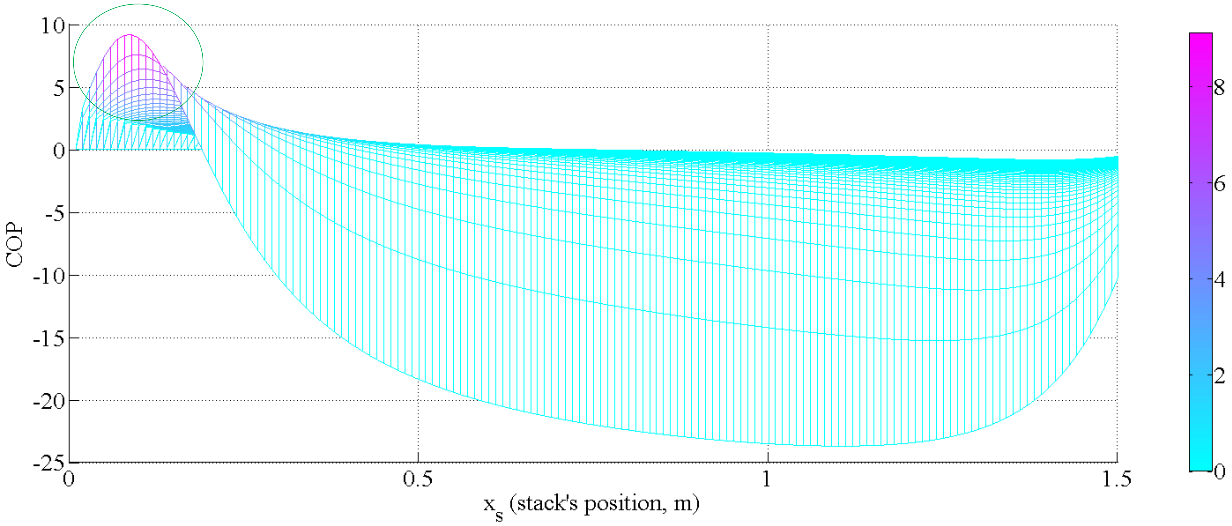

Figure 15: COP against stack’s position

Therefore, as it could be observed from Figure 14 and Figure 15, shorter length and smaller position give higher COP (areas marked with green circle). However, the stack should not be very short as it would destroy the temperature gradient between the hot and cold ends due to fast heat transfer via thermal conduction. For the stack’s design, 60 mm length was chosen with 75 mm position which resulted in a theoretical $\mathrm{COP} \approx 4.97$. Table 6 summarizes the stack's dimensions and performance parameters.

Table 6: Stack's geometry and performance.

Stack's length (L_{stack})	60 mm
Stack's position away from the speaker (x_{stack})	75 mm
Theoretical COP (COP)	4.97

CHAPTER III

EXPERIMENTAL SETUP AND PROTOCOL

3.1 General setup and protocol for two sets of experiments

The whole experimental setup was built according to the theoretical calculations. As shown in *Figure 16*, the original setup for the first set of experiments included:

- Vertically standing TAC (covered with one-layer mineral wool insulation).
- Vertically standing reference system (same design as TAC, but no sound input).
- Water tank with pump (connected to hot end heat exchanger in the TAC)
- Electronic hygrometer with a probe.
- Humidifier (connected to both TAC and reference system)

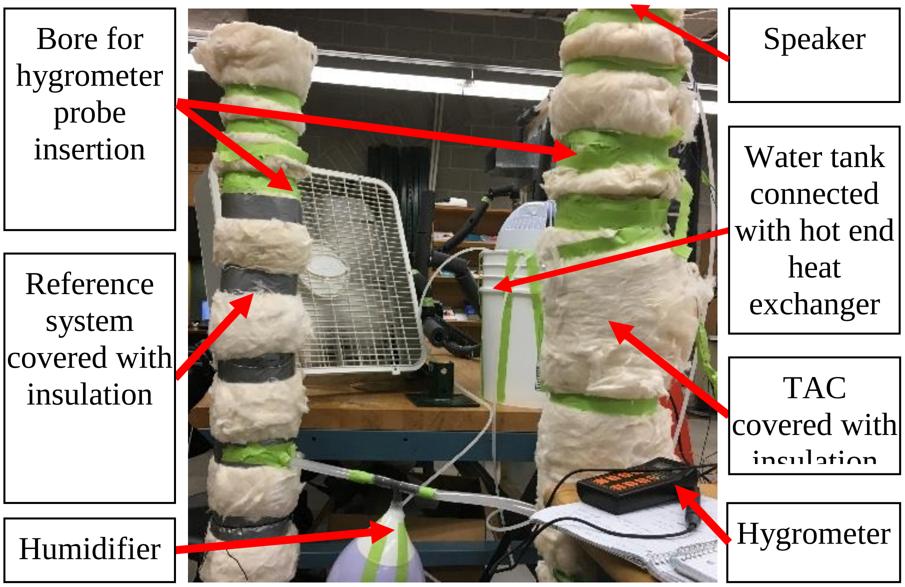

Figure 16: Experimental setup

The stack was 3D printed using PLA filament. The water operating copper heat exchanger was attached to the hot end of the stack and connected through plastic pipes with the water bucket (as a heat sink), as demonstrated in Figure 17. It was removing excessive heat from the hot end (especially as there were two heating sources, one of them is due to heat pumping from the cold end during the TA process and the second one is the Joule heating from the speaker).

Figure 17: Top view w/out speaker (copper heat exchanger attached to the stack's hot end)

To take temperature readings during the experiment, two exposed K-type thermocouples were attached correspondingly for the cold and hot ends of the stack, while one T-type thermocouple was submerged into a water bucket, as shown with details in Figure 18.

Figure 18: Three thermocouples (left: cold end; middle: hot end; right: water bucket)

Hygrometer in Figure 19 was used to measure the relative humidity and saturation temperature during the experiment by inserting the probe inside the TAC/Reference system through the bore near the cold end of stack. It allowed to record the Relative Humidity and air temperature in the vicinity of the cold end of the stack.

Figure 19: Hygrometer

The humidifier in Figure 20 was connected via transparent flexible plastic pipes of equal length to both TAC and reference system. Its aim was to provide humid air into both systems.

Figure 20: Humidifier with flexible pipes

Overall, there was two set of the experiments performed with some small changes in setup and experimental protocol made for the second set. For the second set of the experiments five major changes in setup were made:

- Thermocouples attached to the stack were changed from K-type to T-type as after the number of experiments in the first set they began to corrode.
- Flexible feeding pipe was replaced with the rigid pipe and was connected either to TAC or to reference system at the same time (in the original setup, it was connected simultaneously to both system making them be interconnected and therefore they had a mass flow between two systems during the experiment due to higher operating pressure in TAC).
- Hygrometer was not used anymore as vapor feeding from humidifier was changed from pre-feeding to continuous feeding during the experiment (see the flow chart later).
- Electronic scales were used to measure not only caps weight before and after the experiment (to measure amount of collected water) but also to measure humidifier weight before and after the experiment (to measure amount of water fed into a system).
- In the original experimental setup, only parallel plates stack was used, while in the setup for the second set of experiments, three different stacks (parallel plates, squared mesh and circular mesh) were used.

Figure 21 depicts the changes in the experimental setup for the second set of experiments.

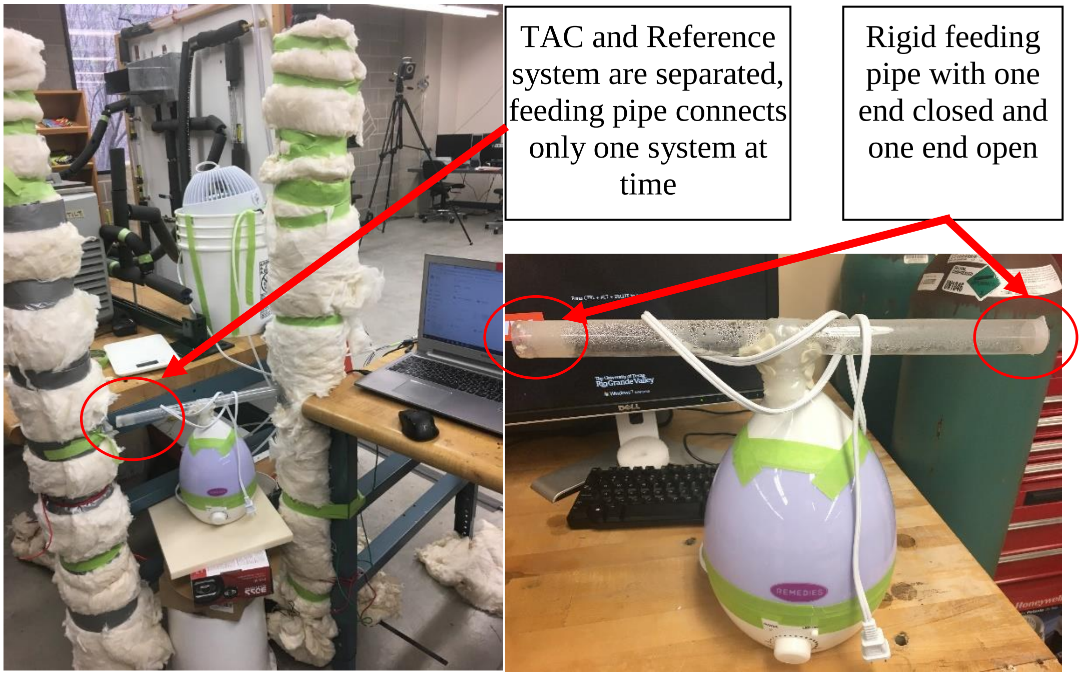

TAC and Reference system are separated, feeding pipe connects only one system at time

Rigid feeding pipe with one end closed and one end open

Figure 21: Experimental setup with changes for the second set

3.2 Experimental protocol for two sets of experiments

As mentioned before, there was two sets of experiments performed overall (flow chart for protocols shown in Figure 22). The first set of the experiments focused on dehumidification performance of the TAC as the humid air was fed into both systems before TA cooling started (pre-feeding both systems with humid air) and was not supplied during the experiment, thus allowing to analyze how strong was dehumidification in TAC (additionally using hygrometer). However, in the second set of the experiments, humid air was constantly fed into one system (because the feeding pipe was connected to only one system at the same time) during the whole experiment allowing to analyze water harvesting performance of the TAC through measuring how much water was fed into the system and how much was collected.

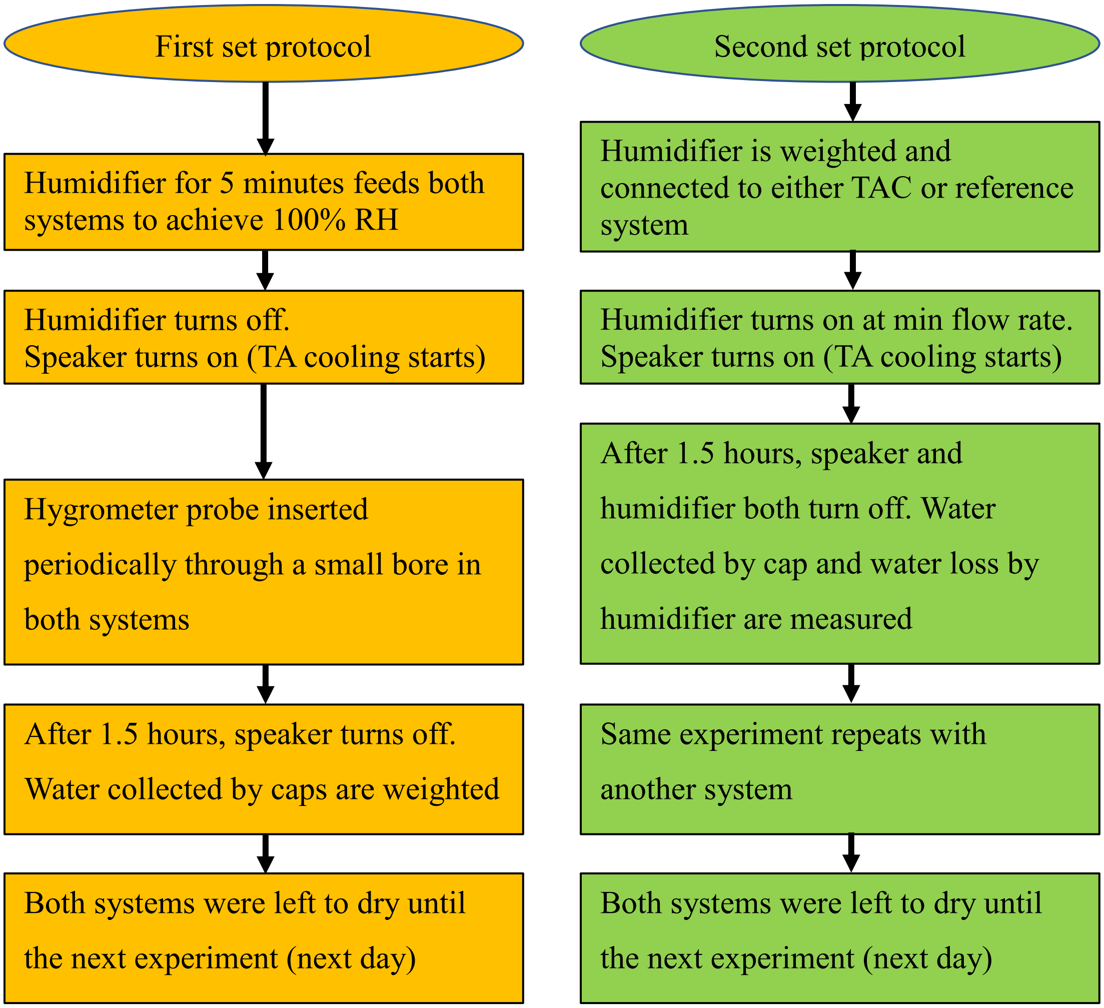

Figure 22: Two sets of experiments protocols

3.3 Thermocouples validation

In the first set of experiments, a set of three thermocouples connected to NI myDAQ module (Appendix B) were used to collect data. Two of them were exposed K-type thermocouples (connected to Hot End and Cold End of the stack correspondingly) and one was a T-type thermocouple (submerged into the water in the basket). A simple test was performed to ensure the accuracy of the readings from thermocouples – they were inserted into boiling water and the output was recorded.

In the second set of experiments, the two K-type thermocouples (that were connected to the stack’s hot and cold ends) were replaced with T-type thermocouples (Figure 24).

Figure 23: Three thermocouples for the second set (T1 cold end, T2 hot end, T3 water basket)

Both K-type and T-type thermocouples in both experimental setups showed a good agreement with the water boiling temperature (Table 7).

Table 7: Boiling water test validation for three thermocouples in both experimental setups

	T1 Hot End (°C)	T2 Cold End (°C)	T3 Water (°C)
Average (first set)	99.39	99.23	99.44
Average (second set)	100.65	100.33	100.54

3.4 Three different design stacks

In the first set of experiments only parallel plates stack was designed, 3D printed and used. However, for the second set of experiments, three different geometry stacks were used. In addition to the initial parallel stack plates, two new stacks were developed with the aim to compare their performance later via the experiments. Overall, three stacks with different geometries were:

1. Parallel plates stack (Figure 24, on the left)
2. Squared mesh plates stack (Figure 24, in the middle)
3. Circular plates stack (Figure 24, on the right)

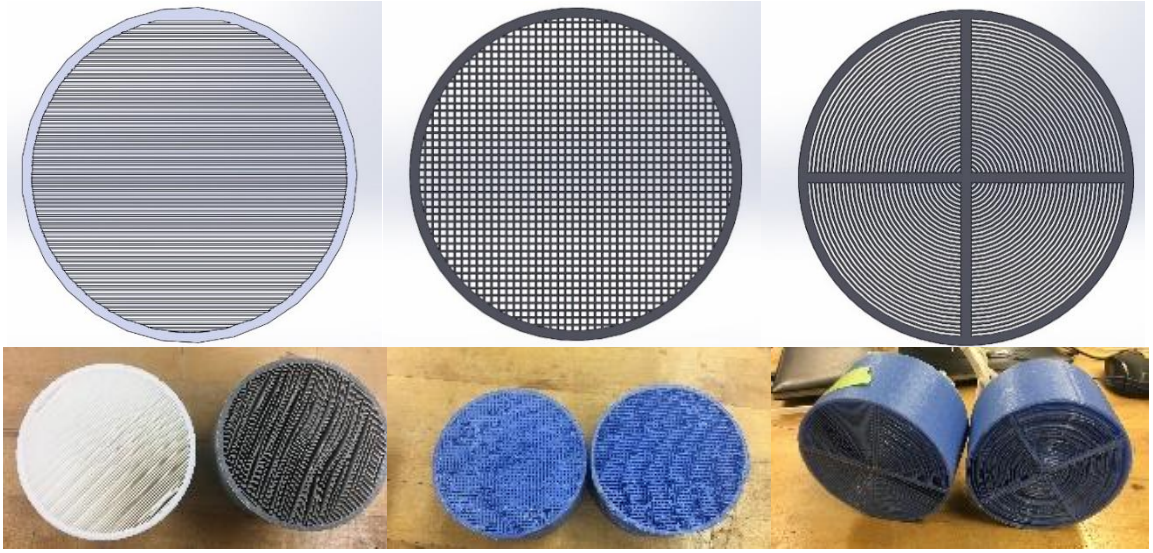

Figure 24: CAD design (on top) and 3D printed (on bottom) for different design stacks.

All three stacks had the same diameter to fit the resonator (100 mm), thickness of the plates due printing resolution (0.5 mm), length and were positioned at the same distance from the speaker in the experiment (see Table 6 for details). Consequently, they were designed to have the same theoretical blockage ratio as 0.6 (thus they had different spacing). Also, the CAD calculated blockage ratio was different from the theoretical value (Table 8).

Table 8: Three stacks - geometry

Shape	Spacing (mm)	Solid surface area (mm^2)	Theoretical blockage ratio	CAD blockage ratio
Parallel	0.75	3661.93	0.6	0.53
Square	1.72	3688.31	0.6	0.53
Circular	0.75	3937.84	0.6	0.5

CHAPTER IV

RESULTS AND DISCUSSION

4.1 First set of experiments

Temperature readings (via thermocouples), collected condensation measurements (measuring weight of the dry cap prior the experiment and wet cap after the experiment) and hygrometer measurements were obtained in the first set of the experiments. The protocol was:

1. Humidifier is turned on and set to run for 5 minutes feeding both systems (reference and TAC) with the humid air (to achieve 100% humidity inside).
2. Turning off the humidifier while turning on the speaker (110 Hz working frequency sin wave audio signal) to start TA effect in TAC.
3. Periodically during the experiment, the hygrometer probe was inserted to the reference system and TAC through a small bore to measure relative humidity and temperature inside (the zone slightly under the cold end of the stack).
4. After around 1.5 hours of TA cooling, the speaker is turned off and the closing bottom cap is being removed to weight it with the collected water inside (mass of the water is the mass of the wet cap minus the original mass of the dry cap).
5. After each experiment both systems were dried for at least one day (using large fan to create forced convection) to ensure that the water completely removed from them prior to the new experiment.

It was assumed that if the working fluid was humid air and the cold end temperature would reach the dew point, condensation should occur on the surface of the stack in the TAC. Therefore, a dehumidification process may occur, and the condensed water would fall from the stack plates due to gravity. Thus, flowing air stream exits the stack with a dew point equal to the temperature of the cold end of the stack (Zimmerman and Lavine 1964). In the similar work (Hiller and Swift 2000), to explore the effects of condensation to thermoacoustic phenomenon, Hiller and Swift developed two simple models, wet-wall model and fog model, to verify with an experiment of an open-flow thermoacoustic cooler with stack temperatures below the saturation temperature of the flowing air, and their results suggested that the thermoacoustic effect of droplets inside the stack is small. However, it was still believed that if the incoming air has a large relative humidity or in the form of mist, there is a high chance that the condensate (water droplets) may block the air pathway and negatively affect TA phenomenon. Consequently, to address such questions, two measurements instruments were available:

1. Thermocouples readings as a way to analyze thermoacoustic performance of the system.
2. Relative Humidity readings from hygrometer and collected condensed water in the cap data to measure condensation and dehumidification performance.

4.1.1 Thermoacoustic performance results for the first set

Thermoacoustic performance of the TAC was analyzed by acquiring data from the thermocouples via NI myDAQ during five experimental trials (Trial 0 to Trial 4) conducted by the same protocol. The Trial 0 (Figure 25) was performed without pre-feeding humid air into the systems and without using hygrometer (but with overall time of the experiment as 1.5 hours). Basically, in Trial 0 the TAC was separated from the humidifier and reference system, sealed and

TA cooling was performed for 1.5 hours with collecting data from thermocouples to analyze maximum TA cooling performance in dry air (and without any collected water as the temperature did not reach low enough to start condensing water from lab dry air). TA cooling performance in Trial 0 in the form temperature drop due to cooling on the cold end from the initial temperature provided below (Table 9).

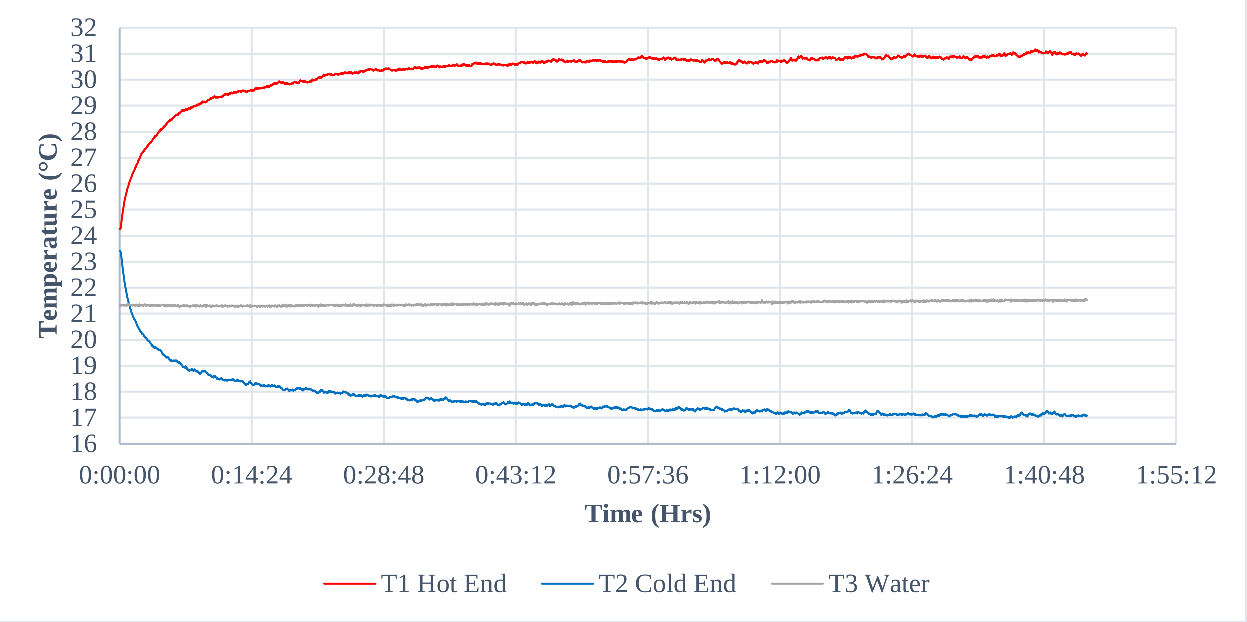

Figure 25: TAC results (Trial 0)

Table 9: TAC results (Trial 0)

Initial temperature at Cold End (°C)	23.42
Lowest temperature at Cold End (°C)	16.99
Maximum temperature drop at Cold End (°C)	6.43

Furthermore, Trials 1-4 (Figure 26 - Figure 29) were conducted using pre-feeding humid air for 5 mins and a standard protocol for the first set.

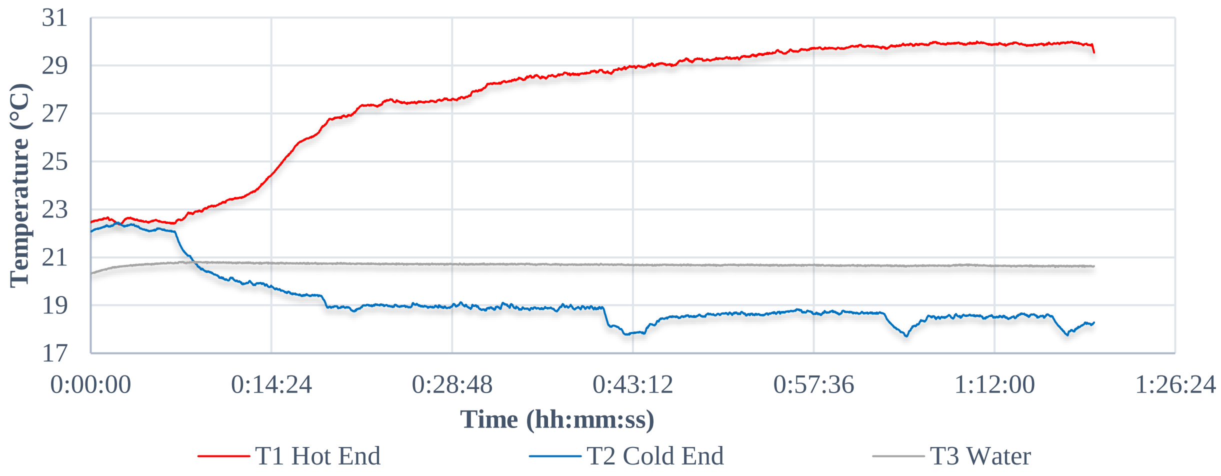

Figure 26: TAC results (Trial 1)

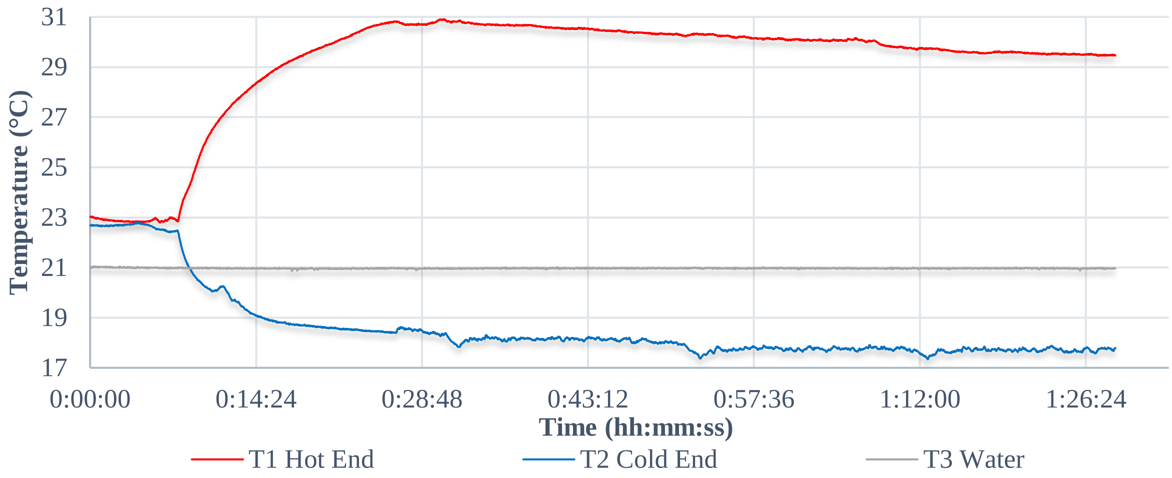

Figure 27: TAC results (Trial 2).

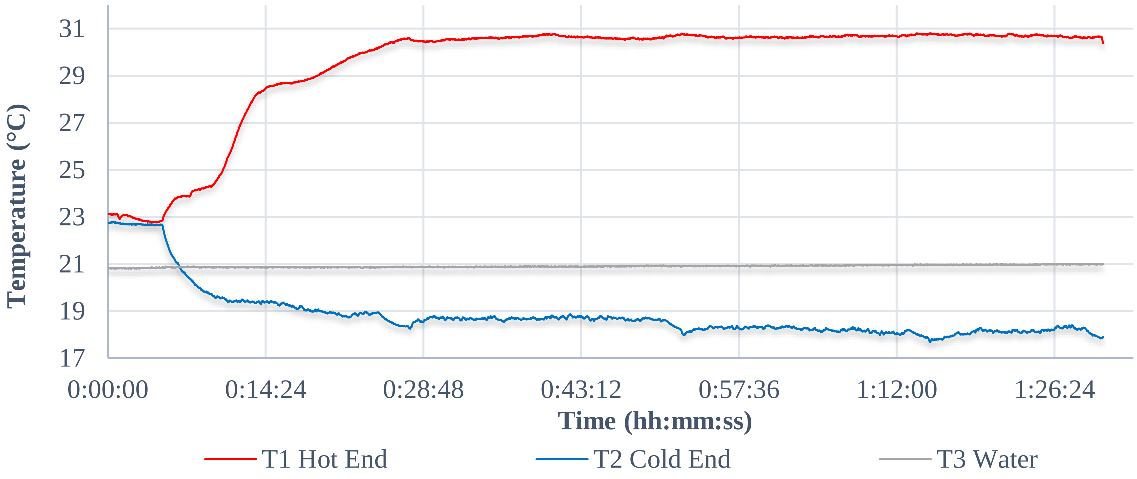

Figure 28: TAC results (Trial 3).

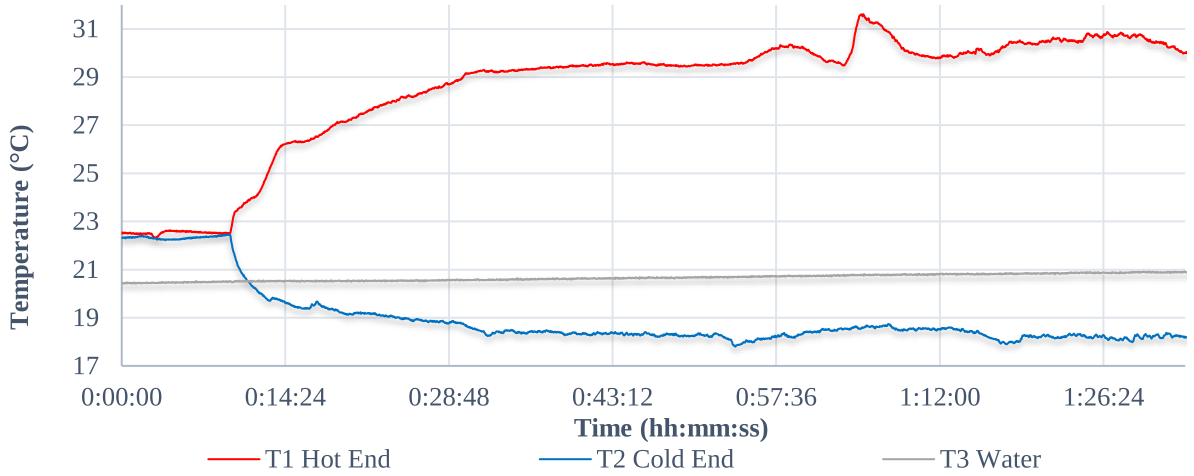

Figure 29: TAC results (Trial 4).

Figure 25 - Figure 29 provide the temperature variation readings from the thermocouples inside the TAC and water basket. The red line indicates the thermocouple readings from the hot end of the stack. The temperature initially was approximately equal to the temperature on the cold end (blue line) but after the speaker was turned on, the hot end temperature started to rise, while the reduction of cold end temperature took place. The kinks in the plots (except for Trial 0) indicate the moments when the hygrometer bore was inserted into a system thus causing some disturbances. The green line indicates temperature of the water in the bucket and as it served as a heat sink for the hot end heat exchanger, it is reasonable that the temperature was rising correspondingly with the hot end temperature rising. At some point, the cold end temperature did not change a lot and the system achieved a rough thermo-equilibrium (Joule heating of the speaker was a significant part of the hot end temperature fluctuations in most of the trials).

4.1.2 Air temperature and humidity results for the first set

During the first set, the relative humidity and temperature of air in the vicinity of the cold end of the stack in both TAC and the reference systems (cold end of the stack in the reference system is not actually a cold end as in TAC, but rather a geometrical counterpart, a bottom side of the stack named also cold end for simplicity) were measured by periodically inserting hygrometer probe into the bore (except in Trial 0 as the hygrometer was not used there). Also, a dew point value for such temperature and relative humidity was automatically calculated by hygrometer, but in general it also can be manually estimated by using psychometric chart (Appendix C).

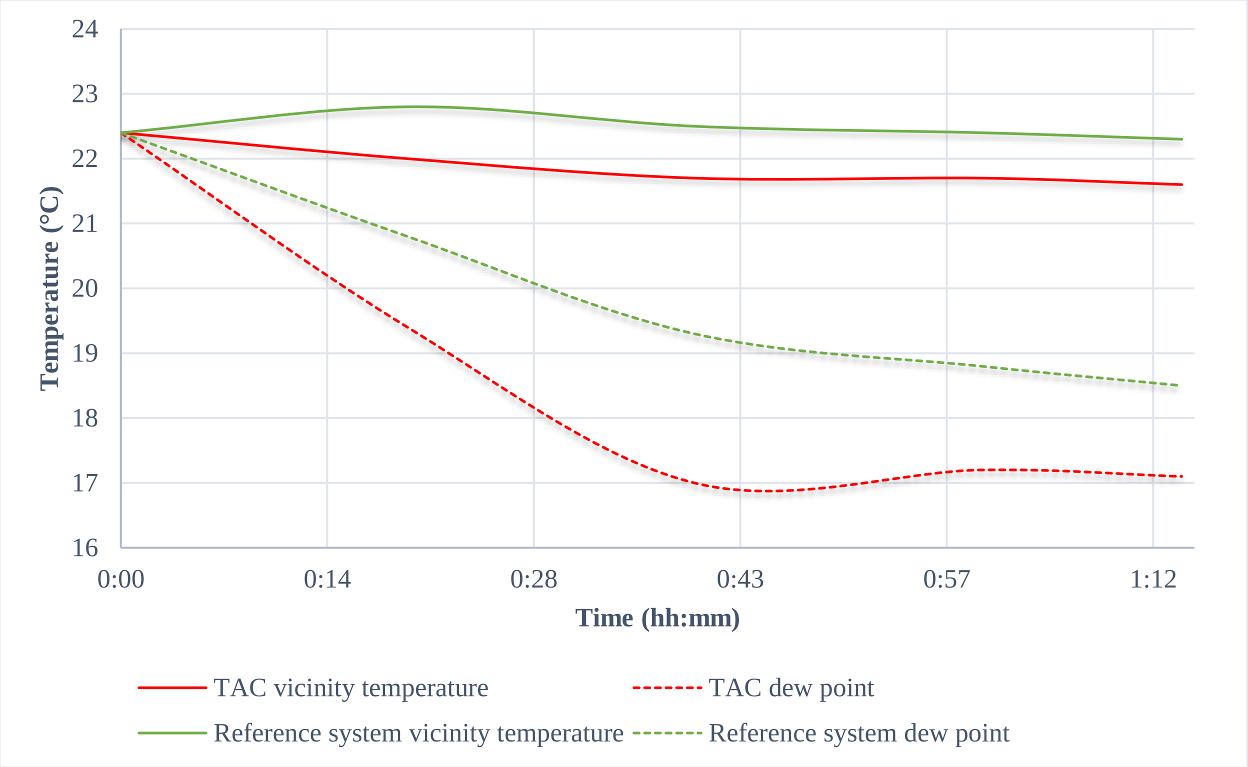

Figure 30: Hygrometer temperature readings (Trial 1)

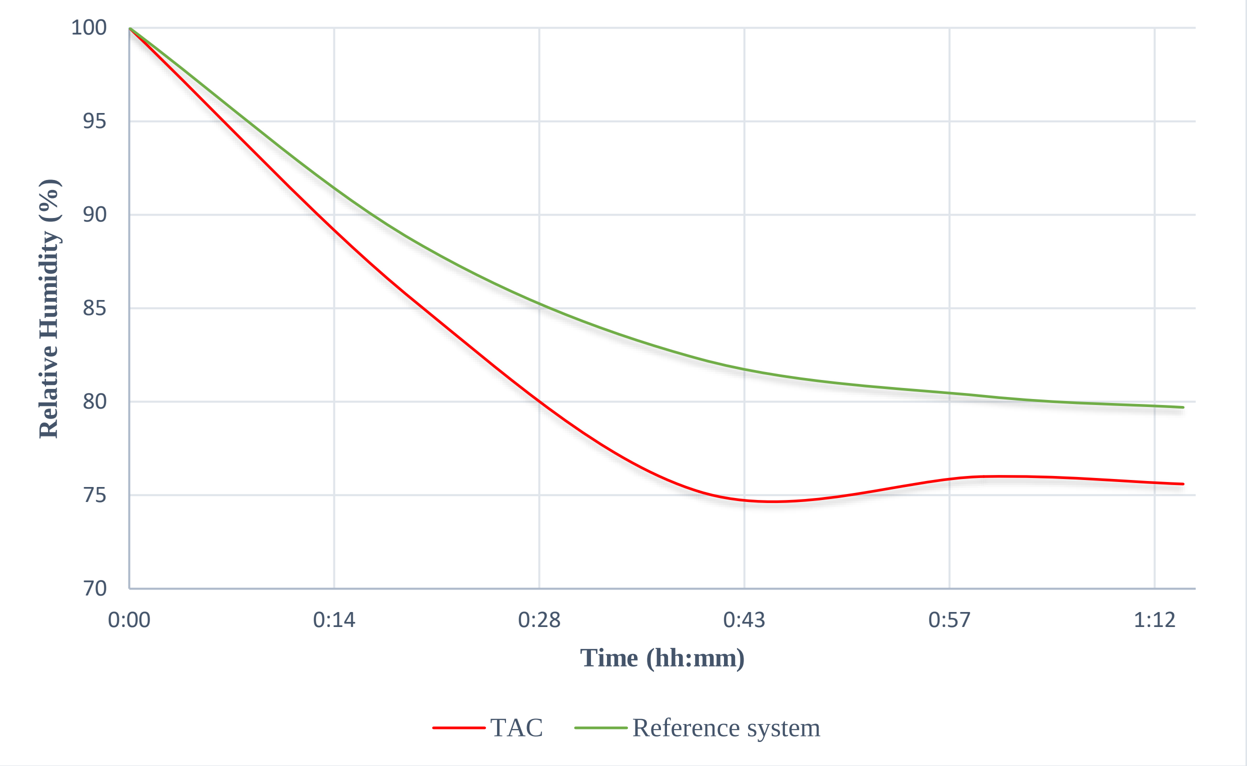

Figure 31: Hygrometer relative humidity readings (Trial 1)

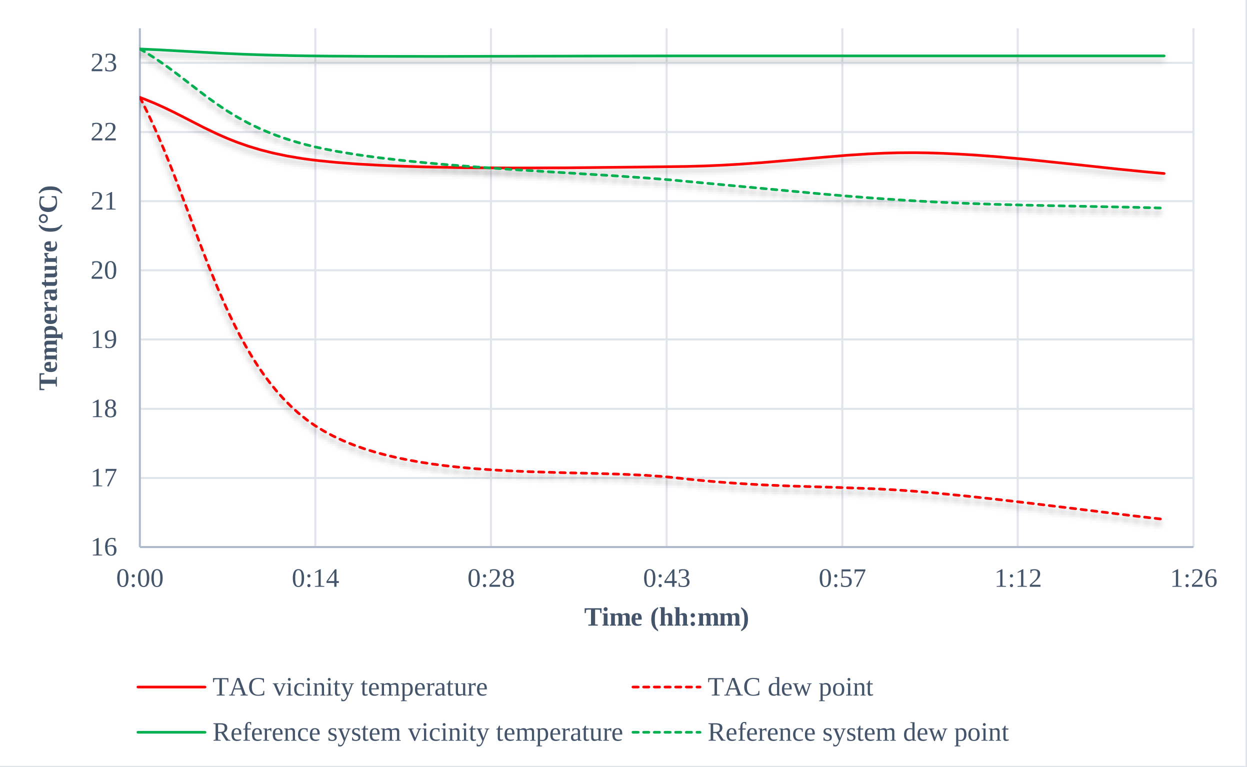

Figure 32: Hygrometer temperature readings (Trial 2)

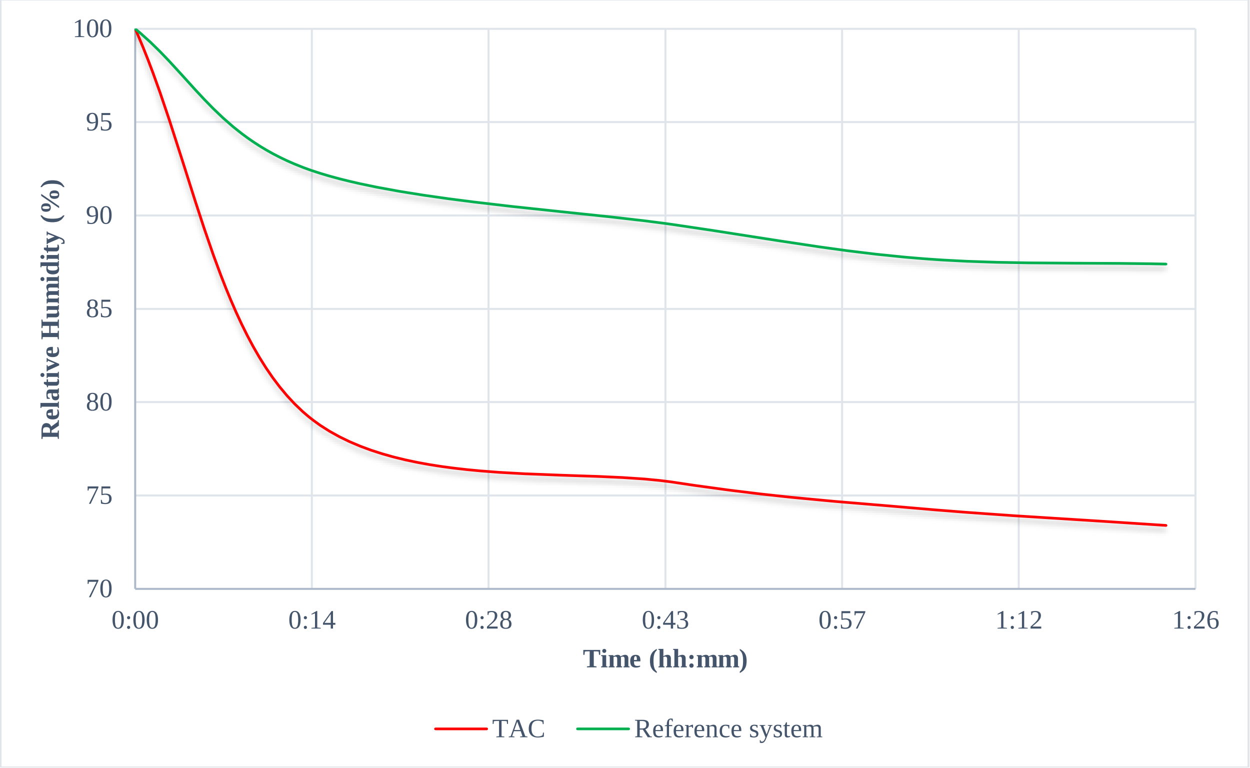

Figure 33: Hygrometer relative humidity readings (Trial 2)

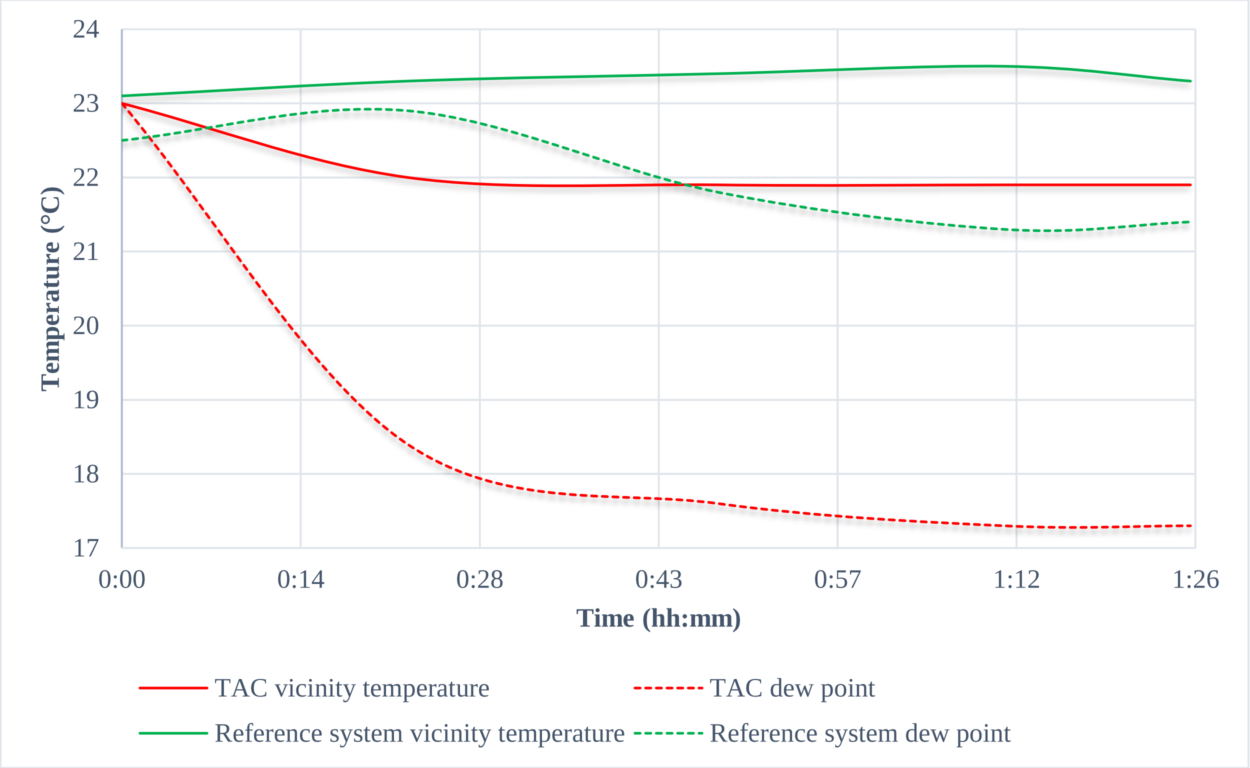

Figure 34: Hygrometer temperature readings (Trial 3)

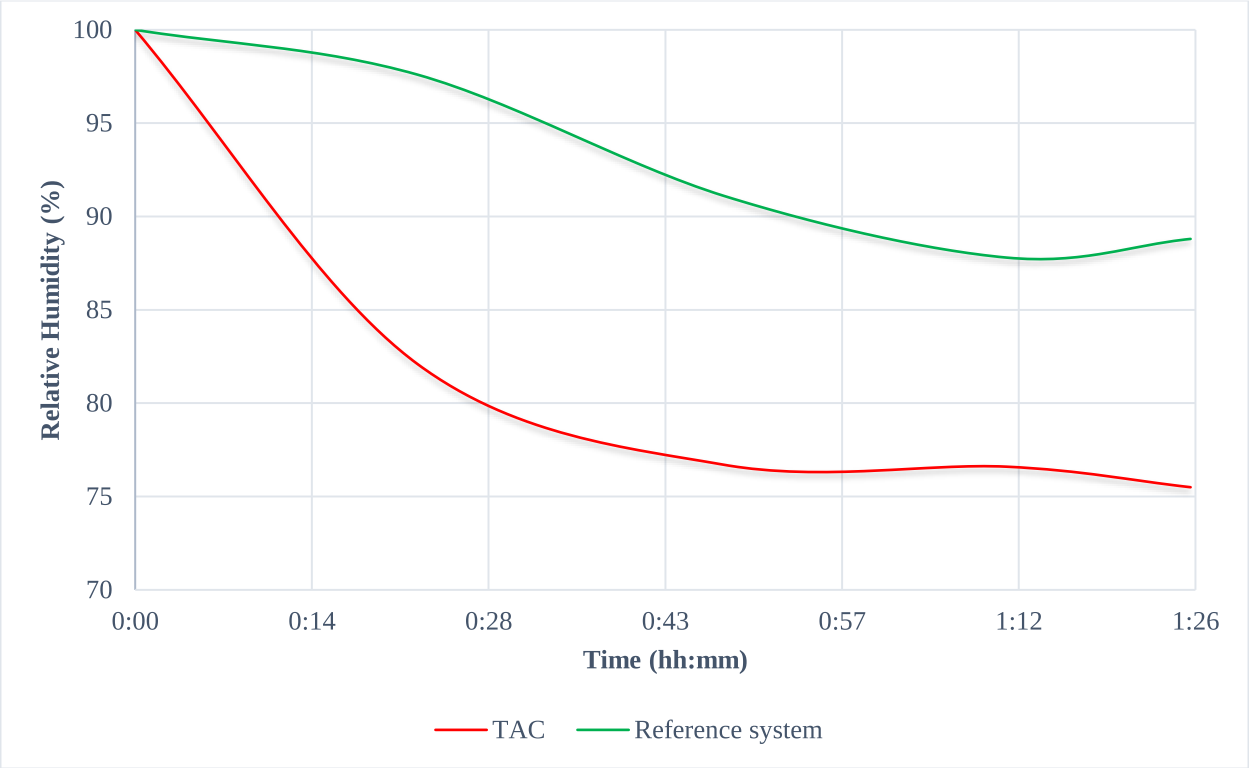

Figure 35: Hygrometer relative humidity readings (Trial 3)

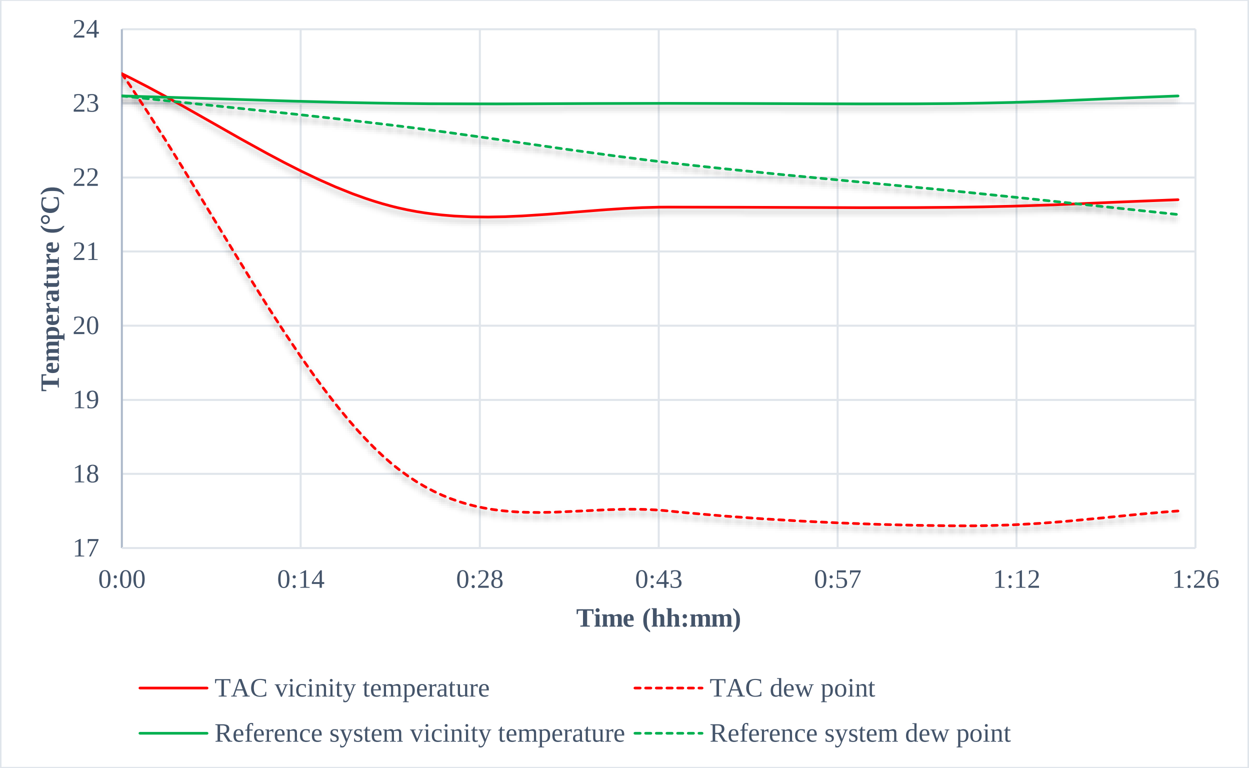

Figure 36: Hygrometer temperature readings (Trial 4)

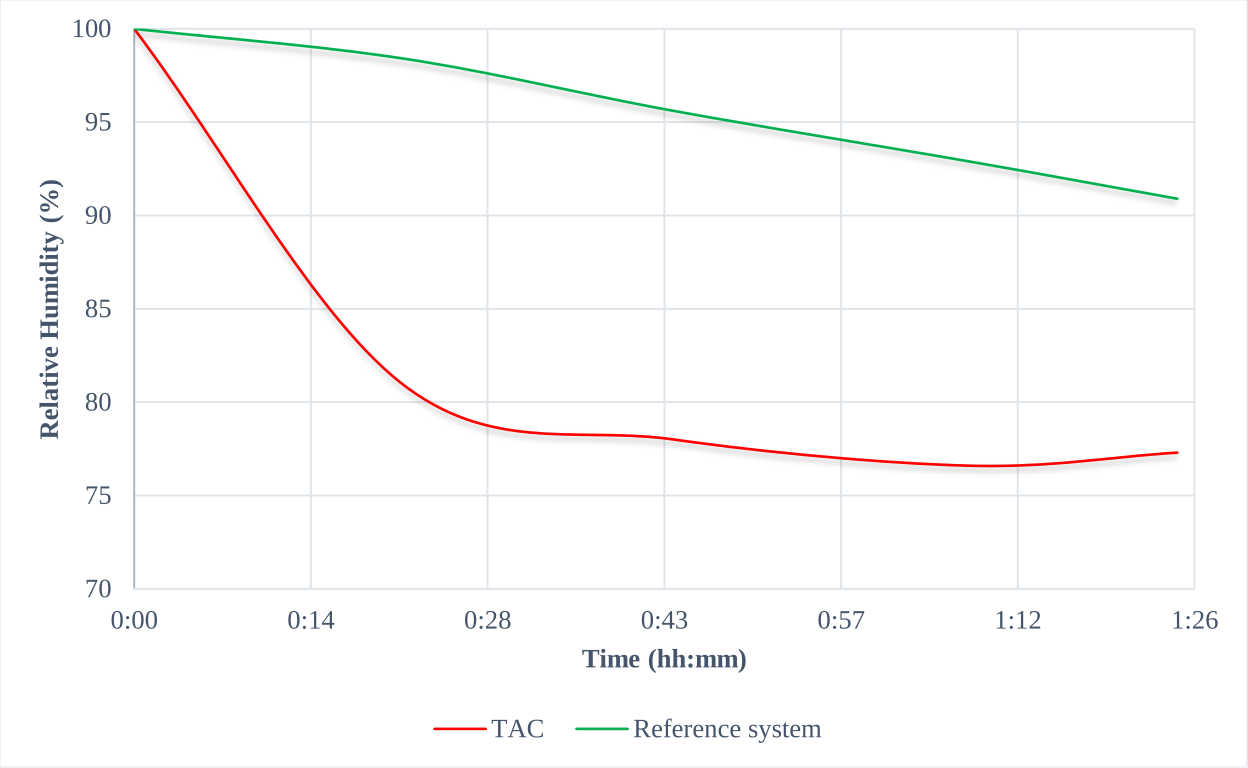

Figure 37: Hygrometer relative humidity readings (Trial 4)

Figure 30 - Figure 37 represent the hygrometer readings for temperature and relative humidity for Trial 1 - 4. It is important to notice that these readings were taken in the vicinity of the cold end in the TAC and reference system during the experiment and thus should not be mistaken with the data from thermocouples. Basically, after obtaining the results they could be interpreted. The temperature of the air in the vicinity of the cold end in the TAC (solid red line in the hygrometer temperature readings plots) was decreasing during the experiment. It correlates with the general cooling of the stack's cold end during TAC operation. The temperature of the air near the lower end of the stack in the reference system (solid green line in the hygrometer temperature readings plots) remained constant as no cooling was provided in the reference system. The relative humidity in both systems were dropping from 100% to around 75% in the TAC (solid red line in the hygrometer relative humidity readings plots) and to around 85-90% in average in the reference system (solid green line in the hygrometer relative humidity readings plots). Ideally,

there should not be any relative humidity drops in the reference system as the system assumed to be closed and insulated from the environment. However, due to insertion of the hygrometer probe, both systems were exposed to the surroundings for the time of insertion and thus mixing of the humid and dry air from the lab (normally around 60% RH) happened. Nonetheless, in all trials RH drop in TAC was larger than the RH drop in reference system, leading to conclusion that at some degree TAC had a dehumidification effect. The dew point was also decreasing for TAC (dashed red line in the hygrometer temperature readings plots) and for reference system (dashed green line in the hygrometer temperature readings plots). However, there was also a noticeable difference between two systems. The dew point in the TAC was dropping down by 5-6 degrees in comparison to the reference system where it was dropping by only 1-2 degree. It correlated with the dehumidification effect in TAC as longer the operation was run consequently it was harder to harvest additional water from the air. Also, dehumidification/water harvesting process in TAC was even stronger than it seems from the graphs, as according to the psychometric chart (Appendix C), lower dry bulb temperature at the same relative humidity leads to lower dew point and as well, lower dry bulb temperature at the same dew point leads to lower relative humidity. Hence, when all three parameters are decreasing, it means that the water content in the air decreasing (i.e. dehumidification/water harvesting).

4.1.3 Water harvesting/condensation performance for the first set

The water harvesting performance was analyzed in the first set for Trial 1-4 by collected water data with comparison between actual TAC and a reference system. The amount of collected water due to condensation was measured by comparing initial weight of the dry closing cap (attached to the bottom of the both systems) and the weight of the wet cap after the end of the experiment. The caps that were measured are shown in Figure 38.

Figure 38: Post-experiment photo of the caps (left: from TAC; right: from reference system)

Table 10: Water harvesting results.

Trial	Temperature drop on cold end (°C)	Water collected in reference system (g)	Water collected in TAC (g)	Condensation enhancement $\left(\frac{W_{H_2O_{TAC}}}{W_{H_2O_{Ref}}}-1\right)x100\%$ (%)
#1	4.75	1.4	2.4	71
#2	5.56	1.7	2	18
#3	5.06	2.1	3	43
#4	4.51	3.1	3.5	13
Ave	4.97	2.08	2.73	36

As it is seen from the results (Table 10):

- In average, temperature drop (from the initial room temperature) that was achieved on the cold end of the stack was close to 5K decrease. It was considered as a good result for the TA system operating on unpressurized air.

- TA gave in average 36% enhancement for the condensation. Even with such small number of trials, the pattern is clean, the TAC showed condensation enhancement in all trials over a reference system.

4.1.4 Intermediate conclusion from the first set

So far, the first set of experiments confirmed that the design calculations were correct and TAC operating on the unpressurized air is feasible and can achieve a moderately good temperature drop. Also, it was experimentally proven that the TAC designed by dry air properties can be started in the ultimately humid air conditions. The most signification observation was that the TA phenomena may indeed enhance the condensation rate (water harvesting) and dehumidification process.

Although the first set of experiments provided relatively good source of data for thermoacoustic performance, dehumidification and water harvesting analysis, the design of the experiment itself contained several important defects that was one of the reasons for the need in the second set of experiments. One of such defects was the fact that both TAC and reference system were interconnected though the flexible pipe. Therefore, humid/dry air from the TAC could easily flow into reference system but the pressure fluctuations in the TAC system thus were affecting the accuracy of the comparison.

4.2 Second set of experiments

For the second set of experiments, the setup was revised, and the experimental protocol was changed. Basically, the protocol for the experiment was changed from feeding two interconnected systems with humid air for 5 minutes to conduction the experiment with only one system at the time and continuously feeding it with humid air as it was believed could give sensible results. Consequently, in the second set of the experiments, neither TAC nor reference system experiment had any effect on each other due to physical separation of the systems from each other (Figure 39). Also, this time, the amount of water fed into a system was carefully measured as well as the water collected in the cap after the experiment. Thus, it allowed to calculate percentage of water collected in the experiment rather than just absolute value of water collected. Hygrometer was not in use anymore as it was concluded that constant insertion of the probe could negatively affect the flow of the experiment. However, hygrometer was substituted with obtaining visual images of the stack's lower end (cold end) before and after the experiment that could give a better understanding of the condensation performance.

Figure 39: Humidifier attached alternately to reference system (left) and to TAC (right)

4.2.1 Thermoacoustic performance results for the second set

Three new stack designs were tested to obtain the temperature variations. The relative percentage of collected condensed water was also measured by measuring the weight of the humidifier before and after the experiment to estimate how much water-vapor was fed, the weight of the dry cap and wet cap before and after was also measured to estimate how much water was collected in the cap as in the first set of experiments.

Each new set had one preliminary experiment (Case 0) where TAC was running without connected humidifier to measure the maximum cooling performance in the atmospheric air. Then, each case set (Case 1-4) was tested with humidifier connected for both TAC and the reference system. The experimental cases with brief description can be found in Table 11, and the new testing protocol was as follows:

1. Humidifier and the dry cap were separately put on the scales and their weights were measured, and then they were attached to the TAC.
2. LabVIEW code was run to record thermocouples output.
3. Humidifier was turned on the min flow.
4. The speaker was turned on (110 Hz working frequency sin wave audio signal) to start TA effect and heat pumping in TAC.
5. After 1.5 hours, the humidifier and the speaker were turned off, the LabVIEW program was stopped, and thermocouples readings were saved. The closing bottom cap was then removed and the weight of the wet cap with water was measured on the scales (so the weight of the collected water can be calculated). The humidifier was disconnected, and the weighted on the scales to calculate water that was fed into the system
6. Humidifier and the cap from the reference system were weighted, and then connected to the reference system.

7. Humidifier was set to min flow again and another 1.5 hours long experiment was started but now with the reference system (without thermocouples and without working speaker, thus with no TA phenomena).
8. After 1.5 hours, the humidifier was stopped and was removed with the cap and they both were weighted again to measure humidifier loss of water, and the weight of collected water in the wet cap.
9. After each experiment both systems were dried for at least one day to ensure that the water completely removed from the resonance tube prior to the next experiment.

Table 11: Experiment cases

Case	Stack	Description
P0	Parallel plates	No humidifier
P1-4	Parallel plates	Connected humidifier
S0	Squared mesh	No humidifier
S1-4	Squared mesh	Connected humidifier
C0	Circular plates	No humidifier
C1-4	Circular plates	Connected humidifier

The temperature variation versus time in the TAC for new cases are shown in Figure 40, Figure 41, Figure 42 (also in more details in Appendix D) and Table 12. T1 indicates a thermocouple attached to the hot end of the stack (top side of the stack), T2 indicates a thermocouple attached to the cold end of the stack (bottom side) and T3 are the thermocouples readings from the water bucket. Also, preliminary experiment data (P0, S0, C0 cases) are marked with solid dark red (for T1), solid dark blue (for T2) and solid dark grey (for T3) lines to make it visually be different from the experimental data when the humidifier was connected and fed TAC with vapor (P1-4, S1-4, C1-4 cases). In Table 12, there are four columns for initial and final temperatures at the hot end (T1) and cold end (T2), respectively. “Max T2 drop” column is for maximum temperature drop from the initial temperature at the cold end of the stack (ever detected during the experiment) and “Final T2 drop” column is for the difference between final and initial temperatures at the cold end. “Reduction in final T2 drop (by %)” column represents how much was percentage decrease in comparison to the reference value.

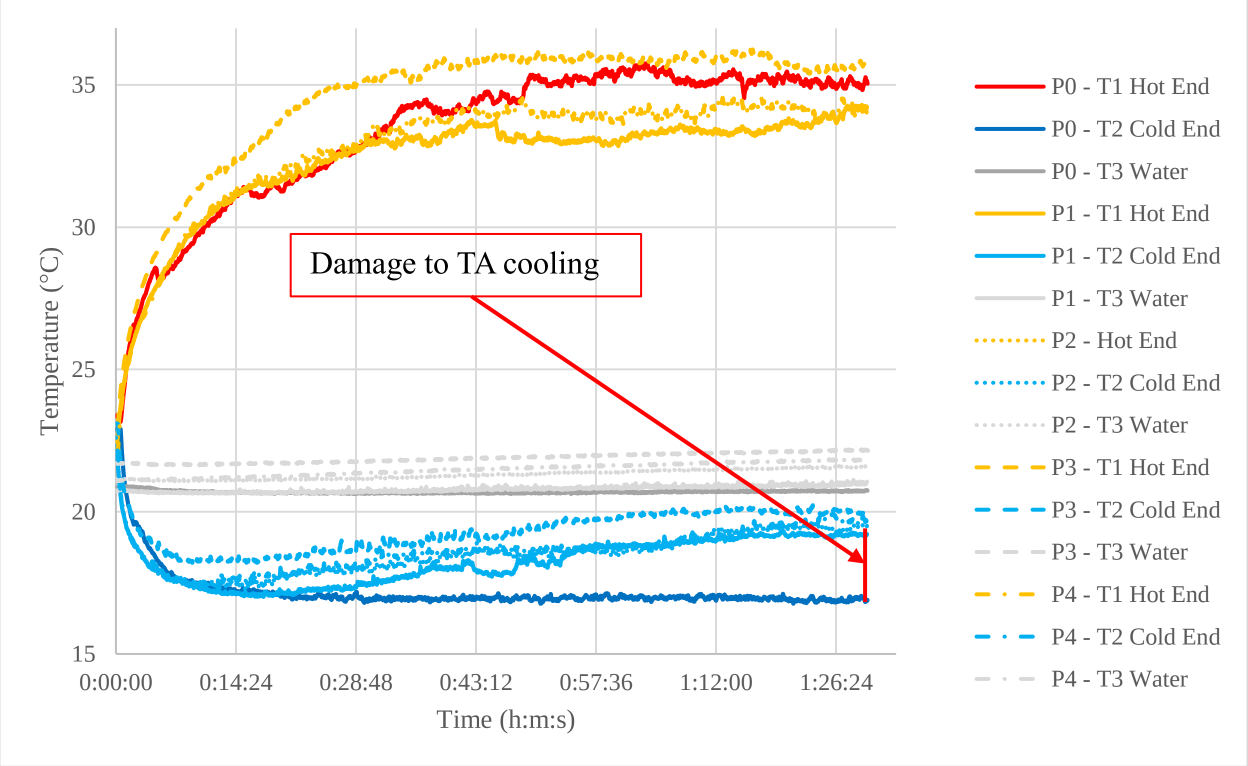

Figure 40: Parallel plates stack cases

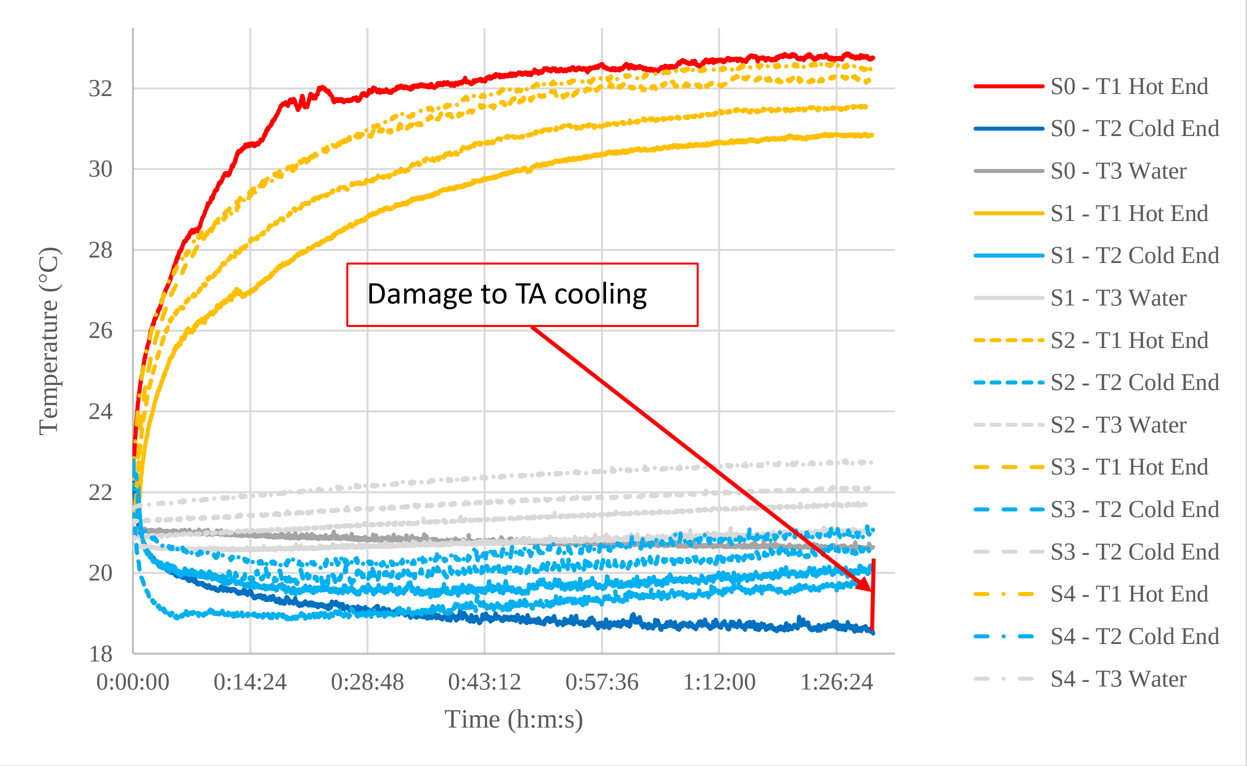

Figure 41: Squared mesh stack cases

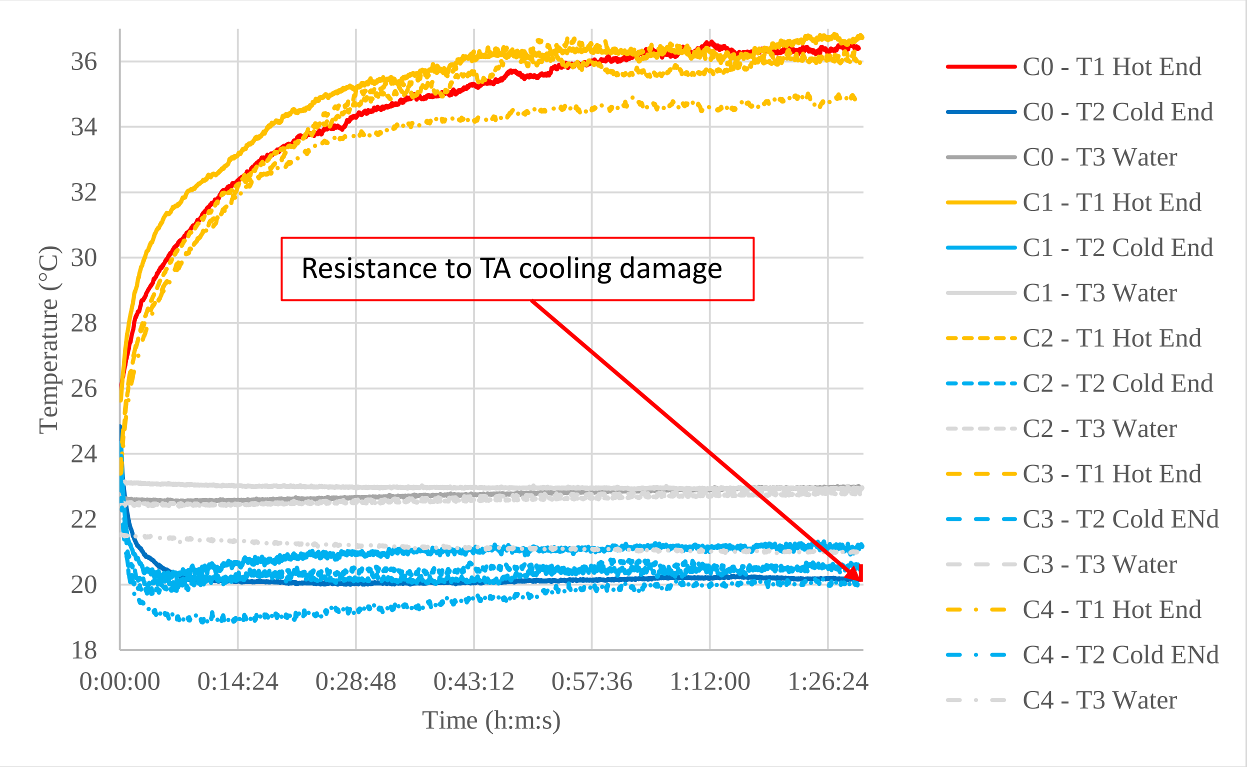

Figure 42: Circular plates stack cases.

Table 12: Thermocouples readings.

#	Initial T1(C)	Final T1 (C)	Initial T2 (C)	Final T2 (C)	Max T2 drop (C)	Final T2 drop (C)	Reduction in final T2 drop, $\left(\frac{Final\ T2\ drop_{Case\ 1-4}}{Final\ T2\ drop_{Case\ 0}} - 1\right) x100\%$ (%)
P0	23.4	35.0	22.9	16.9	6.1	6.0	Reference value
P1	22.3	34.2	22.3	19.2	5.3	3.1	48.7
P2	22.5	35.6	22.6	19.5	5.4	3.1	48.2
P3	23.1	35.8	23.1	20.0	4.9	3.1	49.1
P4	22.1	34.1	22.1	19.7	4.7	2.5	59.0
S0	22.5	32.8	22.8	18.5	4.3	4.3	Reference value
S1	21.6	30.8	22.2	20.1	2.8	2.1	51.5
S2	21.4	31.5	21.4	19.7	2.6	1.7	59.0
S3	22.4	32.2	22.4	20.5	2.7	1.9	55.6
S4	22.6	32.5	22.8	21.0	2.7	1.8	57.8
C0	25.9	36.4	24.8	20.2	4.8	4.7	Reference value
C1	25.6	36.5	24.3	21.1	4.2	3.3	30.1
C2	23.9	36.0	23.9	20.5	4.0	3.4	26.3
C3	23.5	36.2	23.5	20.6	3.8	3.0	36.9
C4	23.4	34.9	23.2	20.0	4.4	3.2	31.3

Table 12 could be used to evaluate the TAC thermal performance. There were some important observations made from it. First of all, TAC with parallel plates stack had the best cooling performance compared to other two designs. Secondly, it is obvious that the preliminary experiment with no connection to humidifier showed better TA performance in terms of maximum temperature drop on the cold end and larger sustained final temperature gradient between hot and cold ends. Thirdly, it is clearly noticed that without constant vapor input, TAC achieved the maximum temperature drop at the cold end and tended to sustain it (solid dark blue lines in the figures), so there is negligible difference between “max T2 drop” and final T2 drop. Whereas, when there was a constant vapor flow coming into TAC, the temperature on the cold end tended to significantly rise after max T2 drop point (light blue lines in the figures). Moreover, if final T2 drop for the zeroth case was taken as the reference value with the assumption that the zeroth case had the best thermoacoustic performance compared to others, percentage reduction could be calculated for the cases and an average could be found. Such average was important due to the following two factors:

- It showed that the continuous feeding with vapor damaged thermoacoustic performance (either due to realizing energy on the stack because of the condensation or because such condensation blocked the pores and simply decreased blockage ratio).
- The different stack geometry could be quantitatively evaluated on the ability to resist to such damage to the thermoacoustic phenomena from enhanced condensation (Table 13).
- Circular plates design for the stack is less affected by the damage to thermoacoustic cooling from the enhanced condensation.

Table 13: Average percentage decrease in T2 drop.

Stack Design	Average reduction in final T2 drop (by %)
Parallel plates	51.2
Squared mesh	56.0
Circular plates	31.2

4.2.2 Water harvesting/condensation performance for the second set

The next step was to measure the relation between water fed into a system by the humidifier and water condensed/harvested by the closing cap in the system. Therefore, aside from temperature readings, weightings to determine the effect from TA to the condensation enhancement were performed.

Table 14: Water fed/collected data

#	Water fed into TAC (g)	Water fed into REF (g)	TAC cap collected water (g)	REF cap collected water (g)	Water collected in TAC, $\left(\frac{w_{H_2O_{collected}}}{w_{H_2O_{fec}}}\right)x100\%$ (%)	Water collected in REF, $\left(\frac{w_{H_2O_{collected}}}{w_{H_2O_{fec}}}\right)x100\%$ (%)
P1	12.2	12.6	6.8	6.3	55.7	50.0
P2	18.2	17.8	10.4	6.2	57.1	34.8
P3	11.0	18.0	4.3	6.3	39.1	35.0
P4	18.1	26.4	6.7	6.5	37.0	24.6
S1	36.4	37.1	18.4	16.0	50.5	43.1
S2	28.2	29.8	13.1	13.3	46.5	44.6
S3	35.3	29.7	21.6	9.3	61.2	31.3
S4	41.8	22.8	22.1	6.8	52.9	29.8
C1	28.1	24.4	19.2	8.6	68.3	35.2
C2	21.1	20.5	10.0	8.6	47.4	42.0
C3	12.5	20.1	6.2	7.4	49.6	36.8
C4	35.5	18.1	19.8	5.8	55.8	32.0

Table 14 represents the data of weight measurement. “Water fed” was calculated as the weight difference of the humidifier before and after the experiment (because 100% of water went into TAC or Reference system depending which was connected at the time of the experiment). “Cap collected water” was measured by the weight difference between dry and wet cap, before and after the experiment accordingly. “Water collected” was calculated as the percentage of collected water at the cap and the water that was fed in by the humidifier. Furthermore, the average percentage of the collected water could be estimated for each stack design (*Table 15*).

Table 15: Average water collected percentage

Stack	Average water collected in TAC (%)	Average Water collected in REF (%)
Parallel plates	47.2	36.1
Squared mesh	52.8	37.2
Circular plates	55.3	36.5

Two significant outputs were made on the average water collected percentage calculations:

- In general, TAC enhanced the condensation rate and dehumidification as it was predicted. The reference system had relatively high percentage of collected water, which can be explained because of the continuous feeding and saturating closed system with vapor process. However, the TAC due to TA cooling had reached even higher percentage.
- There is almost negligible difference in average water collected percentage in reference system, while in TAC it varies with the geometry of the stack. It can be stated that based on the experimental results, circular plates stack had the best water harvesting performance while parallel plates and squared mesh stacks had nearly equal percentage.

Furthermore, another important observation was made by visually inspecting stack before and after the experiment with the camera. The condensation on the stack in the reference system was equally dispersed inside the stack on the plates and in the form of thin layer of tiny droplets. However, in the TAC, the condensation was vastly concentrated on the bottom surface of the cold end of the stack in the form of large water droplets.

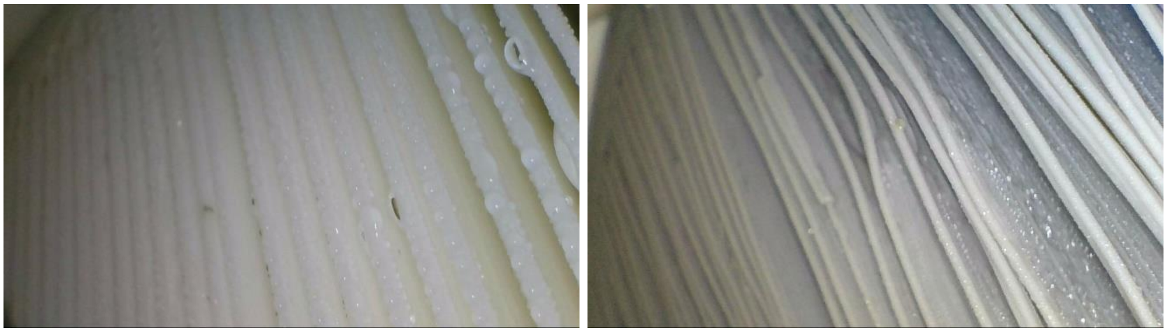

Figure 43: Post-experiment photo of the cold end of the parallel plates stack (left: TAC; right: reference system)

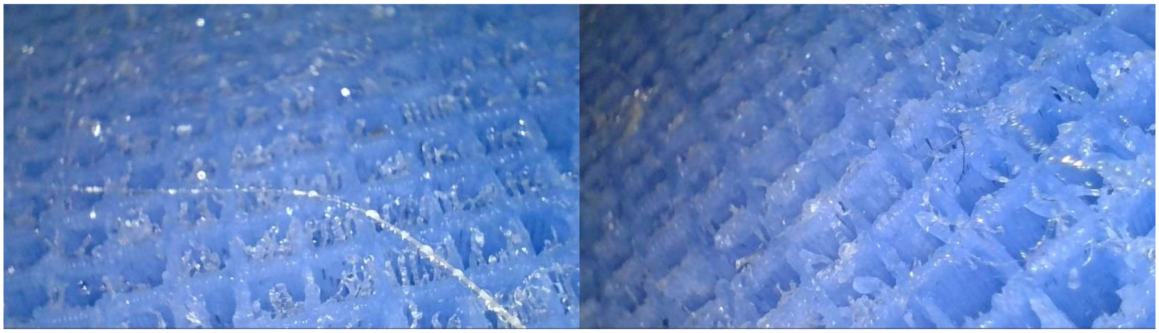

Figure 44: Post-experiment photo of the cold end of the squared mesh stack (left: TAC; right: reference system)

Figure 45: Post-experiment photo of the cold end of the squared mesh stack (left: TAC; right: reference system)

4.2.3 Energy balance for the second set

The speaker has a Sound Pressure Level (SPL) provided my manufacturer as 83 dB. The amplifier, considering 90% efficiency could provide 90W of electrical input. At the distance of 75 mm from the speaker, at the stack, the SPL was estimated to be around 124.8 dB. Using the formula for the conversion between decibels and acoustic power:

$$SPL = 10\log_{10}\left(\frac{P_{acoustic\,power}}{10^{-12}}\right) \tag{4.1}$$

The acoustic power ($P_{acoustic\,power}$) equivalent to 124.8 dB was calculated as 3.02W. Therefore, it can be assumed that the acoustic wave has 3.02W of acoustic power at the stack position (Sengpieaudio.com n.d.). Furthermore, with the assumption that at the end of every experiment, TAC reached thermal equilibrium state as the final temperature gradient (which is just a difference between hot end and cold end temperatures) becomes quasi-constant, the temperature gradient along the stack could be found. Also, considering Case 0 as the maximum undamaged thermal gradient that was achieved, the average for the Cases 1-4 was found in Table 16.

Table 16: Final temperature gradient for different stacks

#	Final temperature gradient (°C)	Average final temperature gradient (°C)
P0	18.2	18.2
P1	15.0	15.3
P2	16.1	
P3	15.8	
P4	14.5	
S0	14.3	14.3
S1	10.7	11.4
S2	11.9	
S3	11.6	
S4	11.5	
C0	16.2	16.2
C1	15.4	15.4
C2	15.5	
C3	15.7	
C4	14.9	

Therefore, heat flow across the stack could be calculated taking into account geometry parameters of every stack, length of the stack (60 mm), PLA thermal conductivity, average final temperature gradient and the formula for the heat flow across the solid body (Bird, Stewart and Lightfoot 2007):

$$q = -kA\frac{\Delta \mathrm{T}}{L} \tag{4.2}$$

where A is the cross-sectional area of the stack, k is the PLA thermal conductivity, L is the length of the stack and ΔT is the final temperature gradient. Also, percentage reduction as a measure of damage done by condensation and continuous vapor feeding to the final temperature gradient was found and reflected in Table 17.

Table 17: Heat flow and damage from condensation

	Case 0 heat flow (W)	Cases 1-4 heat flow (W)	Average heat flow reduction Cases 1-4 vs Case 0, $\left(\frac{\overline{\dot{q}_{1-4}}}{\dot{q}_0} - 1\right) x100\%$ (%)
$\dot{q}_{Parallel}$	0.14	0.12	15.48
$\dot{q}_{Squared}$	0.11	0.09	19.80
$\dot{q}_{Circular}$	0.14	0.13	5.31

Consequently, as it was observed from the calculations results, the circular stack has lowest level of damage from the condensation to the final temperature gradient. Thus, it can be stated that the circular plates stack has better thermoacoustic sustainability in the conditions of high humidity and high-level condensation than other two stacks.

4.3 Conclusion

In this study, the thermoacoustic cooler was built based on Tijani and his team's design with modifications. The working fluid was chosen as air with saturated water vapor generated from a humidifier. The experiments confirmed that the design is working and the TAC operating on the unpressurized air is feasible and can achieve a moderately good temperature drop at the cold end, especially if the system is well insulated and all the possible sources of energy losses are taken into an account (thermal losses minimized by layer of thermal insulation, acoustic and pressure losses minimized by sealing all the possible air leakages, energy losses due to vibrations minimized by tightly fixing the resonator to a heavy object such as massive wood desk). Also, it was observed that the TA phenomenon may indeed enhance the condensation rate and thus improve dehumidification performance. However, it was also observed that the continuous vapor feeding and water harvesting via condensation damaged the thermoacoustic performance and caused reduction in cooling capacity. Moreover, the experiments showed that the stack’s design directly affects thermoacoustic performance and condensation rate. Even the parallel plate stack demonstrated the best thermoacoustic performance and cooling efficiency, circular stack had a better resistance to the damage caused by condensation to the thermoacoustic performance. Thus, it can be concluded that depending on the air humidity and working temperatures, the design of the stack should be carefully selected to balance between the maximum performance and the sustainability of thermoacoustic in accordance to which is more important for the certain application. The potential application of this investigation can be an autonomous thermoacoustic cooler system for water harvesting in arid areas. This work can be used to evaluate how the TA effect can be affected by the condensation if humid air is used as the working fluid.

CHAPTER V

FUTURE WORK

5.1 Overview

The original idea for this experiment was to test the possibility to use the TAC as a water harvesting/dehumidifier device. The experimental results confirmed to some degree that the TAC can indeed enhance condensation rate and thus water harvesting by generating temperature gradient. In general, it could be stated that the condensation performance relied basically on two factors:

- Thermoacoustic performance (and thus the biggest temperature drop that could be achieved on the cold end of the stack).
- The geometry and material properties of the stack (as it the part where condensation directly occurs, and water can be removed from).

Consequently, in order to enhance the condensation, any of these two factors can be addressed and studied. As for TA performance, there are several possible ways to enhance the condensation. The main design of the TAC can be changed from half-wavelength to quarter-wavelength or from standing wave TAC to travelling wave and compare their TA performance if some of the reference parameters are maintained the same (i.e. speaker's power rate, stack's design and geometry). Also, the thermal and sound insulation provides a room for improvement (in theory, better insulation leads to higher TA performance).

However, alteration of the TAC design could cause radical changes in the whole experiment. Second route such as working with the stack and alternating some of its parameters was considered as more appropriate in the frame of this study. Therefore, there was an idea to investigate how the roughness of the stack's plates could affect the condensation rate. Theoretically, roughness inside the stack (shown in Figure 46) enhance condensation as it provides points of surface imperfection acting as nucleation sites for droplets and forming dropwise condensation (Rose and Glicksman 1973).

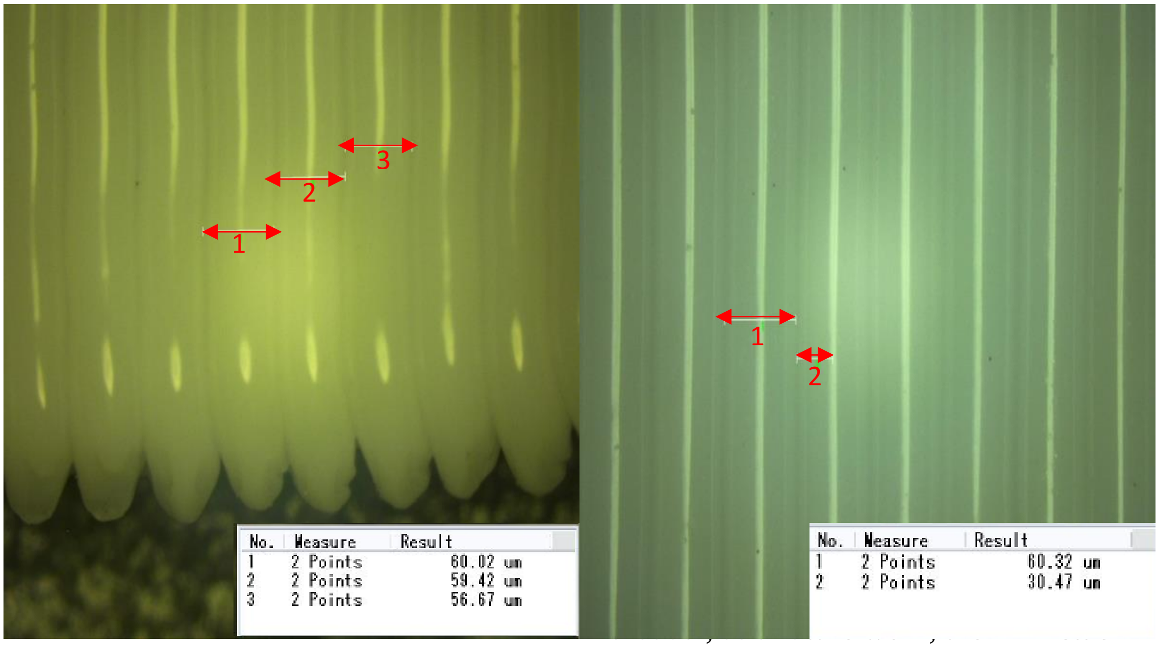

Figure 46: Microscope image of a PLA plate surface texture

Consequently, the stack can be treated with acetone vapor to make the surface smoother and run the same experiments to empirically study the influence of surface roughness to water condensation rate.

5.2 Additional challenges

The TAC has demonstrated water harvesting performance in the lab conditions and fed with the humid air. However, there are still some unstudied problems left that are related to water harvesting in field conditions. They include two major ones:

- What would be the source of an acoustic wave.
- How to provide fresh air into a system.

The autonomous source of an acoustic wave in the field conditions could be another thermoacoustic engine that utilizes solar heat to create a temperature gradient and convert it into an acoustic wave.

The fresh air into the system can be provided by small orifice in the resonator. The insertion of hygrometer probe through a small bore, performed in the first set of experiments, affirms that a small breach in the resonator integrity did not severely damages TA performance and thus orifices can be used to provide fresh air and air mixing with the ambient in general. Also, it should be investigated whether it is more efficient to feed fresh air from the hot end of the stack or from the cold end of the stack location. From the geometrical point of view, the feeding orifice might be better to be located beneath cold end as it could create a natural air flow due to density difference between incoming warmer fresh air and colder air descending from the cold end.

REFERENCES

Jinshah, B. S., R. Ajith Krishnan, and V. S. Eep. 2013. "Study on A Standing Wave Thermoacoustic Refrigerator Made of Readily Available Materials." *International Journal of Scientific and Research Publications* 3.

Atis, C. A. A., M. Sarker, and M. Ehsan. 2014. "Study of Thermoacoustic Phenomenon in a Rijke Tube." *Procedia Engineering* 569-574.

Babaei, H., and K. Siddiqui. 2008. "Design and optimization of thermoacoustic devices." *Energy Conversion and Management* 49(12), 3585-3598.

Backhaus, S., and G. W. Swift. 1999. "A thermoacoustic Stirling heat engine." *Nature* 399, 335-338.

Bird, B. R., W. E. Stewart, and E. N. Lightfoot. 2007. *Transport Phenomena (2nd ed.).* John Wiley & Sons, Inc (ISBN 978-0-470-11539-8), p. 266.

Chatterjee, A., M. M. Derby, Y. Peles, and M. K. Jensen. 2014. "Enhancement of condensation heat transfer with patterned surfaces." *Int. J. Heat Mass Transfer* (71) 675-681.

Corbett, F., T. Harter, and M. Sneed. 2011. "Subsidence due to Excessive Groundwater Withdrawal in the San Joaquin Valley, California." *AGU Fall Meeting Abstracts.*

Cuan, Z., and Y. Chen. 2017. "Analyze of laminar flow and boiling heat transfer characteristics of R134a in the horizontal micro-channel under low temperature condition. DOI:10.1016/j.proeng.2017.10.106." *ISHVAC China* 2933-2939.

Culham, J. R. 2011. "Brayton Cycle." *Engineering Courses Online.* November 15. Accessed Feb 5, 2019. http://www.mhtlab.uwaterloo.ca/courses/me354/lectures/pdffiles/web7.pdf.

Engineering ToolBox. 2004. *Density of Moist Humid Air.* Accessed August 10, 2018. https://www.engineeringtoolbox.com/density-air-d_680.html.

Gatignol, Renée. 2007. "On the history term of Boussinesq–Basset when the viscous fluid slips on the particle." *C. R. Mecanique* (335) 606-6016.

Hiller, R. A., and G. W. Swift. 2000. "Condensation in a steady-flow thermoacoustic refrigerator." *The Journal of the Acoustical Society of America* 108(4), 1521-1527.

Hou, M., Z. Wu, G. Yu, J. Hu, and E. Luo. 2018. "A thermoacoustic Stirling electrical generator for cold exergy recovery of liquefied nature gas." *Applied Energy* 226, 389-396.

Izmailov, V. P., O. V. Karagioz, and V. M. Shakhparonov. 2015. "Hysteresis losses in oscillatory systems." *International Journal of Non-Linear Mechanics* (77) 307–311.

Jaworski, A. J. n.d. *Thermoacoustics.* Accessed Apr 15, 2019. https://sites.google.com/site/professorarturjjaworski/thermoacoustics.

Jin, T., J. Huang, Y. Feng, R. Yang, K. Tang, and R. Radebaugh. 2015. "Thermoacoustic prime movers and refrigerators: Thermally powered engines without moving components." *Energy* 93, 828-853.

Jina, T., J. Huanga, Y. Fenga, R. Yanga, K. Tanga, and R. Radebaugh. 2015. "ReviewThermoacoustic prime movers and refrigerators: Thermally poweredengines without moving components." *Energy* (93), 828-853.

Jordan, D. 2017. *Sonotherm Wins CRCF Commercialization Award to Develop Thermoacoustics Technology!* Accessed Apr 15, 2019. http://www.dojoresearch.com/sonotherm/.

Kalra, S., K. P. Desai, H. B. Naik, and M. D. Atrey. 2015. "Theoretical Study on Standing Wave Thermoacoustic Engine." *Physics Procedia* (67), 456-461.

Kang, H., G. Zhou, and Q. Li. 2010. "Thermoacoustic effect of traveling–standing wave." *Cryogenics* 50(8), 450-458.

Karimi, M., G. Akdogan, K. H. Dellimore, and S. M. Bradshaw. 2012. "Comparison of different drag coefficient correlations in the cfd modelling of a laboratory-scale rushton-turbine flotation tank." *CSIRO Australia.*

Ke, H., Y. He, Y. Liu, and F. Cui. 2012. "Mixture working gases in thermoacoustic engines for different applications." *Int. J. Thermophys.*

Legg, Roger. 2017. "Chapter 1 - Properties of Humid Air." In *Air Conditioning System Design*, by Roger Legg, 1-28. Butterworth-Heinemann.

Maxime Perier-Muzet, Jean-Pierre Bedecarrats, Pascal Stouffs, Jean Castaing-Lasvignottes,, M. Perier-Muzet, J.P. Bedecarrats, P. Stouffs, and J. Castaing-Lasvignottes. 2014. "Design and dynamic behaviour of a cold storage system combined with a solar powered thermoacoustic refrigerator." *Applied Thermal Engineering* (68) 115-124.

Michaelides, E. E., and A. Roig. 2011. "A Reinterpretation of the Odar and Hamilton Data on the Unsteady Equation of Motion of Particles." *AIChE Journal* (57) 2997-3002.

Pelesko, J. A., and D. H. Bernstein. 2003. *Modeling MEMS and NEMS.* CRC Press.
2019. "Relative Humidity." *slideplayer.com.* Accessed April 15, 2019. https://slideplayer.com/slide/4787254.

Rose, J. W., and L. R. Glicksman. 1973. "Dropwise Condensation-The Distribution of Drop Sizes." *Int. J. Heat and Mass Transfer* (11) 411– 425.

SD3D.com. 2017. "PLA Technical Data Sheet." *SD3D.* Accessed July 1, 2018. https://www.sd3d.com/wp-content/uploads/2017/06/MaterialTDS-PLA_01.pdf.

Sengpieaudio.com. n.d. *Soundpower calculator.* Accessed February 25, 2019. http://www.sengpielaudio.com/calculator-soundpower.htm.

SHARCNET. 2009. "Evaporation-Condensation Model." *SHARCNET - ANSYS Manual.* January 23. Accessed May 19, 2017. https://www.sharcnet.ca/Software/Ansys/17.0/en-us/help/flu_th/flu_th_sec_mp_evap_cond.html.

Southard, John. 2006. "Introduction to Fluid Motions, Sediment Transport, and Current-Generated Sedimentary Structures." *MIT Open Courseware.* Accessed Aug 4, 2018. https://ocw.mit.edu/courses/earth-atmospheric-and-planetary-sciences/12-090-introduction-to-fluid-motions-sediment-transport-and-current-generated-sedimentary-structures-fall-2006/course-textbook/ch3.pdf.

Swift, G. W. 1988. "Thermoacoustic engines." *Journal of the Acoustical Society of America* (84), 1146–1180.

Tang, K., Z. J. Huang, T. Jin, and G. B. Chen. 2009. "Influence of acoustic pressure amplifier dimensions on the performance of a standing-wave thermoacoustic system." *Applied Thermal Engineering* 29(5-6), 950-956.

Tasnim, S. H., S. Mahmud, and R. A. Fraser. 2012. "Effects of variation in working fluids and operating conditions on the performance of a thermoacoustic refrigerator." *International Communications in Heat and Mass Transfer* 39(6), 762-768.

Tijani, M. E. H., J. C. H. Zeegers, and A. T. A. M. De Waele. 2002. "Construction and performance of a thermoacoustic refrigerator." *Cryogenics* 42(1), 59-66.

Urieli , Israel. 2008. *MATLAB program for plotting a Simplified Psychrometric Chart.* March 7. Accessed September 14, 2018. https://www.ohio.edu/mechanical/thermo/applied/chapt.7_11/psychro_chart/psychro.html .

Wheatley, J., T. Hofler, G. W. Swift, and A. Migliori. 1985. "Understanding some simple phenomena in thermoacoustics with applications to acoustical heat engines." *American journal of physics* 53(2), 147-162.

Yu, G., W. Dai, and E. Luo. 2010. "CFD simulation of 300Hz thermoacoustic standing wave engine." *Cryogenics* (50), 615-622.

Zhu, C., L. Genfan, Y. Jianxiong, and H. Xu. 2015. "Experimental investigation of non-stationary motion of single small spherical particles in an upward flow with different velocities." *Powder Technology* (273) 111–117.

Zimmerman, , O. T., and I. Lavine. 1964. "Psychrometric Tables and Charts." In *Industrial Research Services*, by O. T. Zimmerman, and I. Lavine. Dover, New Hampshire: Industrial Research Services, Inc.

Zolpakar, N. A., N. Mohd-Ghazali, R Ahmad, and T. Maré. 2017. "Performance of a 3D-printed stack in a standing wave thermoacoustic refrigerator." *Energy Procedia* 105, 1382-1387.

APPENDIX

APPENDIX A

MATLAB CODE

```
%%MATLAB Code developed by Aibek Bekkulov, Graduate Mechanical Engineering
%%student at UTRGV 2017-2019. This code allows to construct COP plot to
%%choose optimal stack's parameters for the half-wavelength air-operated
%%standing wave thermoacoustic cooler (thermoacoustic refrigerator, TAC)

%%Initialization of the program
clear all; clc; close all;

%% Sound wave and helium properties
v_sound = 344; %sound speed (m./s)
f = 110; %sound frequency (Hz)
%Half wavelegth shoud be around 155 cm (length of the choosen resonator)
Lambda = v_sound/f; %wavelength (m)
k = 2*pi/Lambda; %wavenumber
K_gas = 0.02624; %thermal conductivity of Air (W/m.K)
omega = 2*pi*f; %angular velocity of sound wave (rad./s)
M = 0.1;    %acoustic Mach number
rho_gas = 1.2041;   %Air's density @20C (kg./m3)
mu_gas = 0.000018205; %Air's dynamic viscosity (Pa.s)
C_p = 1010; %Isobaric specific heat of Air (J/kg.K)
C_v = 718;  %Isohoric specific heat of Air (J/kg.K)
p_0 = M*rho_gas*v_sound^2;  %dynamic pressure (Pa)
%%p_0 = 35;     %actual pressure variations from Boss Audio 125W speaker
p_m = 1013250;  %average pressure (Pa);
D = p_0/p_m;    %dynamic ratio
gamma = C_p/C_v;  %Cp./Cv gas ratio for helium

%%Stack properties
%L_s =0:0.001:0.2; %stack length (m)
%x_s = 0:0.001:0.2; %stack's center position (m)
[x_s, L_s] = meshgrid(0.01:0.001:1.6,0.05:0.01:0.06);
[L_s_size, x_s_size] = size(x_s);

th = 0.0005; %plate's thickness (m)
%T_h = 313; %hot end temperature (K)
%T_c = 283; %cold end temperature (K)
```

```
T_h = 300; %hot end temperature (K)
T_c = 290; %cold end temperature (K)
T_m = (T_h+T_c)/2; %mean temperature (K)
T_diff = T_h-T_c; %temperature difference (K)

%%Calculated parameters
delta_k = (2*K_gas/(rho_gas*C_p*omega))^0.5;  %thermal penetration depth
delta_v = (2*mu_gas/(rho_gas*omega))^0.5;  %viscous penetration depth
Pr = (delta_v /delta_k)^2;  %Prandtl's number
s_s = 3*delta_k;    %plates spacing (m)
y_0 = s_s/2;    %half spacing (m)
B = s_s/(s_s+th);   %blockage ratio
disp(delta_k)

 %% Normalized parameters
T_mn = T_diff/T_m;  %normalized temperature difference
L_sn = L_s.*k; %normalized stack length
x_sn = x_s.*k; %normalized stack's center position
delta_kn = delta_k/y_0; %normalized thermal penetration depth
lambda_n = 1 - (Pr)^0.5*delta_kn+0.5*Pr*delta_kn^2; %lambda coefficient

 Q_cn =
((delta_kn.*D.^2.*sin(2.*x_sn))./(8.*gamma.*(1+Pr).*lambda_n)).*((T_mn.*tan(x_sn).*(1+Pr.^
0.5+Pr))./((gamma-1).*B.*L_sn.*(1+Pr.^0.5)) - (1+Pr.^0.5-Pr.^0.5.*delta_kn));    %normalized
heat flow
W_n = (((delta_kn.*L_sn.*D.^2.*(gamma-
1).*B.*(cos(x_sn)).^2)./(4.*gamma)).*(T_mn.*tan(x_sn)./(B.*L_sn.*(gamma-
1).*(1+Pr.^0.5).*lambda_n) - 1)) -
(delta_kn.*L_sn.*D.^2.*Pr.^0.5.*(sin(x_sn)).^2./(4.*gamma.*B.*lambda_n)); %normalized
acoustic power
COP_n = Q_cn./W_n;   %normalized COP

%%preallocation
Q_cn = nan(L_s_size, x_s_size);
W_n =  nan(L_s_size, x_s_size);
COP_n = nan(L_s_size, x_s_size);
for j = 1:L_s_size
   for i = 1:x_s_size
       if (0.5*L_s(j,1) <= x_s(1,i))
           Q_cn(j,i) =
((delta_kn.*D.^2.*sin(2.*x_sn(1,i)))./(8.*gamma.*(1+Pr).*lambda_n)).*((T_mn.*tan(x_sn(1,i)).
*(1+Pr.^0.5+Pr))./((gamma-1).*B.*L_sn(j,1).*(1+Pr.^0.5)) - (1+Pr.^0.5-Pr.^0.5.*delta_kn));
%normalized heat flow
           W_n(j,i) = (((delta_kn.*L_sn(j,1).*D.^2.*(gamma-
1).*B.*(cos(x_sn(1,i))).^2)./(4.*gamma)).*(T_mn.*tan(x_sn(1,i))./(B.*L_sn(j,1).*(gamma-
1).*(1+Pr.^0.5).*lambda_n) - 1)) -
```

```
(delta_kn.*L_sn(j,1).*D.^2.*Pr.^0.5.*(sin(x_sn(1,i))).^2./(4.*gamma.*B.*lambda_n));
%normalized acoustic power
            COP_n(j,i) = Q_cn(j,i)./W_n(j,i);   %normalized COP
%           if (COP_n(j,i) < 0)
%               COP_n(j,i) = 0;
%           end
        else
            COP_n(j,i) = 0;
        end
    end
end

 %%Plotting results (dimensionless)
surf(x_sn, L_sn, COP_n)
title('Dimensionless, COP vs x_sn, L_sn')
xlabel('x_s_t_a_c_k_\__n');
ylabel('L_s_t_a_c_k_\__n');
zlabel('COP');

 %%Plotting results (with dimensions)
figure
mesh(x_s, L_s, COP_n)
title('With dimensions, COP vs x_s, L_s')
xlabel('x_s (stack''s position, m)');
ylabel('L_s (stack''s length, m)');
zlabel('COP');
```

APPENDIX B

LabView Program

Three thermocouples were connected to NI myDAQ module which was connected through USB cable to a laptop. Custom made LabView code was developed to take readings from thermocouples (indicated as T1 Hot End, T2 Cold End and T3 Water). The illustration of the LabView program is presented below in Figure 47. It consists front panel with GUI interface (left half of the figure) and Block Diagram with the implemented programming logic. The data was acquiring every 2 seconds when the code was run.

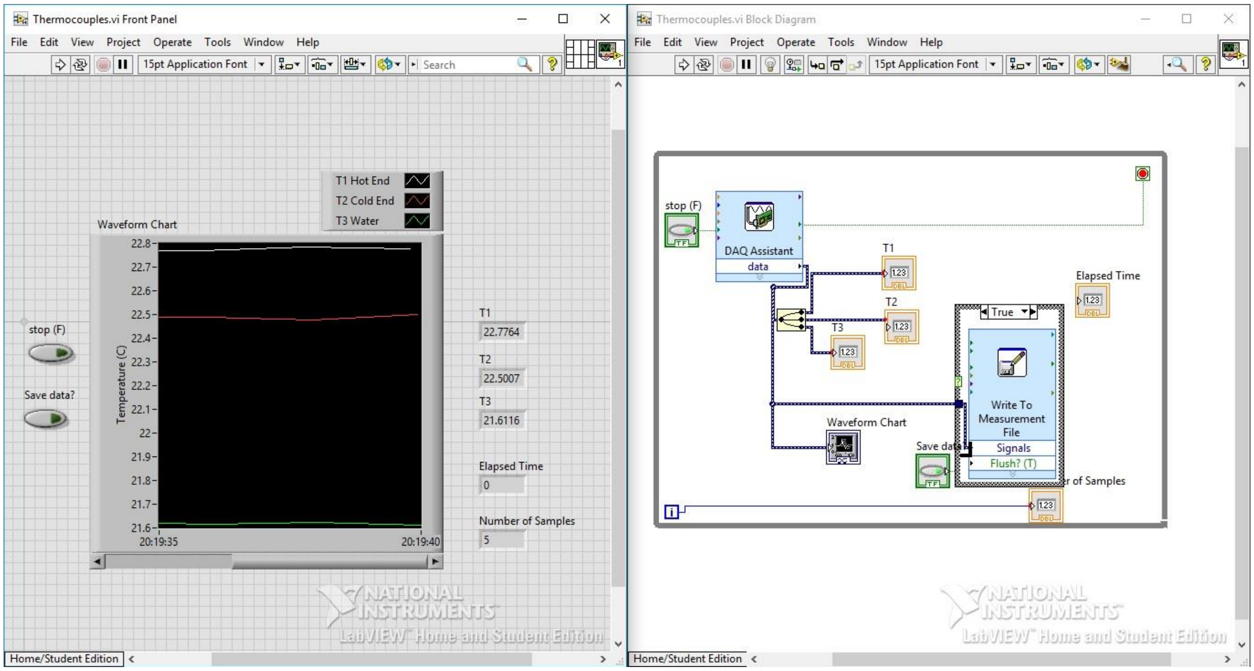

T1 22.7764

T2 22.5007

T3 21.6116

Elapsed Time 0

Number of Samples 5

Figure 47: LabView program for thermocouple

APPENDIX C

Psychometric chart

A simple psychometric chart is used to manually find dew point if the air temperature (correspond to dry bulb temperature) and relative humidity are known. The horizontal line to wet bulb temperature curve gives dew point temperature for the point of intersection between dry bulb temperature and relative humidity. Figure 48 provides such psychometric chart (Urieli 2008).

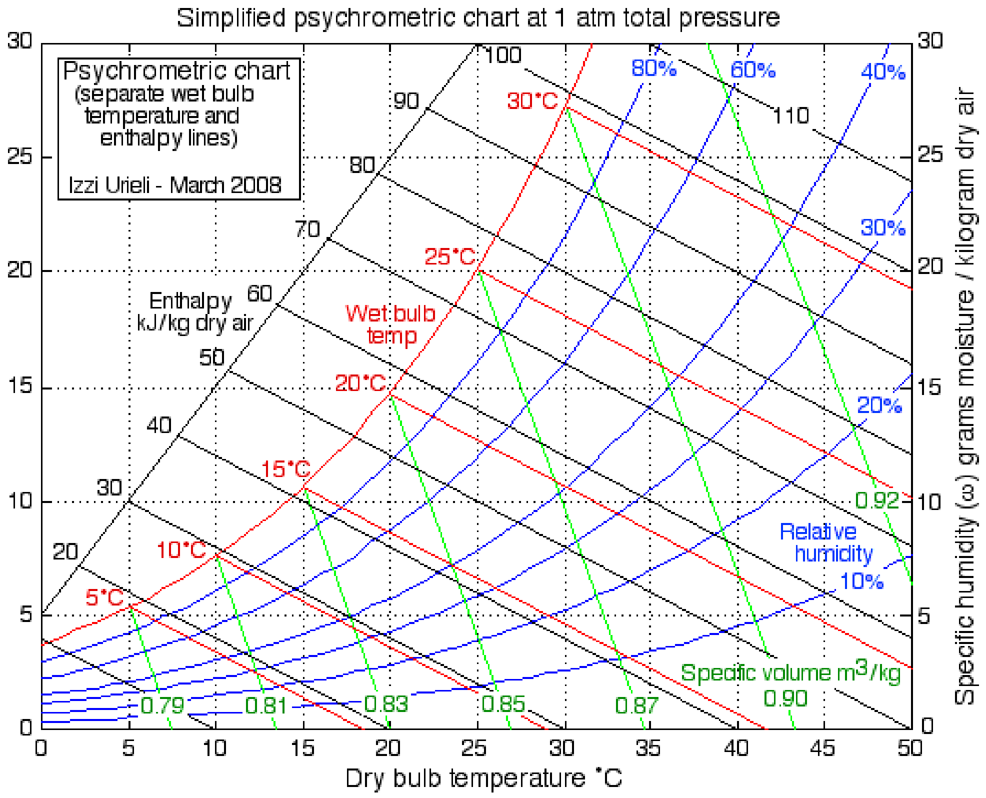

Figure 48: Psychometric chart

APPENDIX D

Second set of experiments – thermocouples readings

Thermocouples readings for the second set of experiments, including parallel plates stack, squared mesh stack and circular plates stack cases, are presented below:

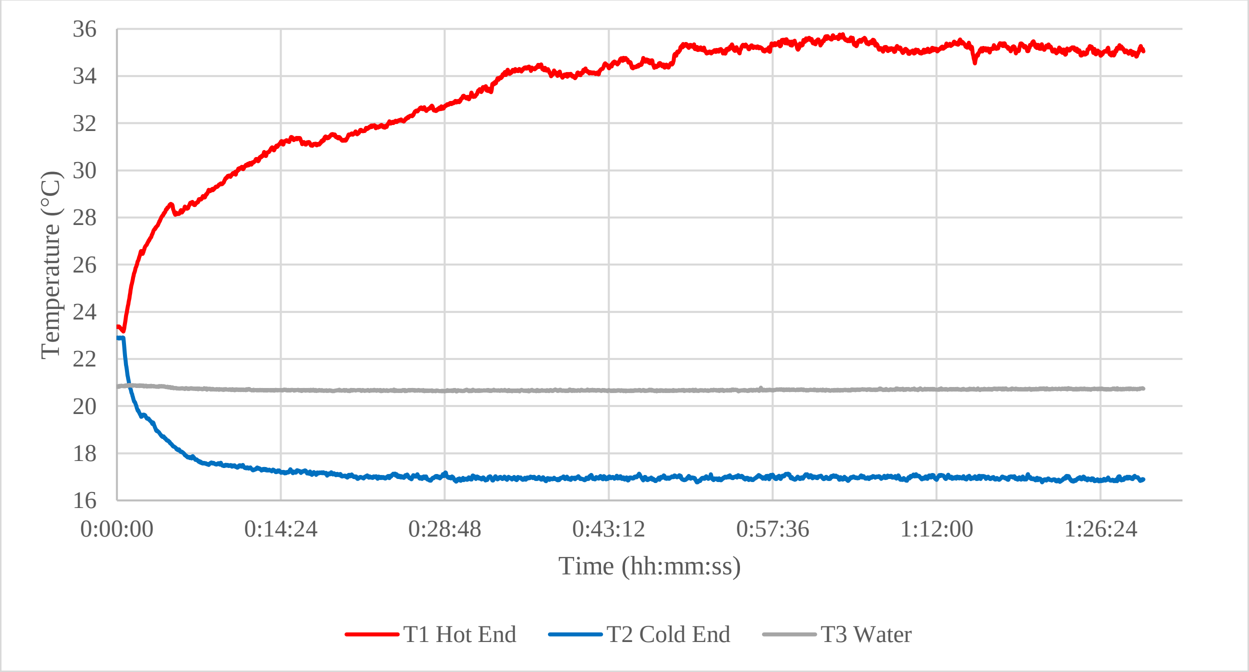

Figure 49: P0 case (parallel plates stack)

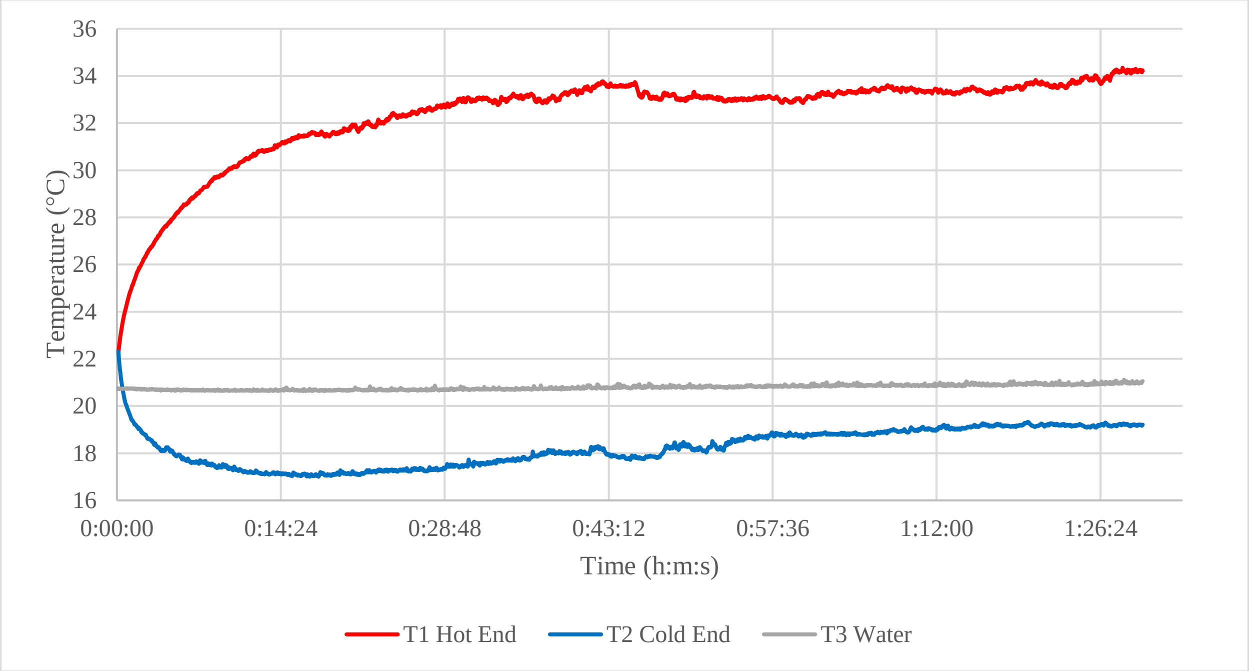

Figure 50: P1 case (parallel plates stack)

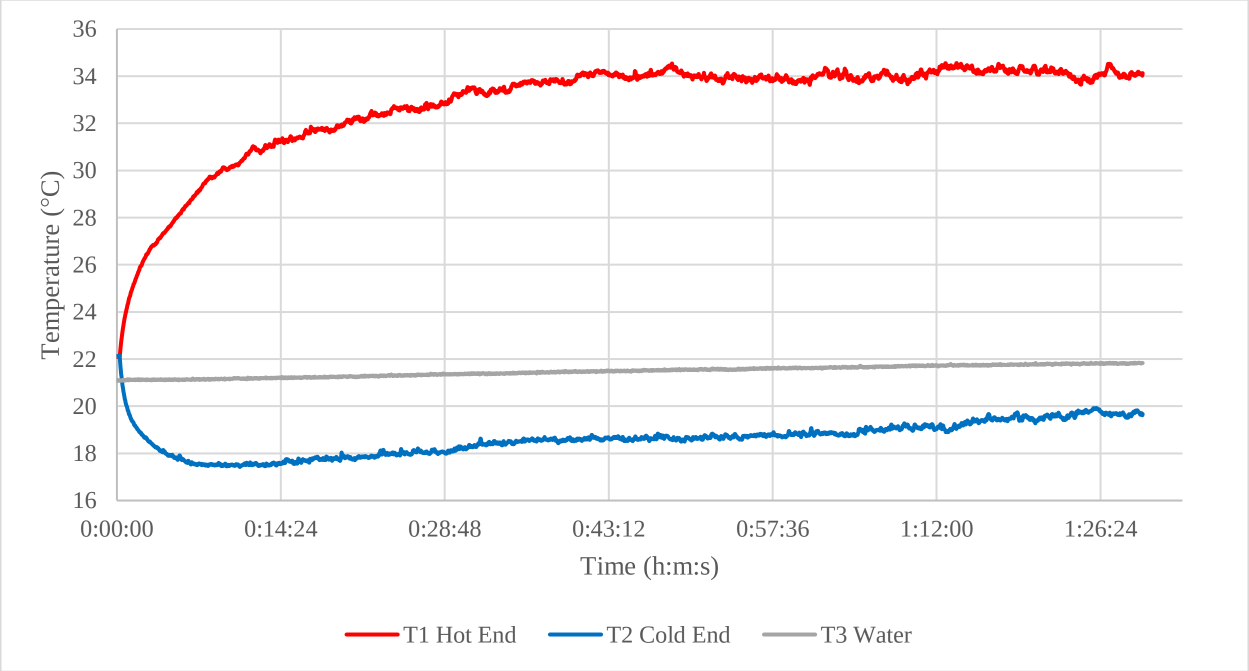

Figure 51: P2 case (parallel plates stack)

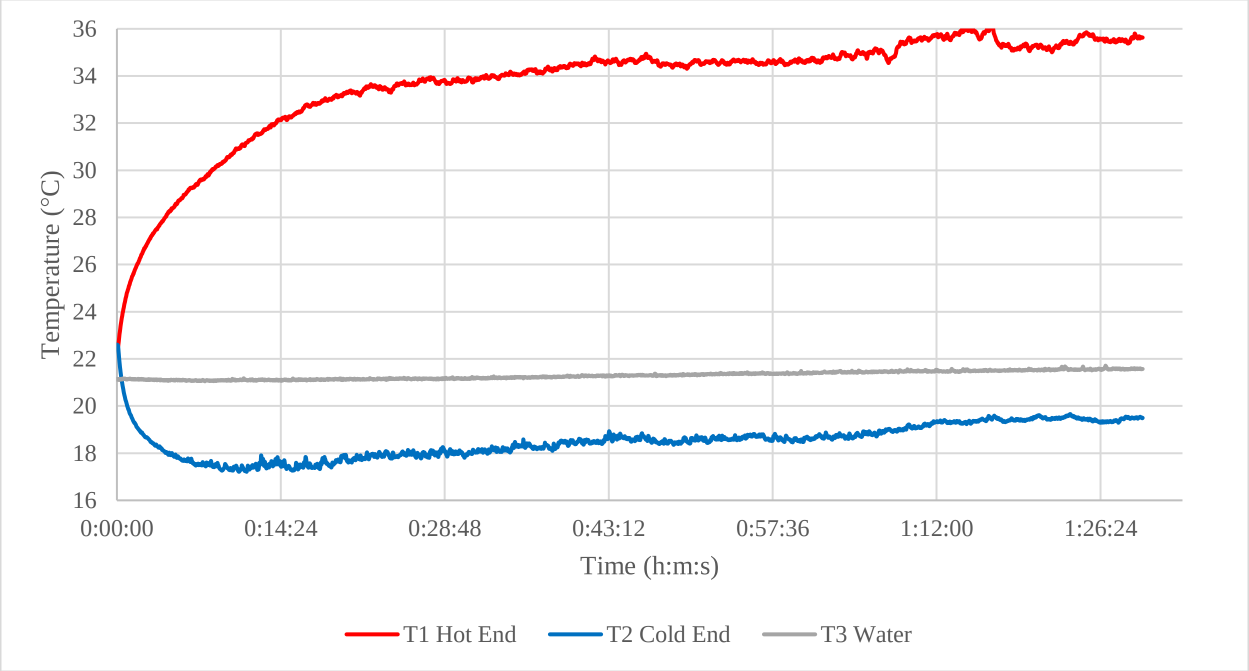

Figure 52: P3 case (parallel plates stack)

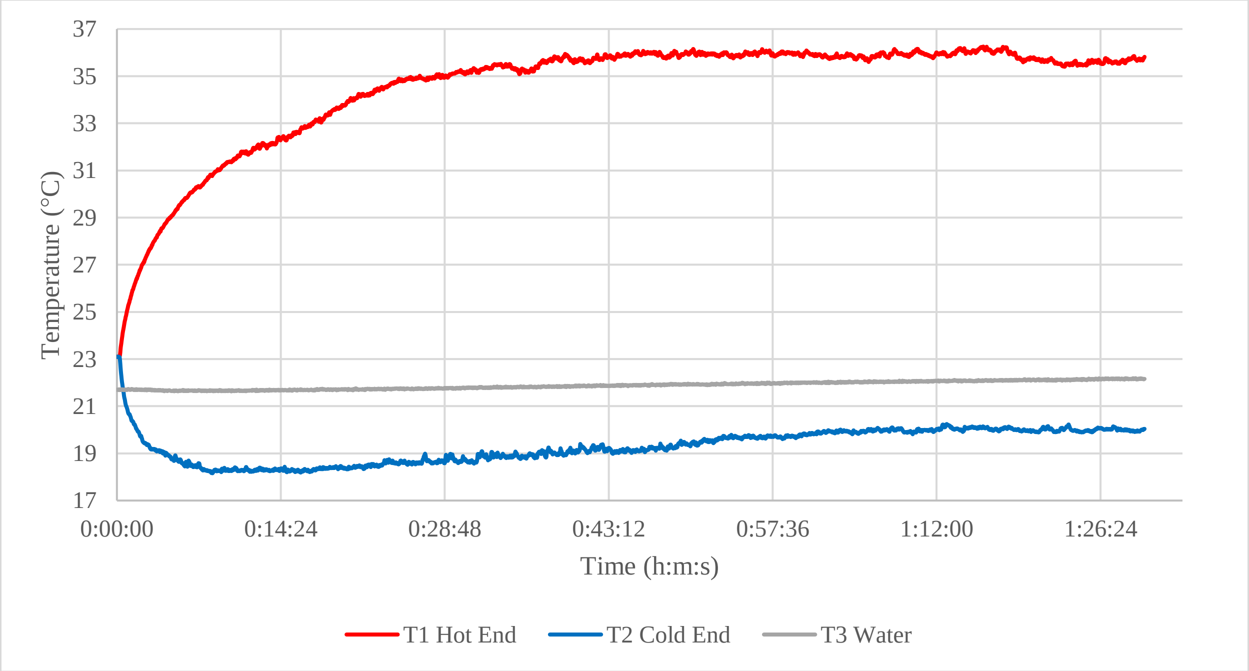

Figure 53: P4 case (parallel plates stack)

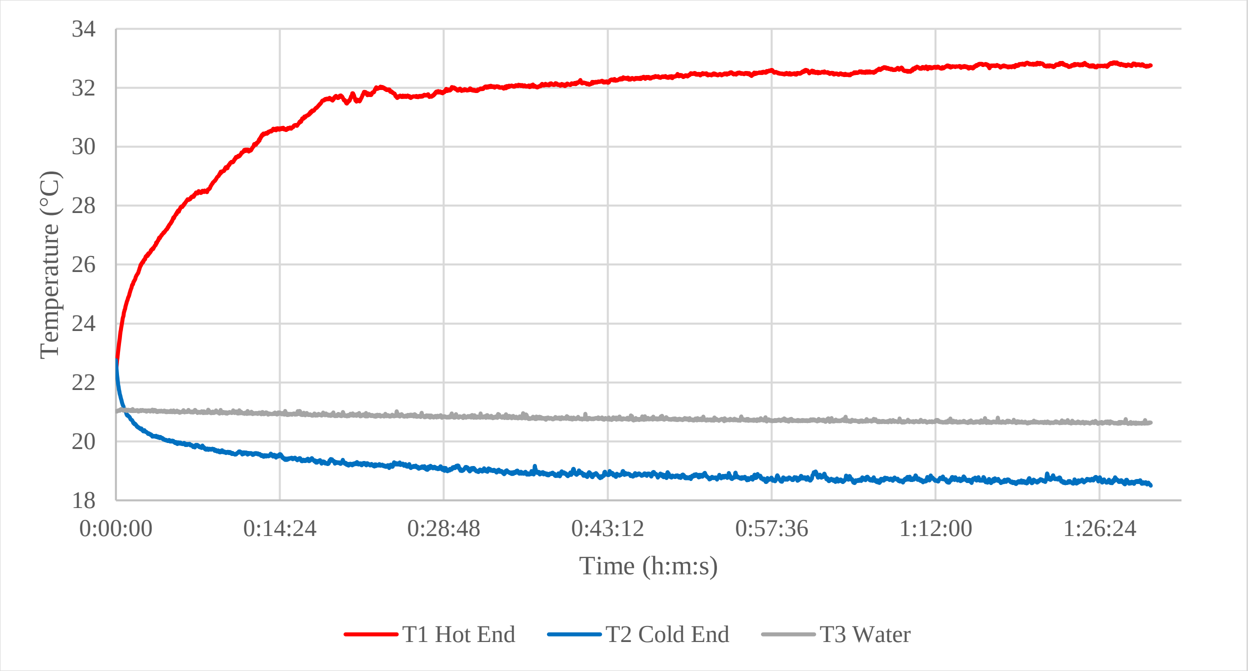

Figure 54: S0 case (squared mesh stack)

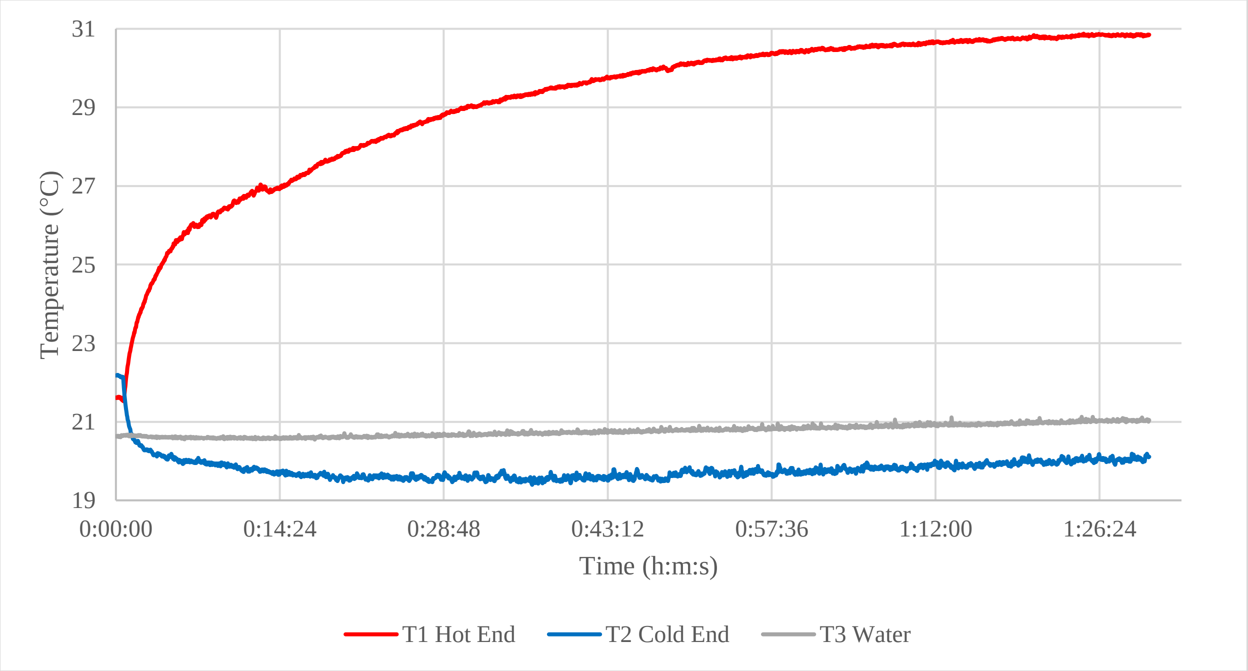

Figure 55: S1 case (squared mesh stack)

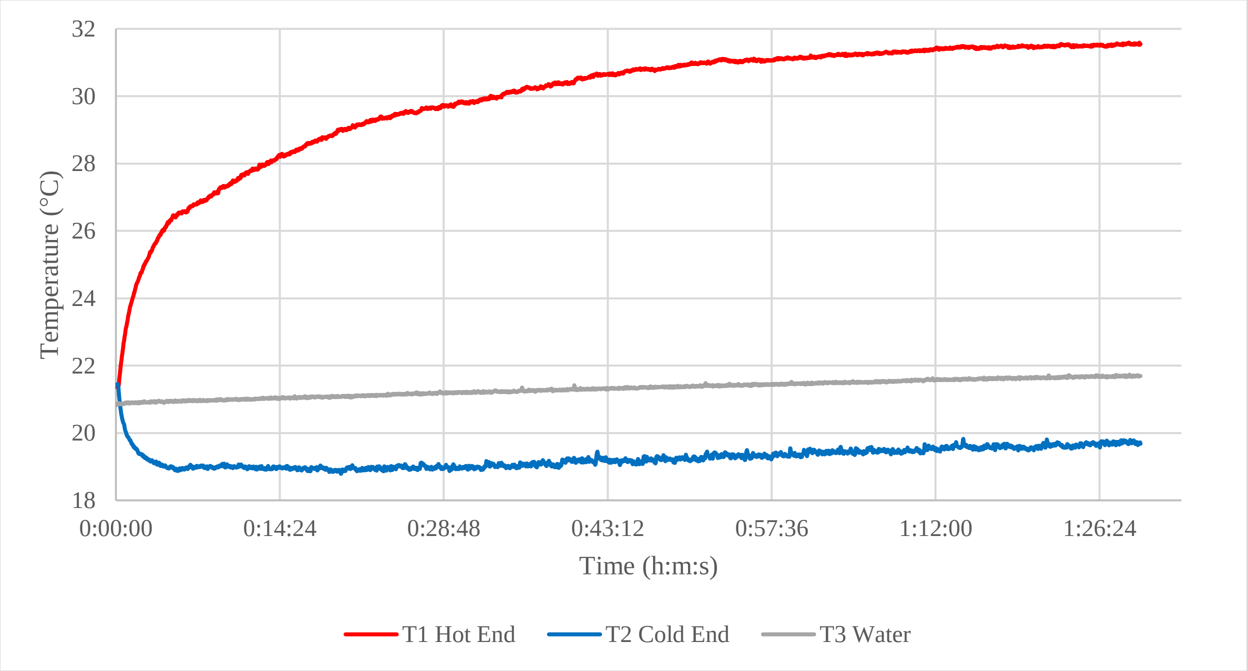

Figure 56: S2 case (squared mesh stack)

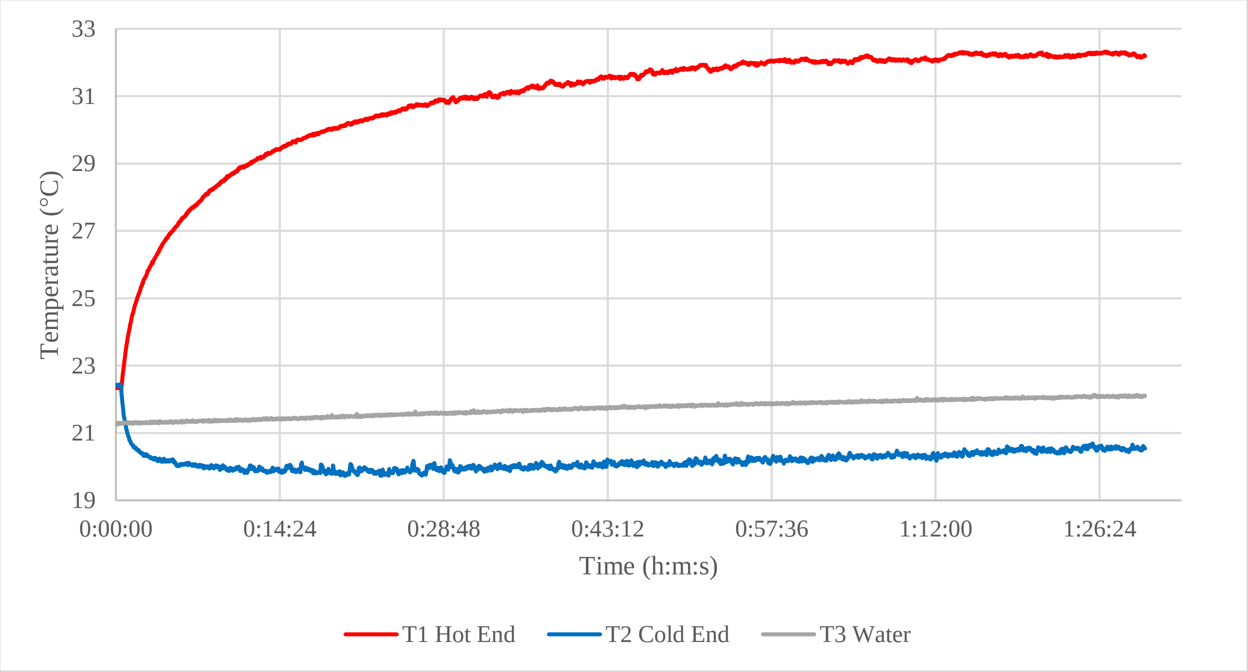

Figure 57: S3 case (squared mesh stack)

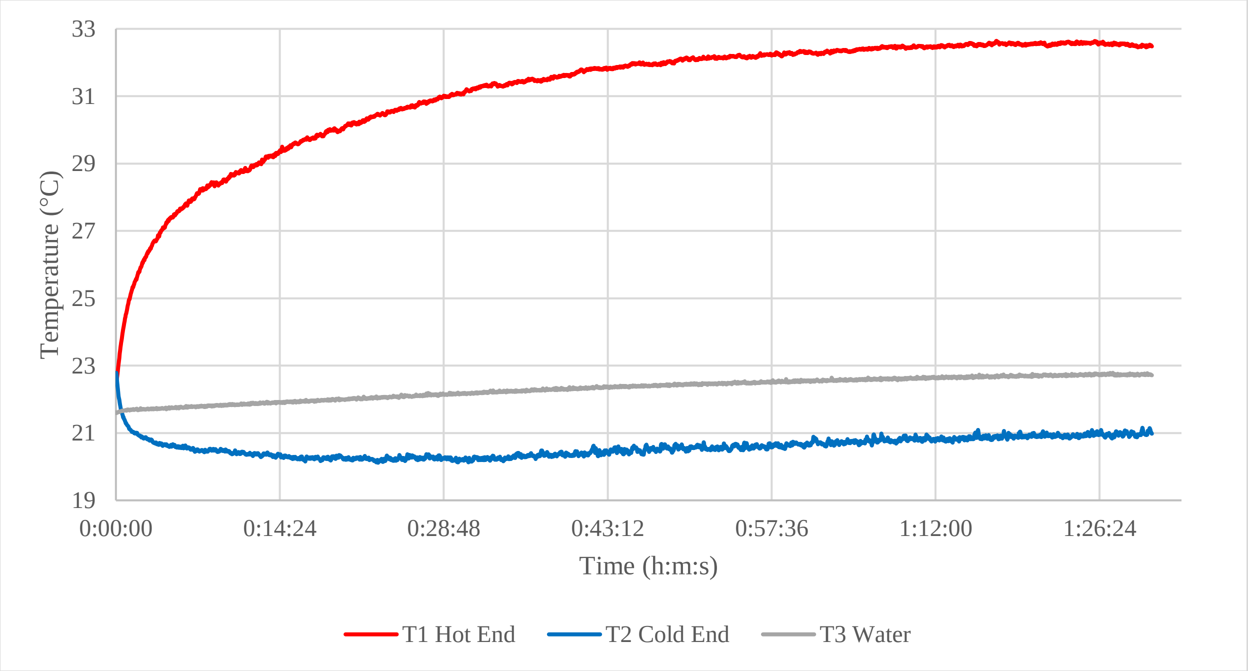

Figure 58: S4 case (squared mesh stack)

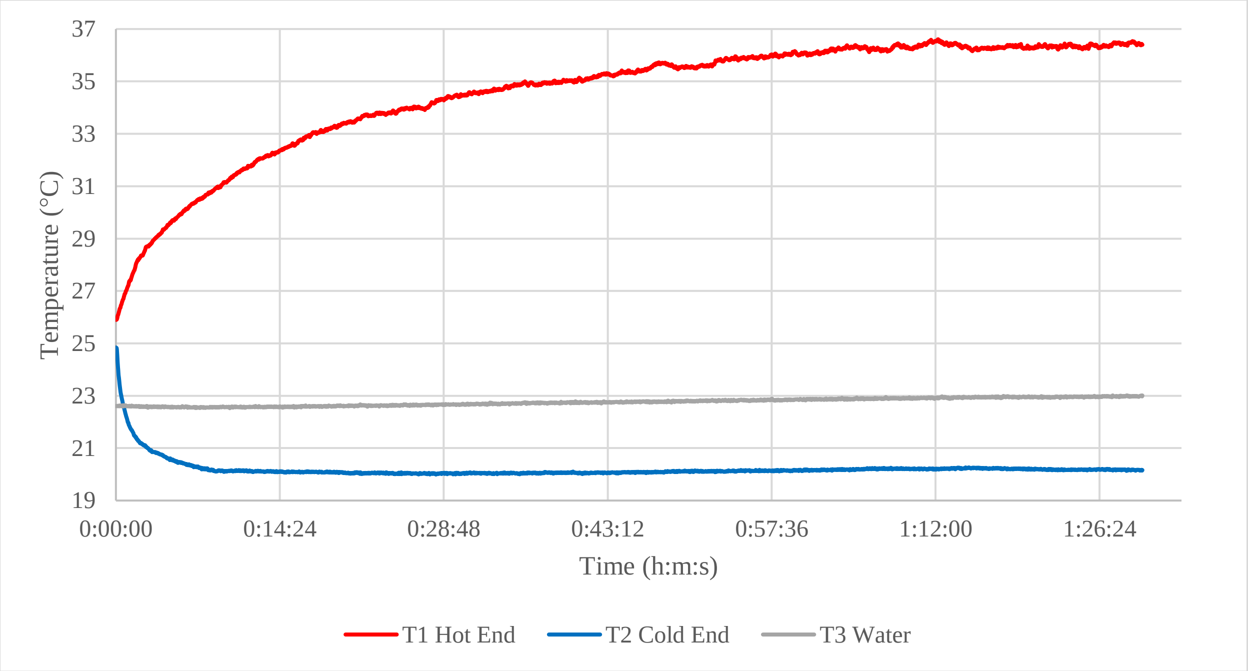

Figure 59: C0 case (circular plates stack)

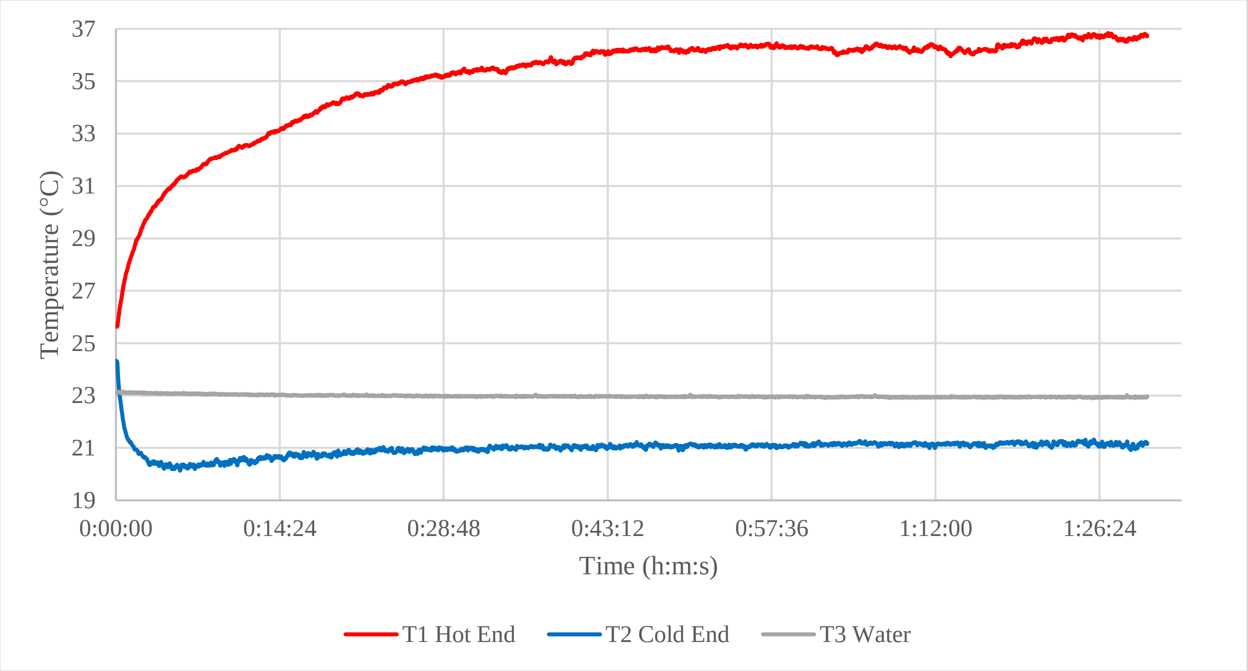

Figure 60: C1 case (circular plates stack)

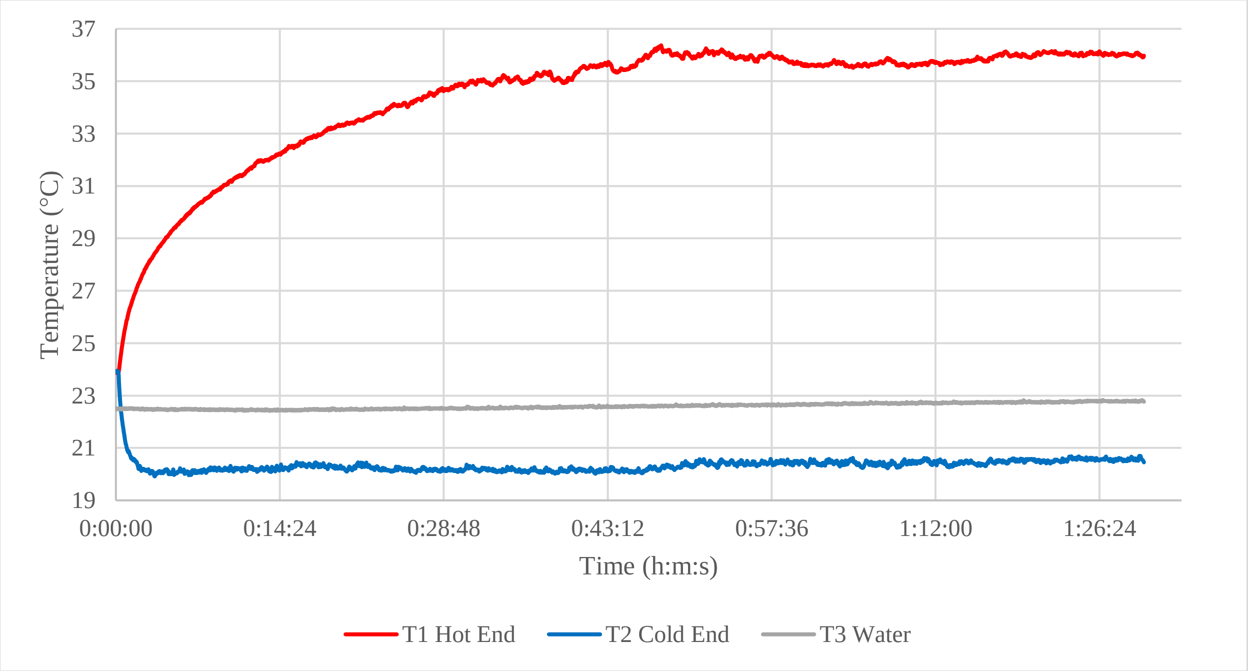

Figure 61: C2 case (circular plates stack)

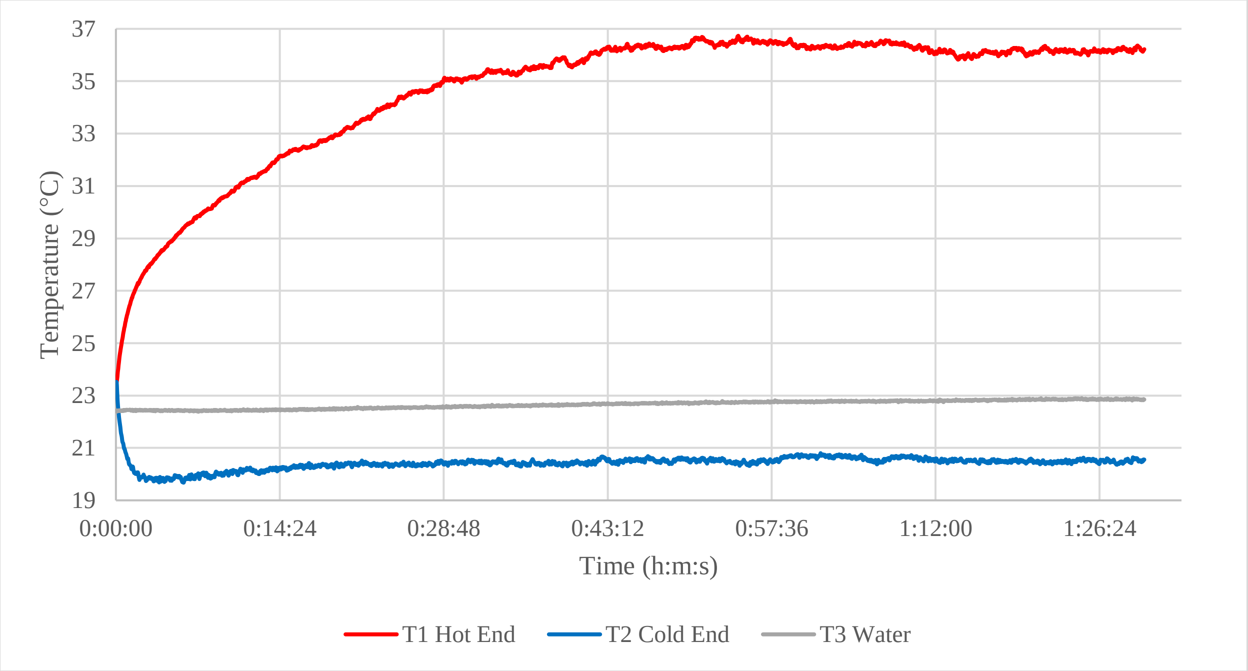

Figure 62: C3 case (circular plates stack)

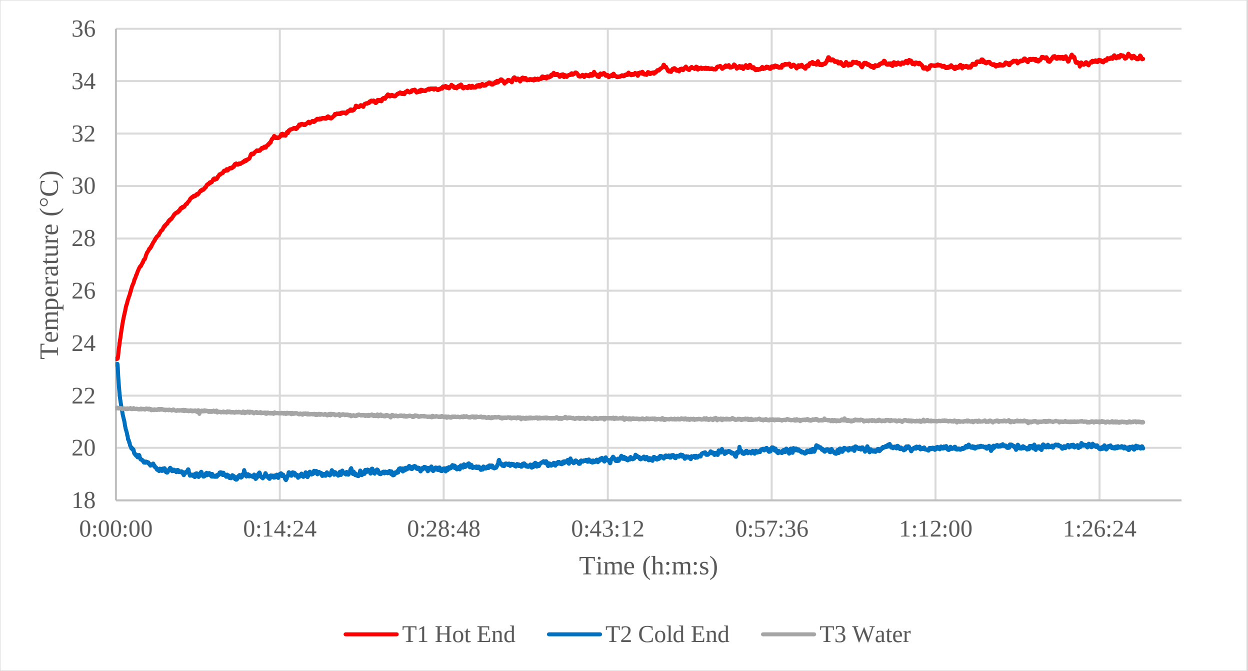

Figure 63: C4 case (circular plates stack)

APPENDIX E

Force Decomposition of Medium Reynolds Number Oscillating Flow over a Submerged Sphere

One of the challenges that emerged from the condensation in the thermoacoustic cooler was to have a mathematical model that describes how the standing wave, or in other words oscillating flow, affects the condensed water droplet (that can be simplified as a sphere). Therefore, I conducted an additional research on the topic of "Force Decomposition of Medium Reynolds Number Oscillating Flow Over a Submerged Sphere" that was published as a conference paper for the "ASME International Mechanical Engineering Congress and Exposition, Volume 7: Fluids Engineering" that was hosted in Pittsburgh, PA on November 9-15, 2018.

INTRODUCTION

The prediction of unsteady motion of particles in a carrier fluid is an important engineering problem. Numerous practical examples include fuel droplets in combustion processes, aerosol dispersion, movement of microorganisms in a fluid, sedimentations of solid particles in rivers, oceans and other water bodies. Therefore, one of the most important parameters in all such problems is the quantification of the forces acting on the particle.

Boussinesq in 1885 and Basset in 1888 (Gatignol 2007) developed a force equation for an unsteady motion of a sphere in creeping flow conditions ($Re << 1$) with an additional *historical term of Basset*, extending the force equation to the form of:

$$\mathrm{F_{total}} = \mathrm{F_{drag}} + \mathrm{F_{virtual\ mass}} + \mathrm{F_{history}} \tag{E.1}$$

Both the virtual mass force (in some literature referred as added mass force) and the history forces are unsteady by their nature. Odar and Hamilton (Michaelides and Roig 2011) conducted several sets of experiments with an oscillating sphere in a tank filled with stagnant oil, and they concluded a semi-empirical coefficient based on Boussinesq-Basset expression for flow in a diapason of Re between 0 and 62.

The drag force proposed in the original work (Michaelides and Roig 2011):

$$\mathrm{F_{drag}} = \mathrm{C_D}\pi\mathrm{R}^2(\mathrm{u_i} - \mathrm{v_i})|\mathrm{u_i} - \mathrm{v_i}| + \mathrm{C_A} \tag{E.2}$$

The virtual mass force is generated by the acceleration of the fluid around a particle (Zhu, et al. 2015):

$$\mathrm{F_{virtual\ mass}} = \mathrm{C_A}\left(\frac{4}{3}\pi\mathrm{R}^3\rho\right)\frac{\mathrm{d(u_i - v_i)}}{\mathrm{dt}} \tag{E.3}$$

The history force emerges from the lagging boundary layer as the particle accelerates through the fluid (Zhu, et al. 2015):

$$F_{history} = C_H R^2 \sqrt{\pi \rho_c \mu_c} \int_{t_0}^{t} \frac{\left(\frac{d(u_i - v_i)}{dt'}\right)}{\sqrt{t - t'}} dt' \tag{E.4}$$

The three coefficients, C_D, C_A, and C_H are correlations used by Odar and Hamilton for according force terms. In fact, OH-64 used Schiller-Neumann correlation (Karimi, et al. 2012) for the laminar flow (valid in the range of $Re < 1000$), for the drag coefficient (i.e. C_D):

$$C_D = \frac{24}{Re}\left[1 + 0.15Re^{0.687}\right] \tag{E.5}$$

However, both virtual mass and history term force coefficients (C_A and C_H correspondingly) were empirically derived from the OH-64 experimental data (Michaelides and Roig 2011):

$$C_A = 1.05 - \frac{0.066}{Ac^2+0.12} \tag{E.6}$$

$$C_H = 2.88 + \frac{3.12}{(Ac+1)^3} \tag{E.7}$$

where Ac (*acceleration number*) was chosen by OH-64 as the primary variable for correlations:

$$Ac = \frac{(u_i - v_i)}{2\mathrm{R}\left|\frac{d(u_i - v_i)}{dt}\right|} \tag{E.8}$$

Consequently, the accuracy of such semi-empirical coefficients was questioned, and it was assumed that there might be a possible over-prediction from them.

In this research, they are later combined as F_x for simplicity of the analysis:

$$(F_x)_{OH} = (F_{virtual\,mass})_{OH} + (F_{history\,force})_{OH} \tag{E.9}$$

The aim of this study is to further extend the Re number to 300 via numerical simulations using ANSYS Fluent. It is expected that the results of this study will be beneficial to advance the fundamental understanding of oscillating flow over spheres and the potential applications.

NUMERICAL APPROACH

1. GEOMETRY AND SETUP

ANSYS Fluent© was applied to perform the simulation and compare OH-64 model with the CFD results. Since $Re < 300$, a 2D axisymmetric laminar flow model was adopted in order to significantly reduce the computational cost. The computational domain is shown as follows.

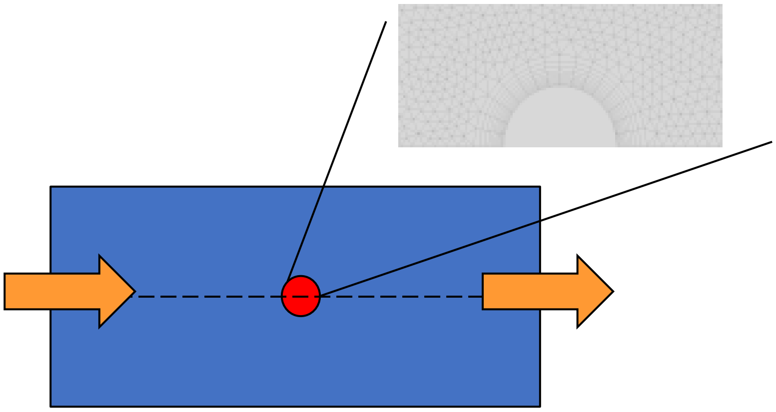

Figure 64: Mesh in the domain and near the sphere surface

The half sphere was modelled as stationary (thus $v_i = 0$) and the fluid (water) was moving around it in oscillating manner. The gravity and energy models were not activated. Different cases with Re varying from 1 to 300 and frequency varying from 0.1 to 100 Hz were simulated. The bottom boundary in the computational domain was set as axis of symmetry. The left, top and right boundaries of the computational domain were set as velocity-inlets with the flow direction normal to the corresponding boundary. The flow velocity was controlled by UDF (User Defined Function) code and mathematically was represented as:

$$u_i = U * sin(f * t) \tag{E.10}$$

where U represents magnitude of the velocity and f represents the frequency.

Table 18: Fluid and particle parameters

Parameters	
Water density (kg/m3)	998.2
Dynamic viscosity, µ (kg/m-s)	0.001003
Diameter (m)	0.001

Finally, the computed force acting on the sphere during 20 seconds of simulation for each case was compared to the theoretical results predicted by OH-64.

To achieve correct mesh parameters for the ANSYS Fluent© model, the results for simulation case with $Re = 75,\ f = 1\,Hz$ was compared to the OH-64 for the same flow conditions.

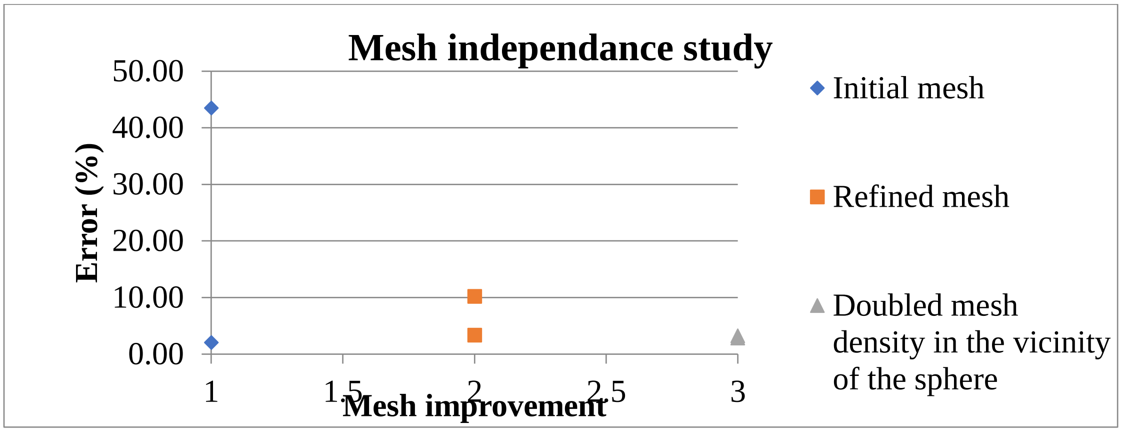

Figure 65: Mesh independence study

The percentage difference (as an absolute error) between OH-64 top peaks and CFD top peaks on the total force acting on the sphere plot (e.g. Figure 66), and similarly the error for their bottom peaks, then was estimated (thus there are two data points for each mesh configuration in Figure 65).

The mesh was refined and then doubled in the sphere's vicinity to achieve same level absolute error for top and bottom peaks (i.e. oscillating flow should produce symmetric error on the top and bottom peaks, as the peak simply indicates current direction of the flow) and also to lower numerical error.

The size of the domain was chosen such as the distance between sphere and any of the domain boundaries is ten times the diameter of the sphere to neglect potential effects from the boundaries on the sphere. Final domain and mesh parameter are provided in the Table 19:

Table 19: Final domain and mesh parameters

Element	Elements	X-lim (m)	Y-lim (m)	Sphere diameter (m)
triangles	12130	0.02	0.02	0.001

2. GOVERNING EQUATIONS

A two-dimensional, incompressible, laminar flow model was used in ANSYS Fluent©. The investigated model certainly has $Kn >> 0.1$ (as it is not microfluidics problem) which is a limit for continuum hypothesis validity and thus Navier-Stokes (N-S) applicability (Pelesko and Bernstein 2003).

Therefore, the governing equations for the CFD simulations are N-S for a 2D case (without energy equation) (Cuan and Chen 2017).

Continuity equation:

$$\frac{\partial \rho}{\partial t} + \frac{\partial(\rho u_i)}{\partial t} = S_m \tag{E.11}$$

where $S_m = 0$ (no any adding mass source terms)

Momentum equation:

$$\rho \frac{\partial u_i}{\partial t} + \frac{\partial(\rho u_i u_j)}{\partial x_i} = -\frac{\partial(\rho)}{\partial x_j} + \frac{\partial}{\partial x_i}\left[\mu\left(\frac{\partial u_j}{\partial x_i} + \frac{\partial u_i}{\partial x_j}\right)\right] + \Phi \tag{E.12}$$

where $\Phi = 0$ (no any model-dependant source terms)

RESULTS DISCUSSION

1. CASES

Ten different cases (Table 20) were simulated in ANSYS Fluent© and compared against OH-64 prediction. The idea behind comparison was to observe the effect of frequency and Re variation on accuracy between results obtained from CFD simulations and OH-64 equations.

Table 20: Case table

Case #	Re	Frequency (Hz)
1	1	0.1
2	1	1
3	1	5
4	1	10
5	1	20
6	1	100
7	75	1
8	100	1
9	200	1
10	300	1

2. FREQUENCY VARIATION

The first six cases were simulated varying the frequency. Consequently, for each case, the total force acting on the sphere (Figure 66 and Figure 68) and F_x (Figure 67and Figure 69) were analysed. The plots contain ANSYS Fluent© results (blue curve) and OH-64 results (red curve).

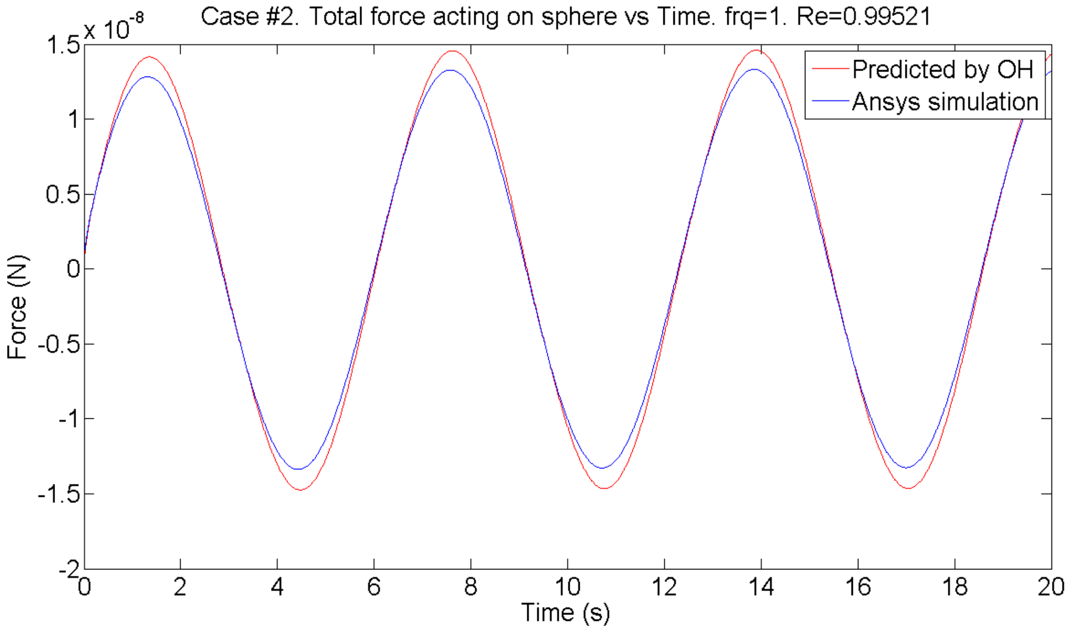

Figure 66: Case 2 (Total force). $Re = 1. f = 1\ Hz$

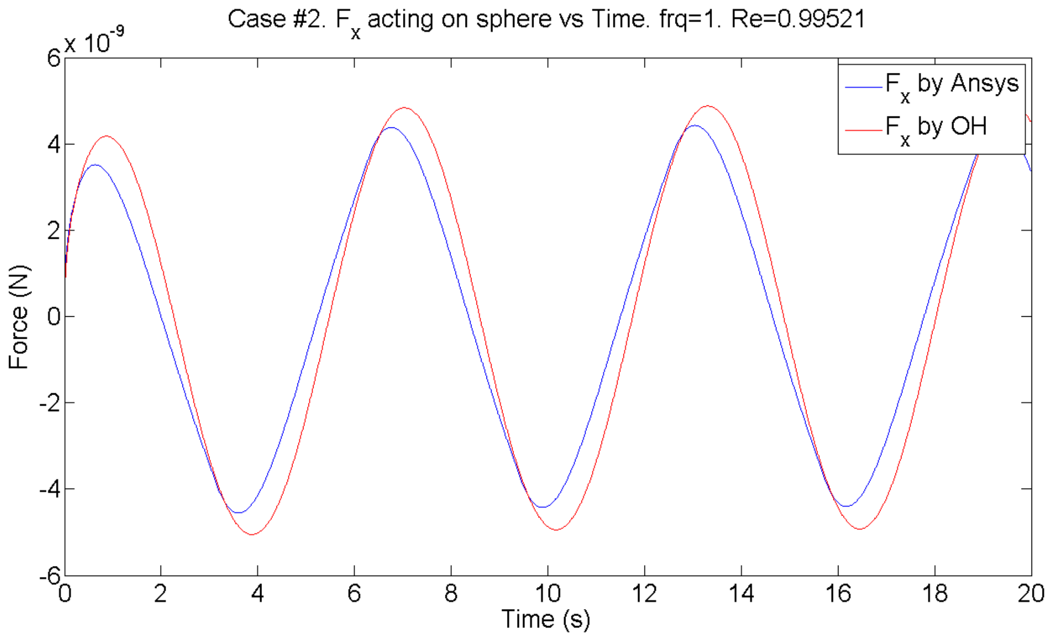

Figure 67: Case 2 (F_x). $Re = 1. f = 1\ Hz$

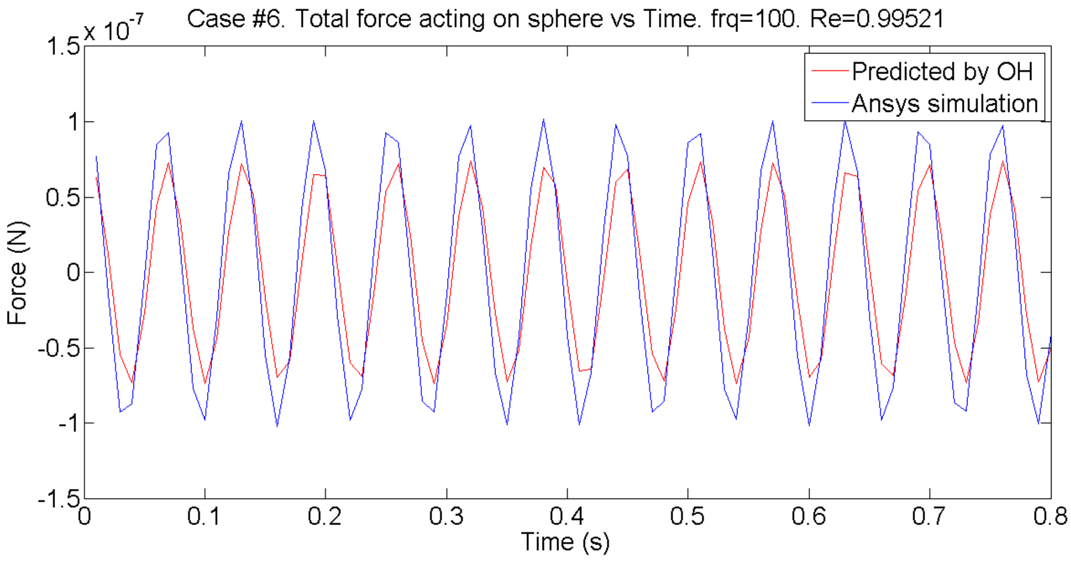

Figure 68: Case 6 (Total force). $Re = 1. f = 100\ Hz$

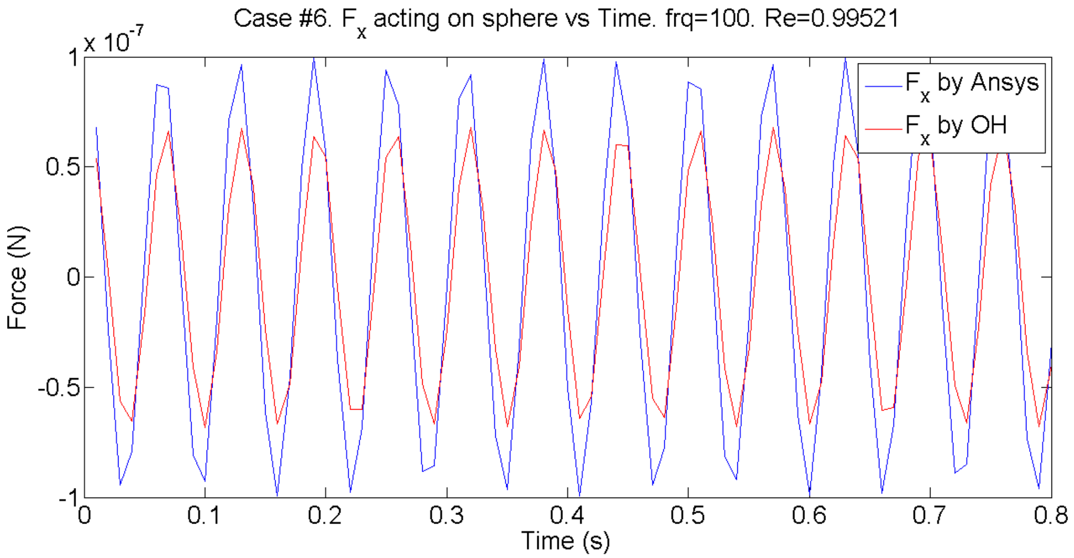

Figure 69: Case 6 (F_x). $Re = 1. f = 100\ Hz$

Two main observations were made in this part of the simulations. First of all, as it is seen from the plots, OH-64 overcompensate CFD results with a tendency of decreasing overcompensation (i.e. red curve has larger range in Figure 66 and Figure 67 that represent Case 2) and even going into undercompensating (i.e. the blue curve has larger range than the red curve in Figure 68 and Figure 69 that represent Case 6) as the frequency increases(from 1 to 100 Hz). Secondly, ANSYS Fluent© results show the same smooth sinusoidal pattern as OH-64.

3. REYNOLDS NUMBER VARIATION

The last four cases (Figure 70 - Figure 77) were simulated varying the Reynolds number. Although, original OH-64 has not been experimentally tested for flows above $Re = 62$, for such simplified CFD model it was observed that OH-64 results closely approach the total force acting on the sphere given by ANSYS Fluent©.

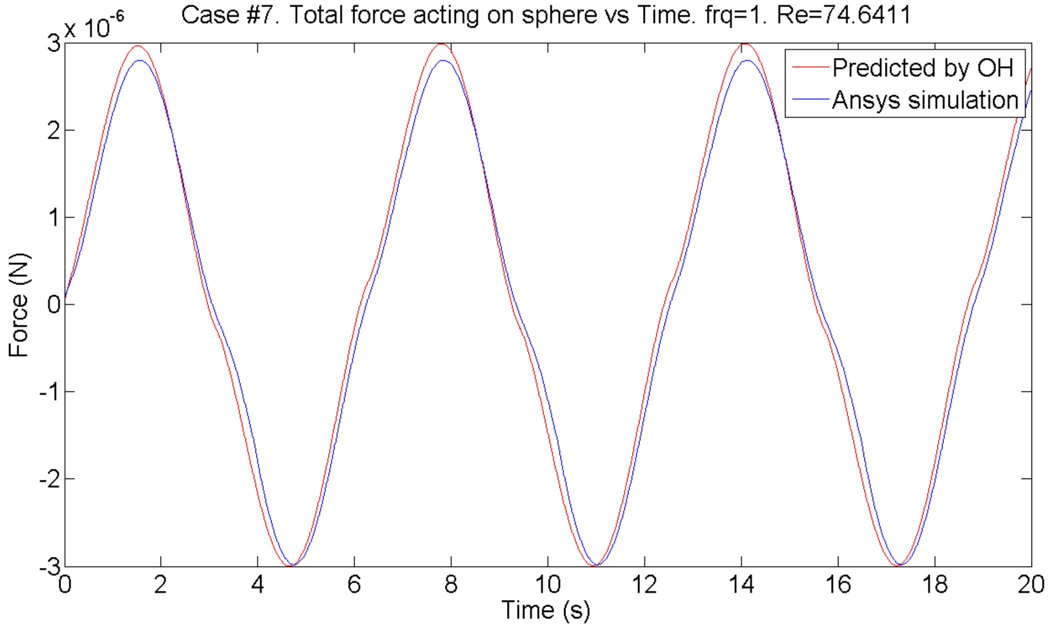

Figure 70: Case 7 (Total force). $Re = 75. f = 1\ Hz$

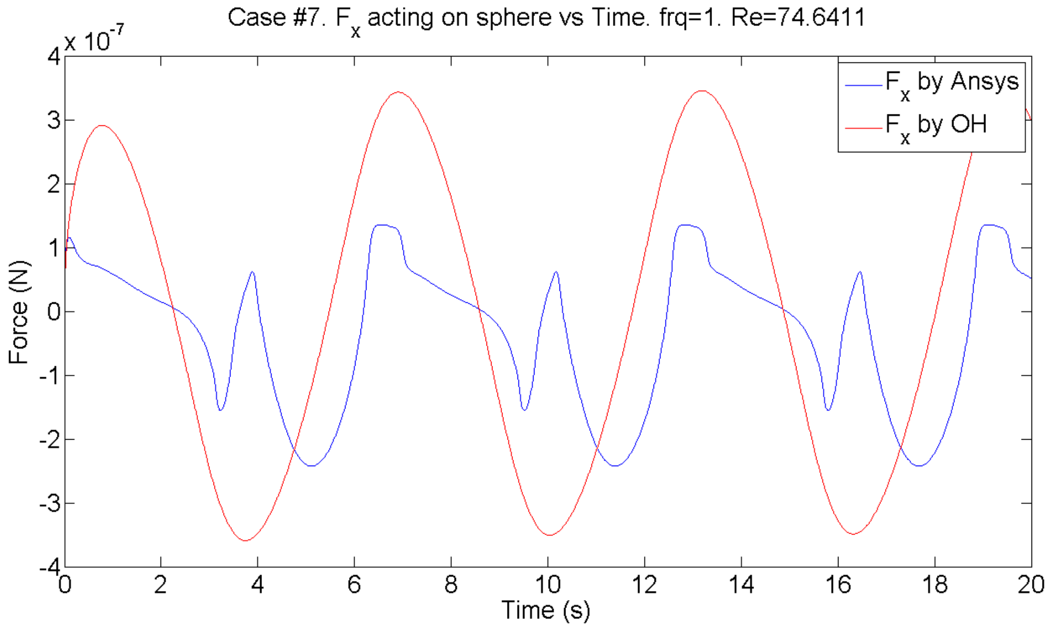

Figure 71: Case 7 (Fx). $Re = 75. f = 1\ Hz$

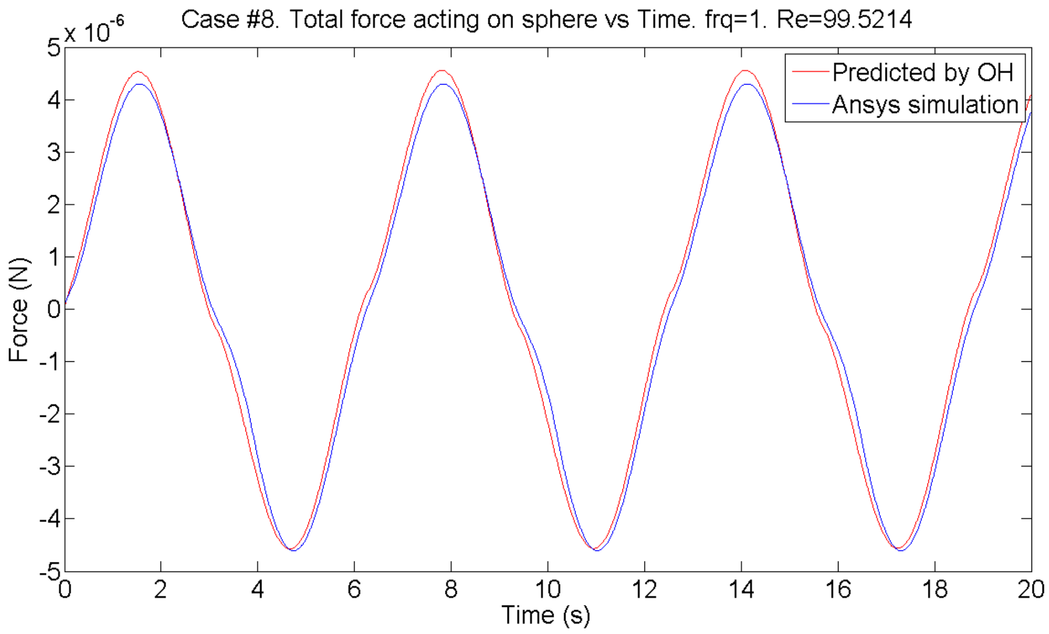

Figure 72: Case 8 (Total force). $Re = 100. f = 1\ Hz$

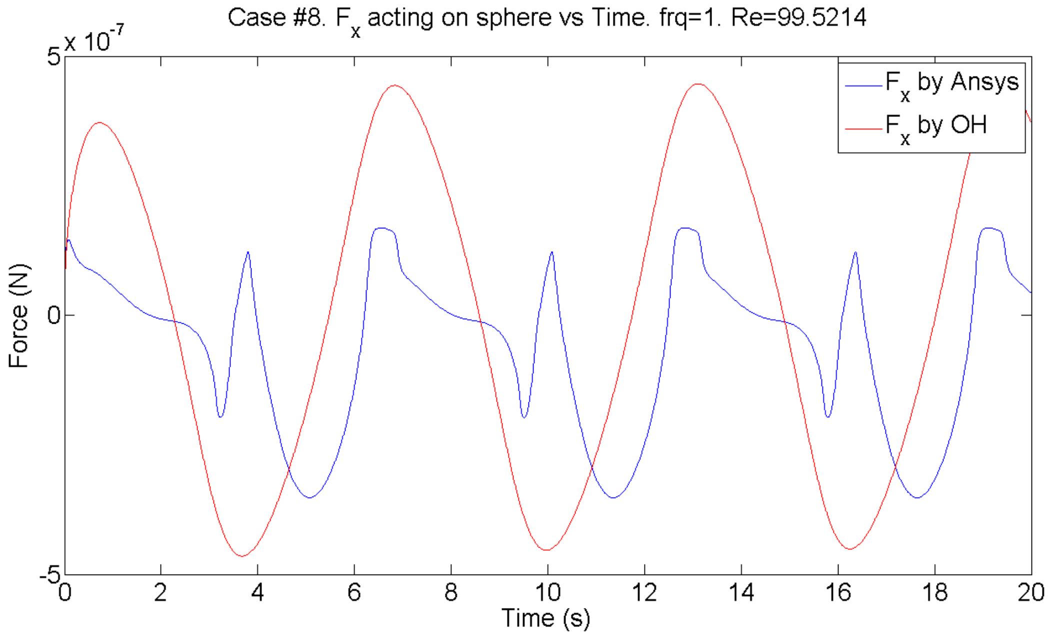

Figure 73: Case 8 (Fx). $Re = 100. f = 1\ Hz$

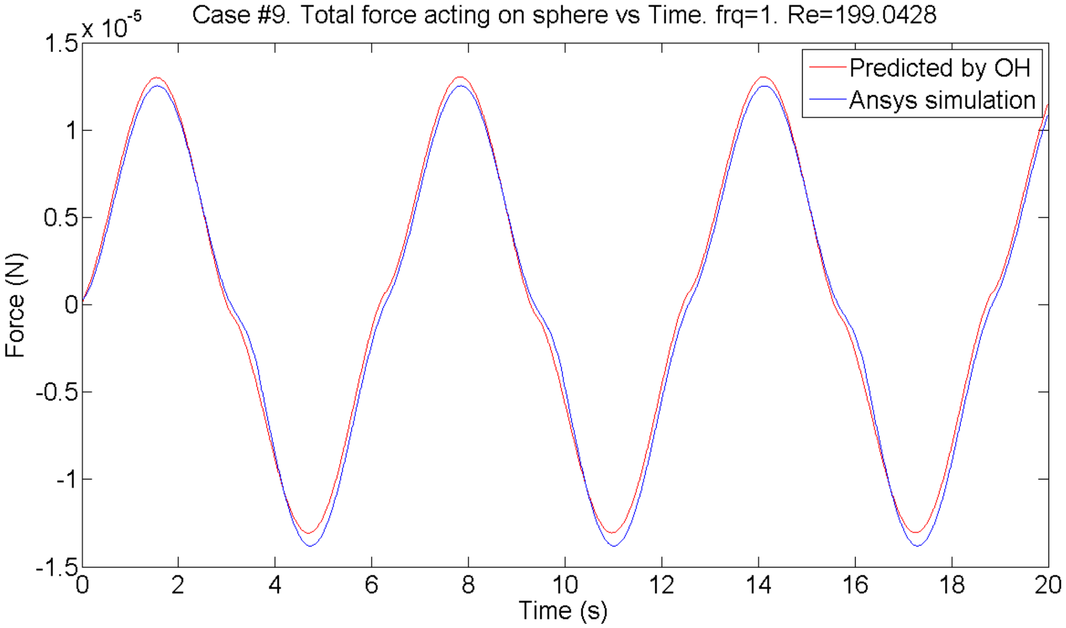

Figure 74: Case 9 (Total force). $Re = 200. f = 1\ Hz$

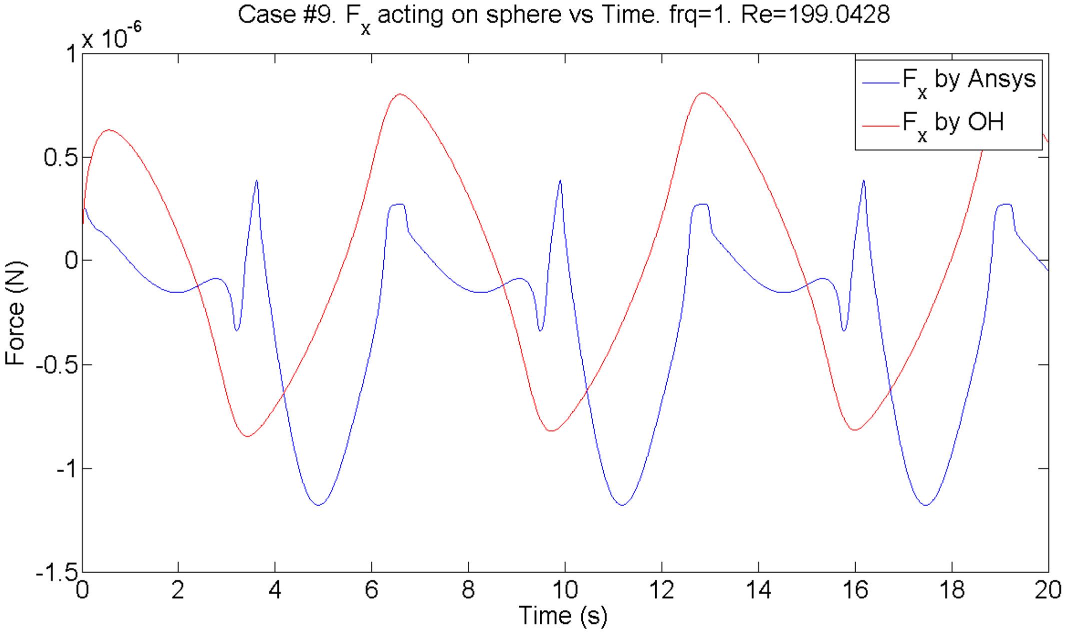

Figure 75: Case 9 (Fx). $Re = 200. f = 1\ Hz$

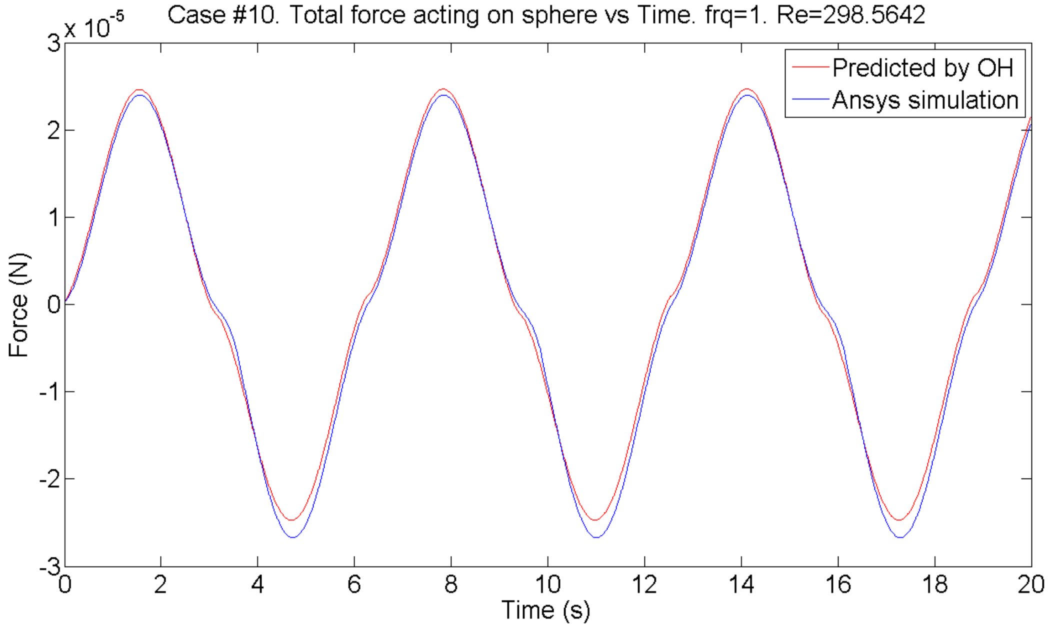

Figure 76: Case 10 (Total force). $Re = 300. f = 1\ Hz$

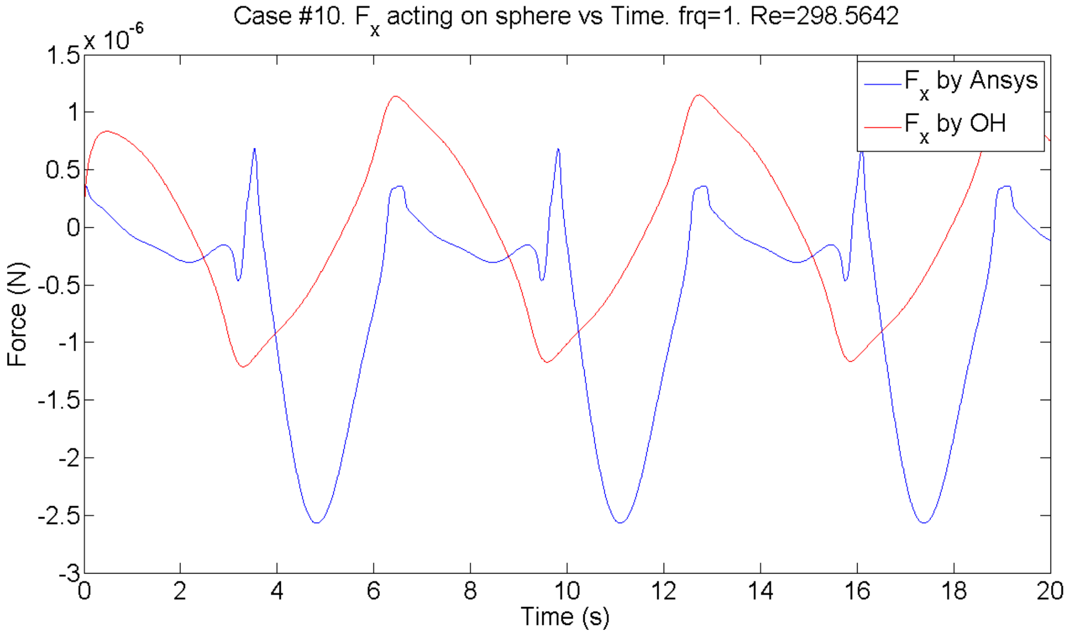

Figure 77: Case 10 (F_x). $Re = 300. f = 1\ Hz$

The main observation discerned from these simulations was disturbance (unexpected kinks on the curve) in the F_x curve. Therefore, as OH-64 does not predict any of such disturbance (red curves have a smooth sinusoidal shape on the plots), there must be a source of such phenomena that is not accomodated in the OH-64 model. Also, in the same manner as for the varying of the frequency, varying of the Re leads to transition from overcompensating the results (most noticeably viewed on the F_x plot) to undercompensating the results as Re increases.

4. DETAILED ANALYSIS OF THE FLOW

In order to find the physical source of the disturbance when varying Re, detailed flow analysis was performed. Case 9 was chosen for such analysis.

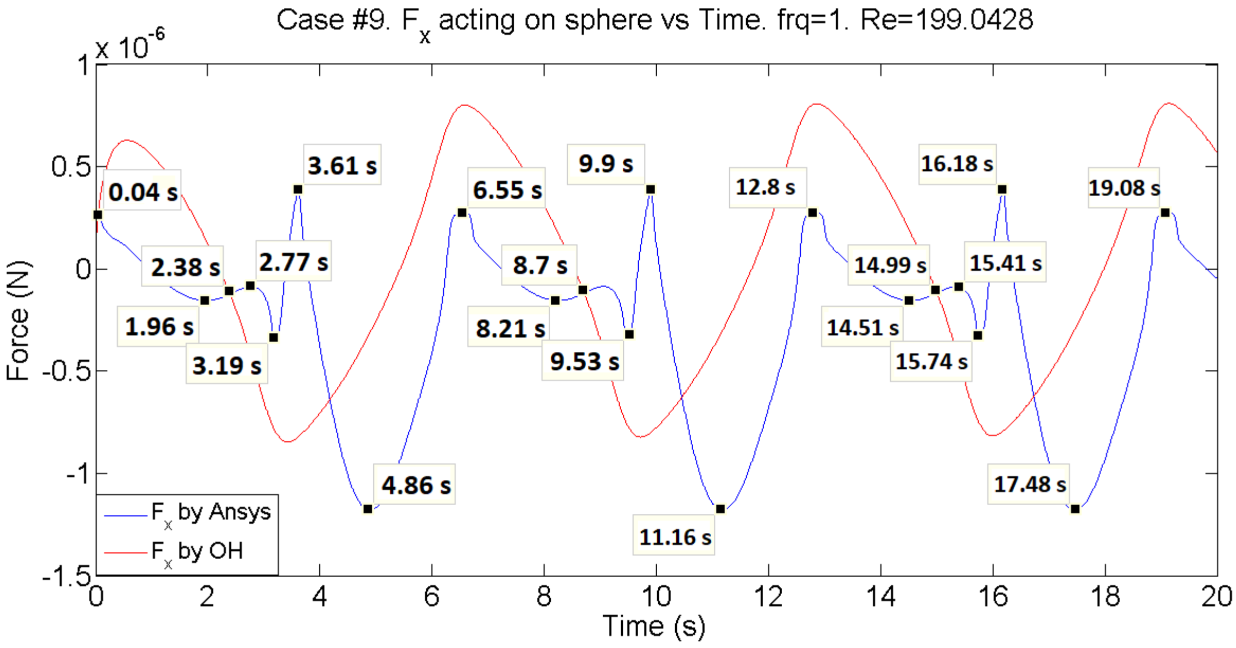

Figure 78: Case 9 (Re = 200, f = 1 Hz). F_x acting on the sphere vs Time

The possible time points at which detection of the disturbance's source is most likely were marked on Figure 78 and analyzed by ANSYS© post-processing tools. The velocity vectors were inspected at these time points and angle of separation was recorded for each of the time point (e.g. Figure 79 where red line indicates a disturbance in the velocity vectors and hence a separation angle on the surface of the sphere). As the curve (Figure 78) has a repeatable pattern, the separation angle variation also has a repeatable pattern (Figure 80)

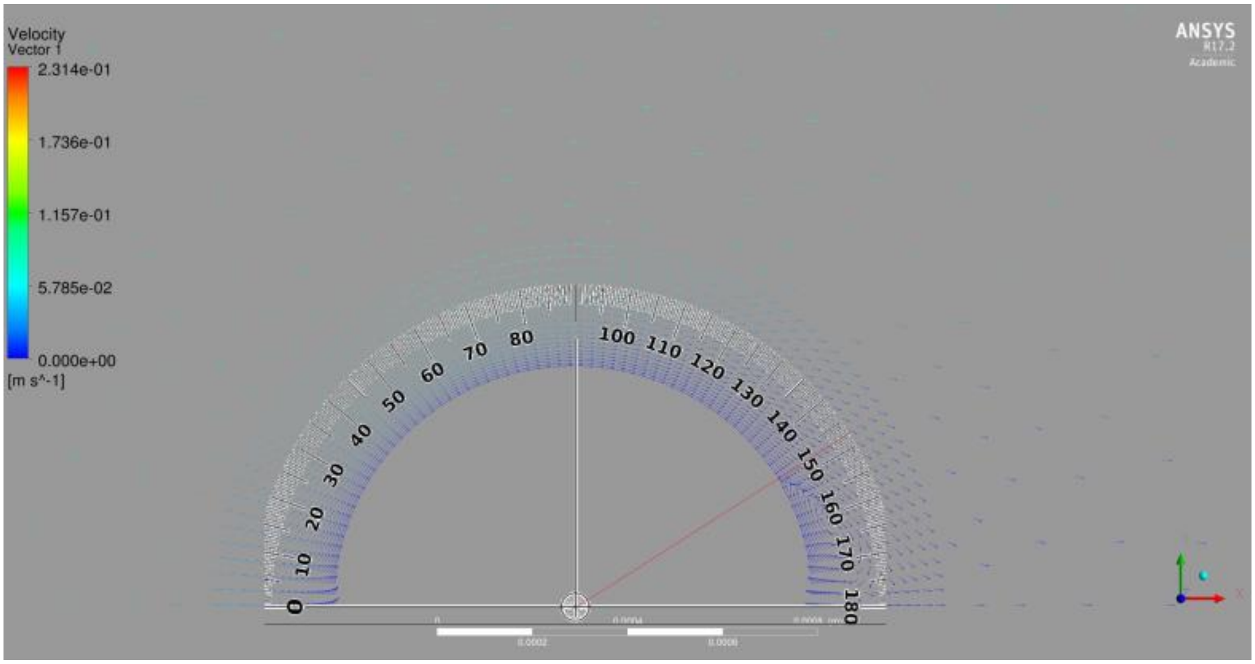

Figure 79: Case 9 (Re = 200, f = 1 Hz). Velocity vectors - flow analysis (at $t = 6.55$ *s)*

The flow pictures analysis (as in Figure 79) for all of the time points leads to a conclusion that the flow separates from the sphere at certain time points (Table 21 and Figure 80). It is a reasonable assumption as in general flow separation is immanent for flows with $Re > 24$ (Southard 2006). Therefore, it is assumed that the disturbance in the F_x curve is due to the pressure variation (and thus variations of the force acting on the sphere) in the wake region in the vicinity of the sphere, formed due to flow separation.

The data for the flow separation angle (the bottom left point on the sphere is referenced as 0 degrees) is presented in the table below:

Table 21: Flow separation angle

Time (s)	Angle (degree)	Comments
0.04		no separation
1.96	119	
2.38	123	
2.77	130.5	
3.19		no separation
3.61	44	
4.86	62.5	
6.55	147	
8.21	119	
8.7	123	
9.53		no separation
9.9	46	
11.16	62	
12.8	159	
14.51	119	
14.99	123	
15.41	132.5	
15.74		no separation
16.18	45	
17.48	62	
19.08	160	

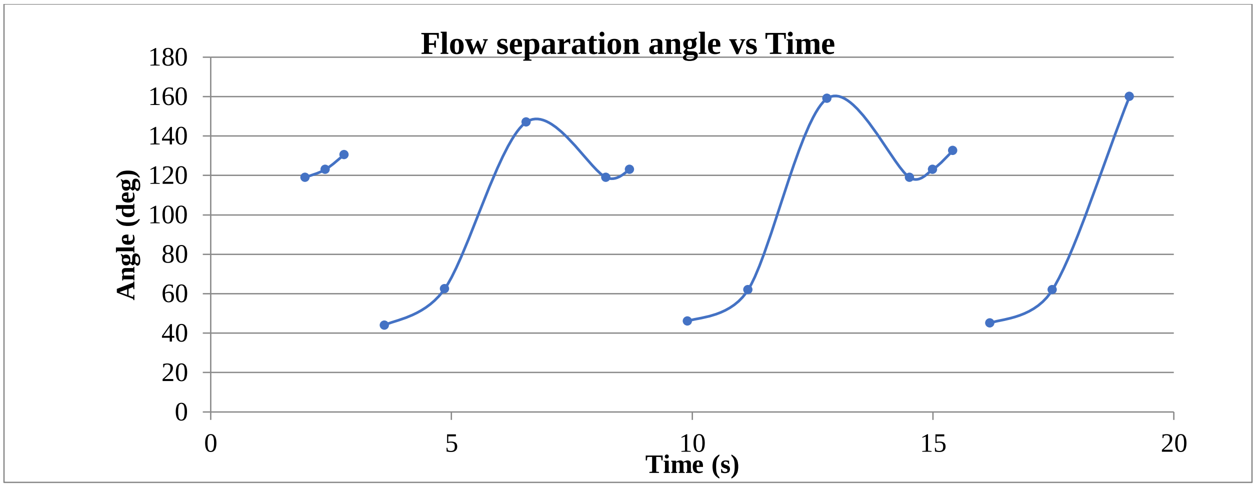

Figure 80: Flow separation angle vs Time

So, the separation angle is a repeating sinusoidal pattern as the force which is governed by sinusoidal velocity input. The separation angle is directly related to the velocity, as the velocity increases, the force acting on the sphere increases correspondingly and thus the separation nucleus moves from the rear part of the sphere towards its equator. Then, as the flow changes direction (due to the oscillating nature of the flow), the pattern repeats again but from the opposite side of the sphere.

5. HYSTERESIS

The detailed analysis of the flow resulted in a conclusion that the disturbance in the F_x curve between OH-64 and ANSYS Fluent© results for moderate Re flows ($Re < 300$) is due to flow separation and wake region formation. Therefore, quantification of the wake influence on the sphere is important to derive a correction for the OH-64 model for such range of Re. One way to quantify it was an idea to use a concept of hysteresis.

In oscillatory systems, the vibrations associated with the system are accompanied by hysterical losses (e.g. energy dissipation in elastic systems during cyclic loading/unloading) (Izmailov, Karagioz and Shakhparonov 2015). In this oscillating flow investigation, the energy dissipation in the wake region due to formation of the vortices in the vicinity of the sphere and with direct impact on the forces acting on the sphere can be observed from the hysteresis perspectives.

The plots of F_x versus input velocity for comparing results obtained by ANSYS Fluent © (blue curve), by OH-64 (red curve) and the F_x difference between them (green curve) are shown below (Figure 81-Figure 86).

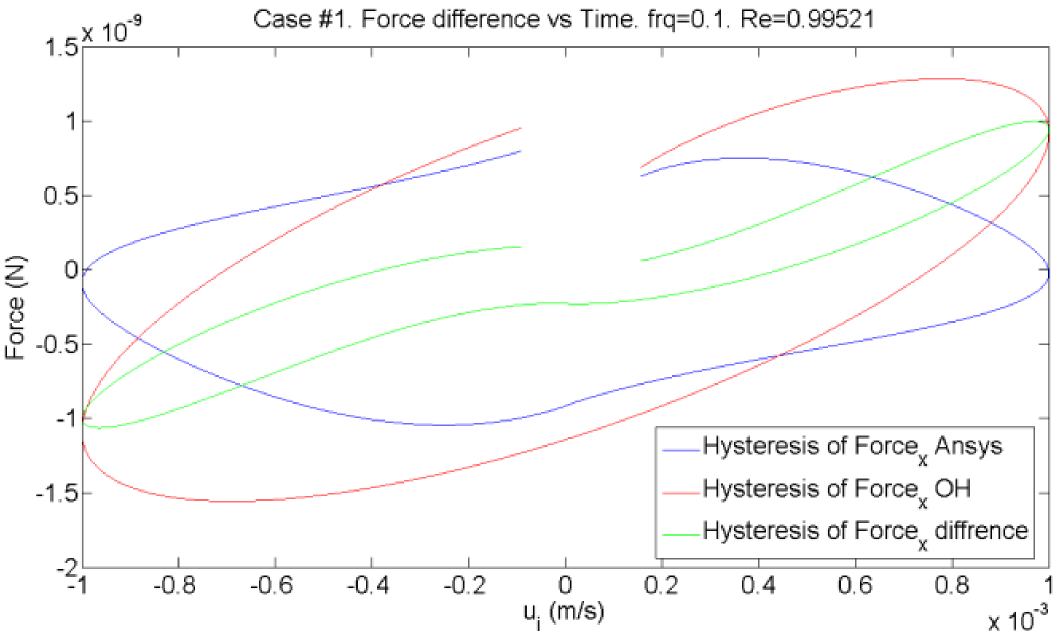

Figure 81: Case 1. $Re = 1. f = 0.1\ Hz$

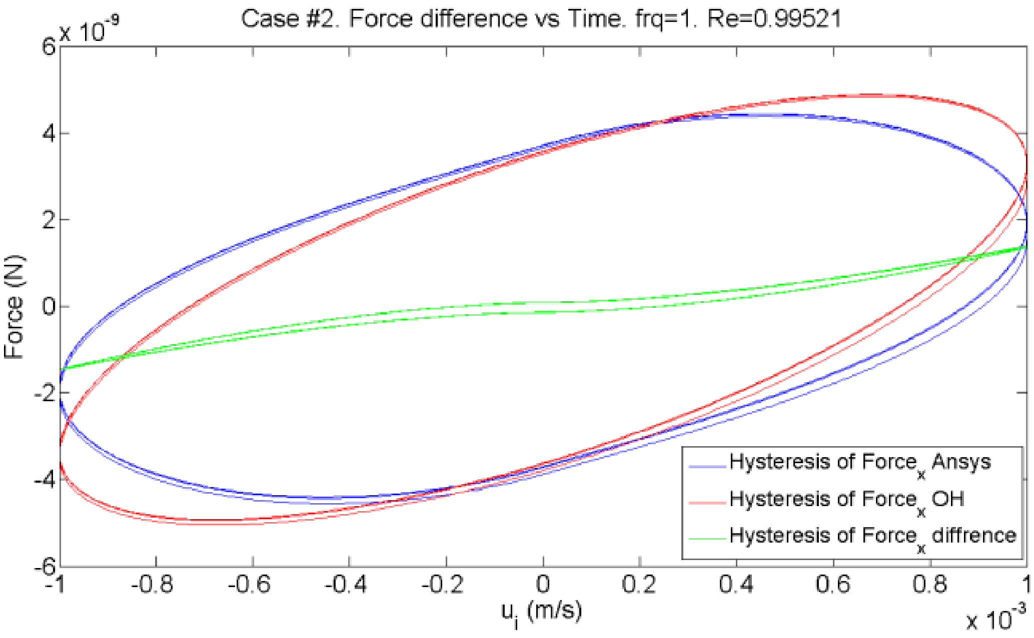

Figure 82: Case 2. $Re = 1. f = 1\ Hz$

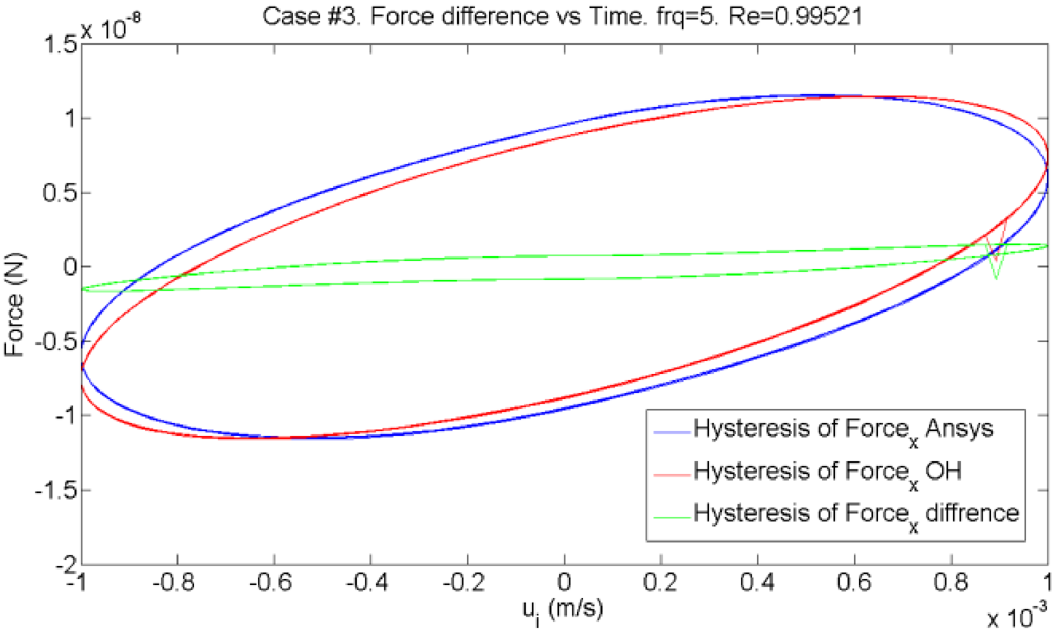

Figure 83: Case 1. $Re = 1. f = 5\ Hz$

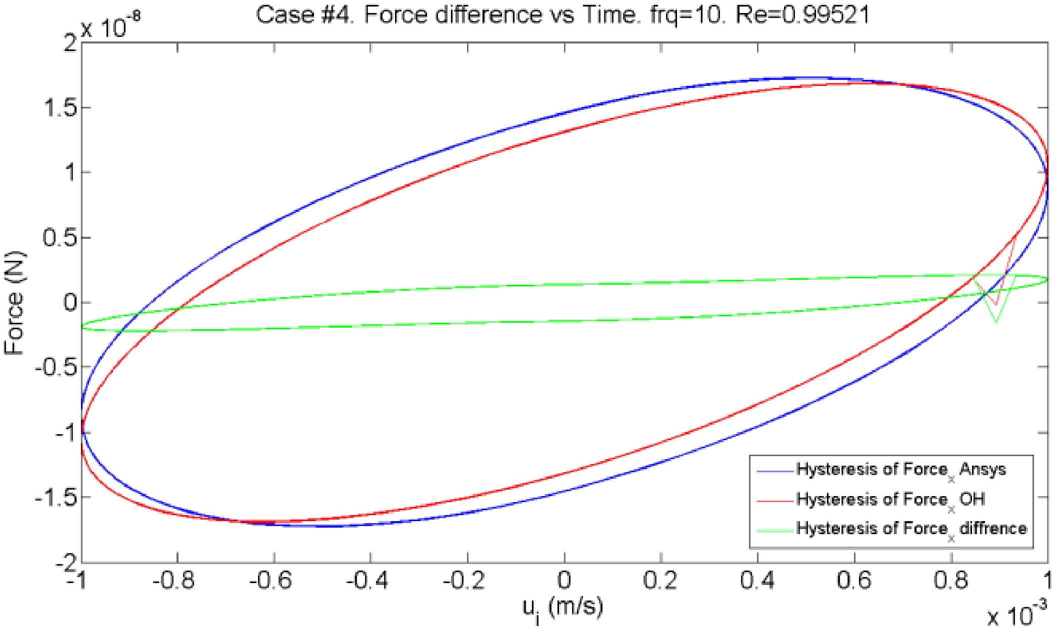

Figure 84: Case 4. $Re = 1. f = 10\ Hz$

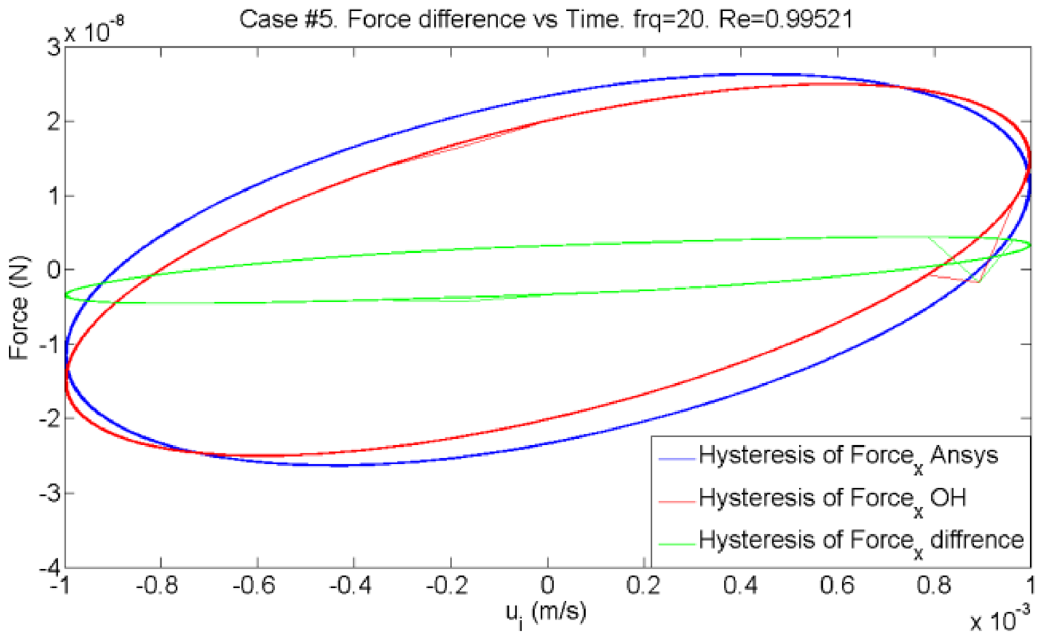

Figure 85: Case 1. $Re = 1. f = 20\ Hz$

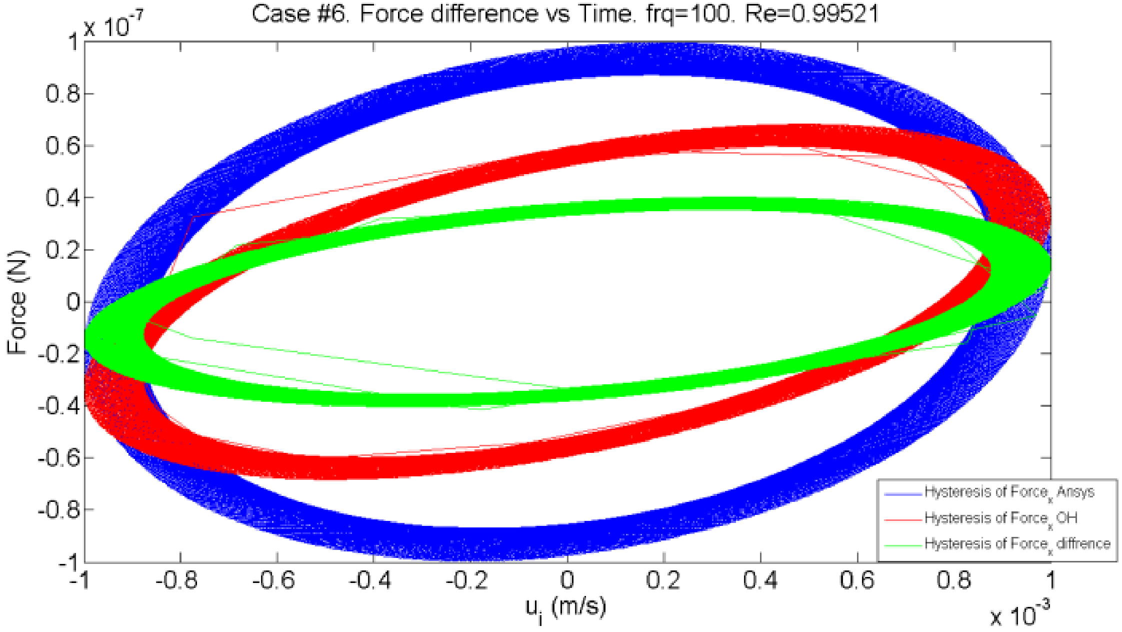

Figure 86: Case 1. $Re = 1. f = 100\ Hz$

As the flow is oscillatory in nature, it creates a round shaped cycle. The right side of the plot if for positive velocity flow (thus the flow moves from left to right) and the left side is for negative velocity flow (thus the flow moves from right to left). The area under the curve is representing power as:

$$Power = Force * Velocity \tag{E.13}$$

It may be observed that there is a discrepancy between the ANSYS Fluent© results curve and OH-64 curve. However, such discrepancy is relatively not significant and can be assumed as resulting from over- or undercompensating by the OH-64 model.

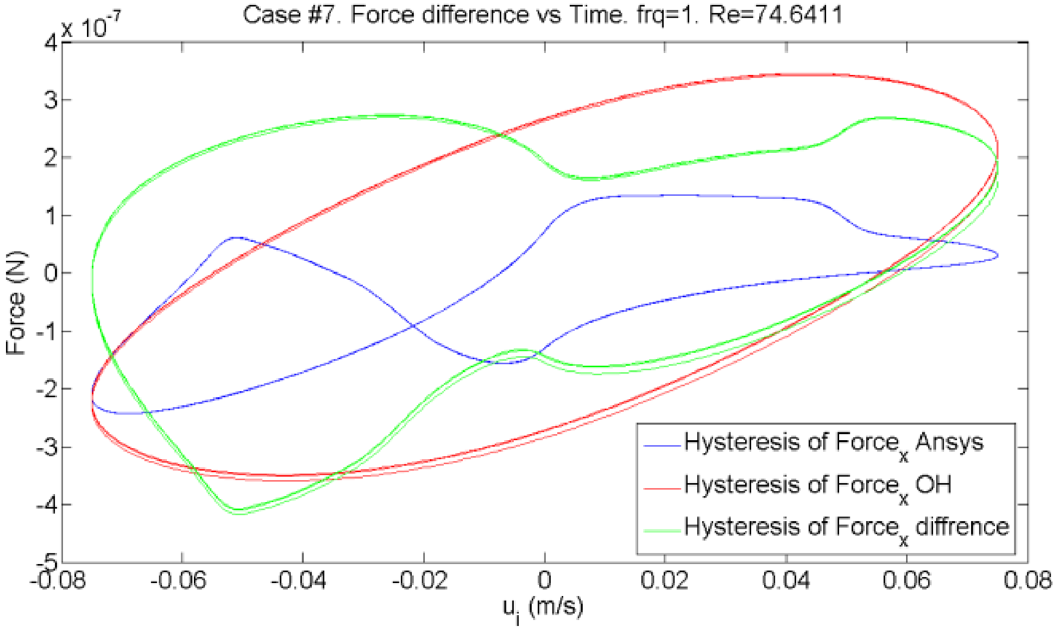

Figure 87: Case 7. $Re = 75. f = 1\ Hz$

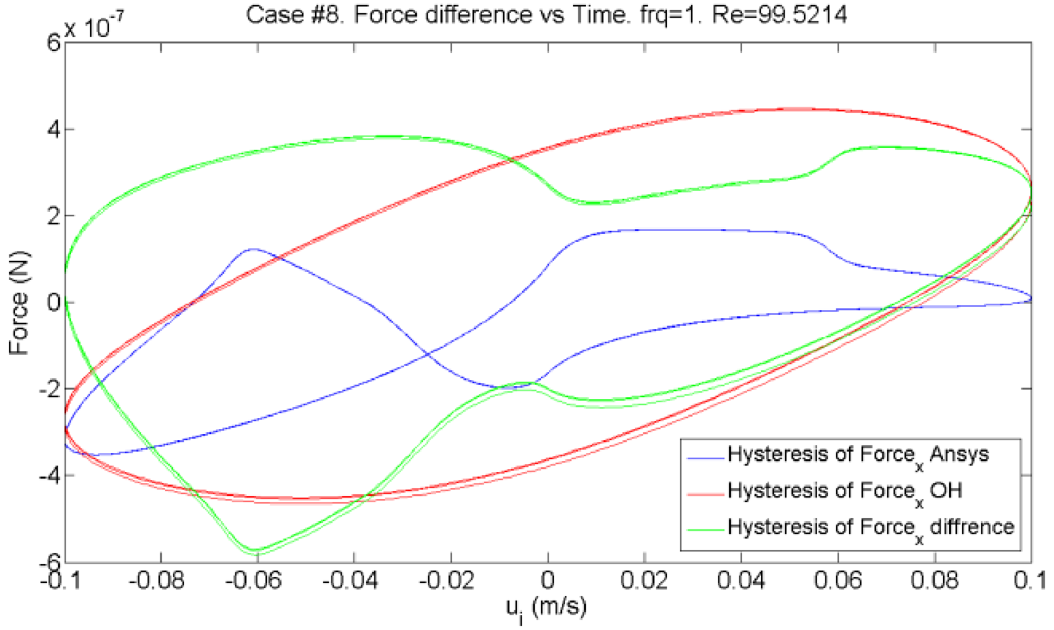

Figure 88: Case 8. $Re = 100.\ f = 1\ Hz$

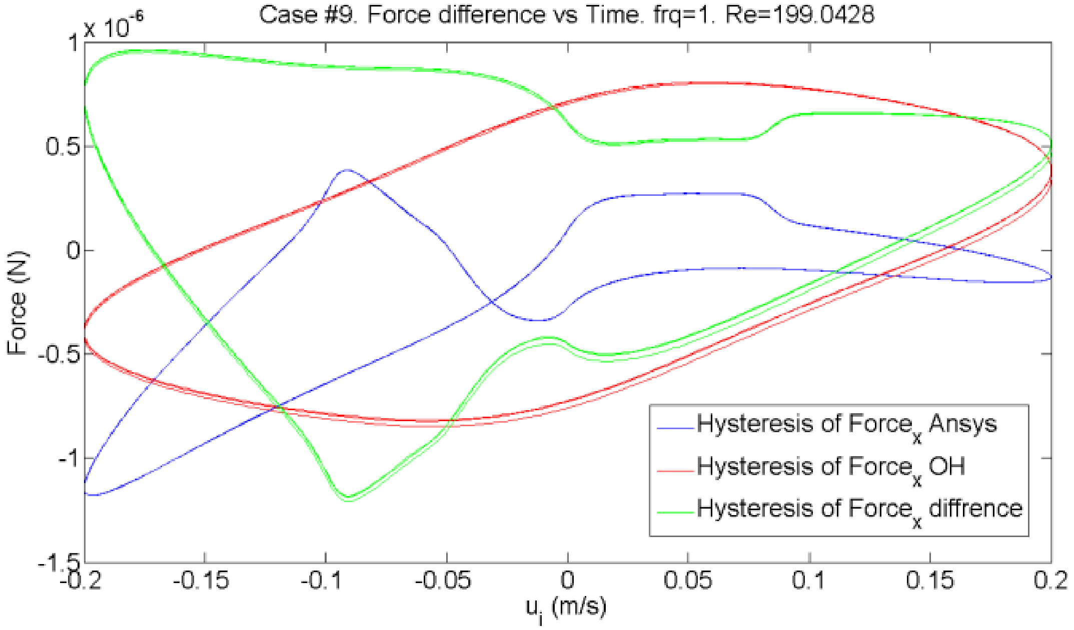

Figure 89: Case 9. $Re = 200.\ f = 1\ Hz$

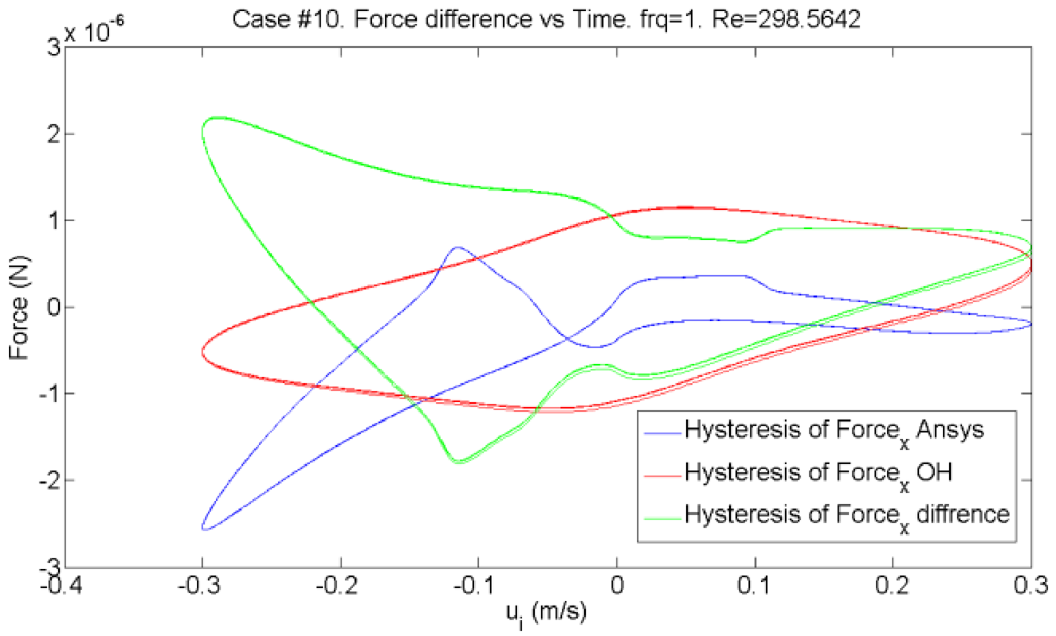

Figure 90: Case 10. $Re = 300. f = 1\ Hz$

The two most distinctive outcomes of the Re variation plots are: the ‘butterfly’ shaped contour of the ANSYS Fluent© results curve (coloured blue on the plots) and the much bigger F_x difference curve (coloured green on the plots) comparing to previous frequency variation plots. In fact, these two outcomes are closely related to each other, as the ‘butterfly’ shape occurred because of the curve twisting on the left side of the plot, at the same time points where unexpected kinks were found in F_x vs Time plots for Cases 7-10 (Figure 71, Figure 73, Figure 75 and Figure 77). The source of such kinks and curve twisting is assumed to be vortices in the wake region as discussed earlier. Therefore, as the F_x difference curve is nothing more than the difference between ANSYS Fluent© and OH-64 results, at such kinks the difference becomes larger (on the hysteresis plots, it is the difference between the red curve and further blue curve for the twisted left side of the green curve, while on the right side of the green curve, it is still the difference between the red curve and the nearest blue curve). Consequently, the left (twisted side) of the green curve is bigger and not enclosed in red or blue curves as the curve for difference is logically expected to be.

CORRECTION TERMS FOR OH-64

One possible approach to derive a new correction for OH-64 is to analyse the areas of the hysteresis plots and based on the difference between area under ANSYS Fluent© curve and OH-64 curve propose a new correction.

Table 22: Hysteresis results

Case	Re	f (Hz)	$(F_x)_{OH}$ area (W)	$(F_x)_{ANSYS}$ area (W)	$(F_x)_{difference}$ area (W)	Subtraction (W)
1		0.1	3.17E-12	2.43E-12	7.45E-13	7.45E-13
2	1	1	3.41E-11	3.50E-11	8.94E-13	-8.94E-13
3	1	5	4.07E-10	4.43E-10	3.55E-11	-3.55E-11
4	1	10	1.20E-09	1.33E-09	1.29E-10	-1.29E-10
5	1	20	3.69E-09	4.30E-09	6.04E-10	-6.04E-10
6	1	100	4.61E-08	7.55E-08	2.94E-08	-2.94E-08
7	75	1	1.86E-07	1.02E-08	1.76E-07	1.76E-07
8	100	1	3.23E-07	3.48E-09	3.20E-07	3.20E-07
9	200	1	1.18E-06	1.15E-07	1.30E-06	1.07E-06
10	300	1	2.47E-06	3.46E-07	2.81E-06	2.12E-06

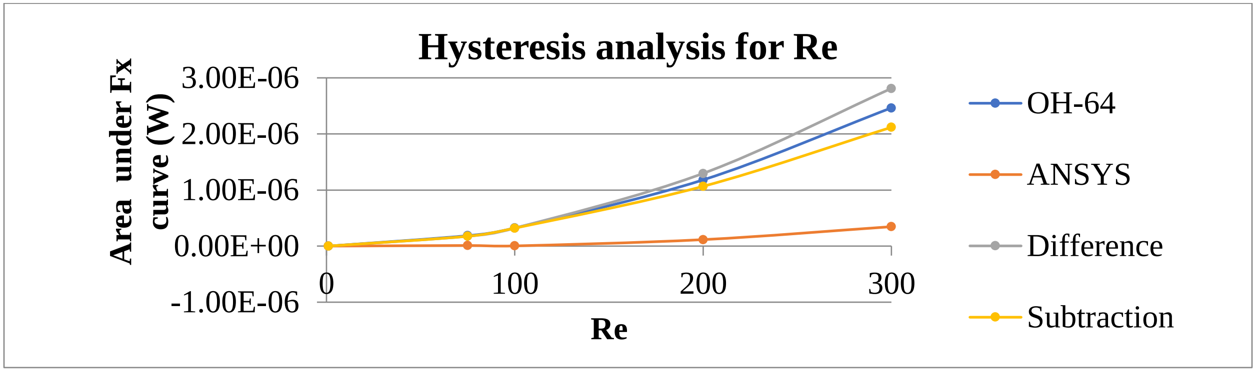

Figure 91: Hysteresis analysis for Re variation

The hysteresis analysis for Re (Table 22: Hysteresis resultsTable 22 and Figure 91) contains a difference curve (coloured as green) and a subtraction curve (coloured as violet). The difference between these curves is in the method used for calculations. The area difference (green curve) was calculated as the area under the F_x difference curve (also green curve on hysteresis plots), while area subtraction (violet curve) was calculated as just a subtraction of ANSYS Fluent© curve area from the OH-64 curve area. For the purpose of finding a good correction, quantification of subtraction (violet curve) looks more promising. Therefore, a power law fit could be applied (Figure 92 and Figure 93).

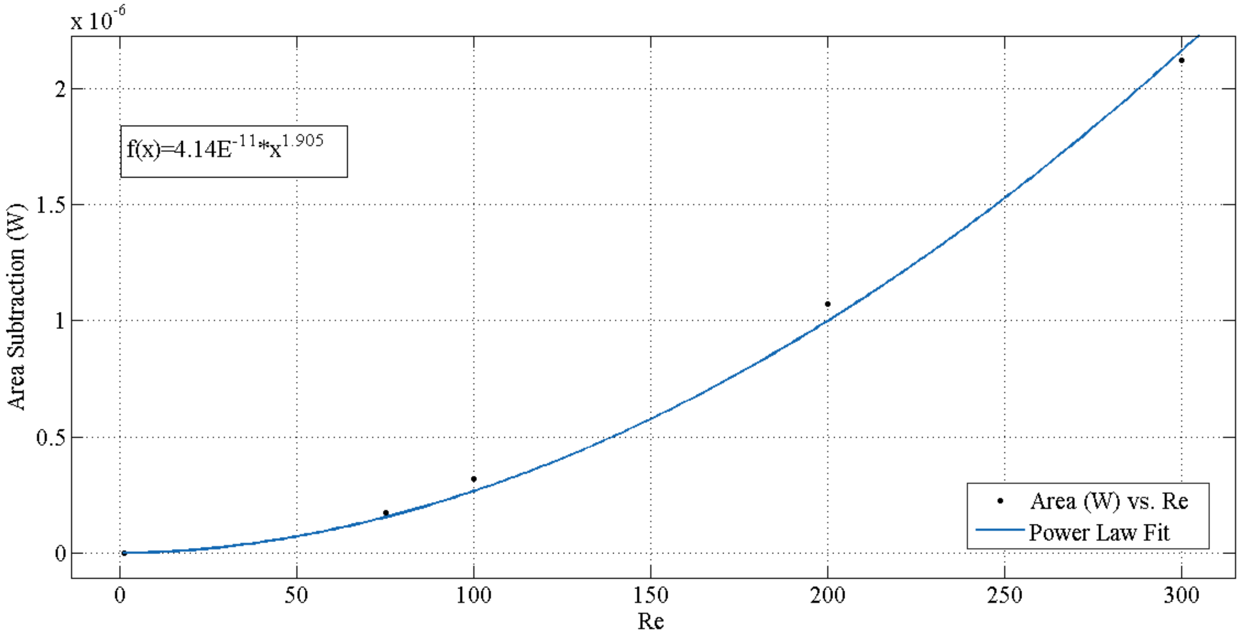

Figure 92: Power Law Fit for Area Subtraction (W) vs Re

The power law fit for Area Subtraction (Figure 92) resulted in an equation:

$$f(x) = 4.14E^{11} * x^{1.905} \tag{E.14}$$

However, another way to quantify the correction is to work directly with F_x plots for cases 7-10 (Figure 71, Figure 73, Figure 75 and Figure 77) and try to find a correction that could match the amplitudes for OH-64 and ANSYS Fluent© results.

Table 23: Average F_x difference for each case

Case	Re	*f* (Hz)	Average F_x difference (N)
1		0.1	-4.59E-11
2	1	1	-8.82E-12
3	1	5	-4.44E-11
4	1	10	-3.56E-11
5	1	20	-1.72E-11
6	1	100	-4.82E-11
7	75	1	4.46E-08
8	100	1	7.46E-08
9	200	1	3.09E-07
10	300	1	6.71E-07

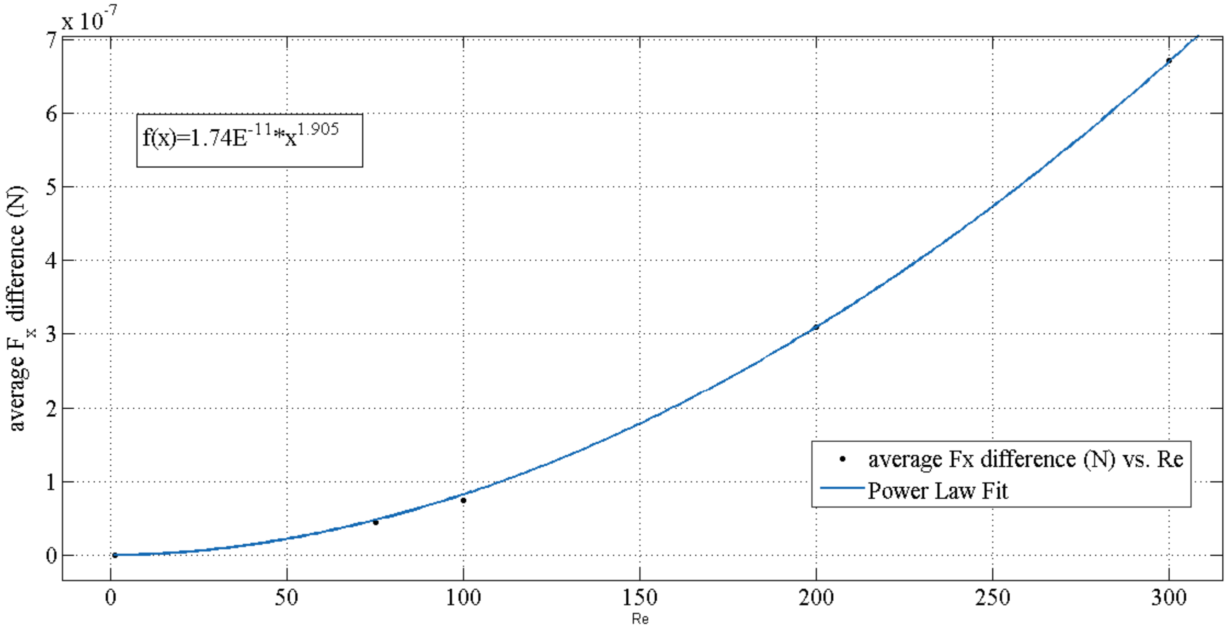

Figure 93: Power Law Fit for average F_x difference (N) vs Re

The power law fit for the average F_x difference (Figure 93) resulted in an equation:

$$f(x) = 1.74E^{11} * x^{1.906} \tag{E.15}$$

Although, the power fit equation for area subtraction (denoted as power with ‘W’ as primary units) does not give directly a correction term for force equation (denoted as force with ‘N’ as primary units). However, an important observation was made when comparing to the power law fit for the average F_x difference equation, both power fit equations have approximately the same exponent (1.905 for the area subtraction and 1.906 for the average F_x difference).

The power fit for the average F_x difference equation can be applied as a correction (modifying) term to the OH-64 F_x equation. The application of such a correction to the OH-64 F_x equation is shown below (Figure 94 - Figure 103).

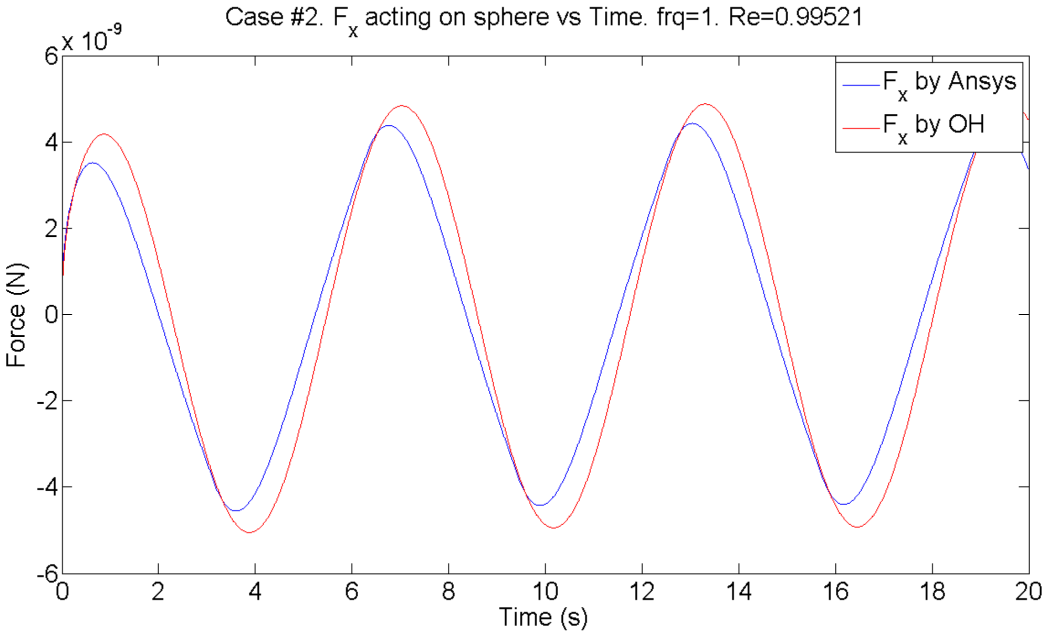

Figure 94: Case 2. $Re = 1. f = 1$ *Hz (original)*

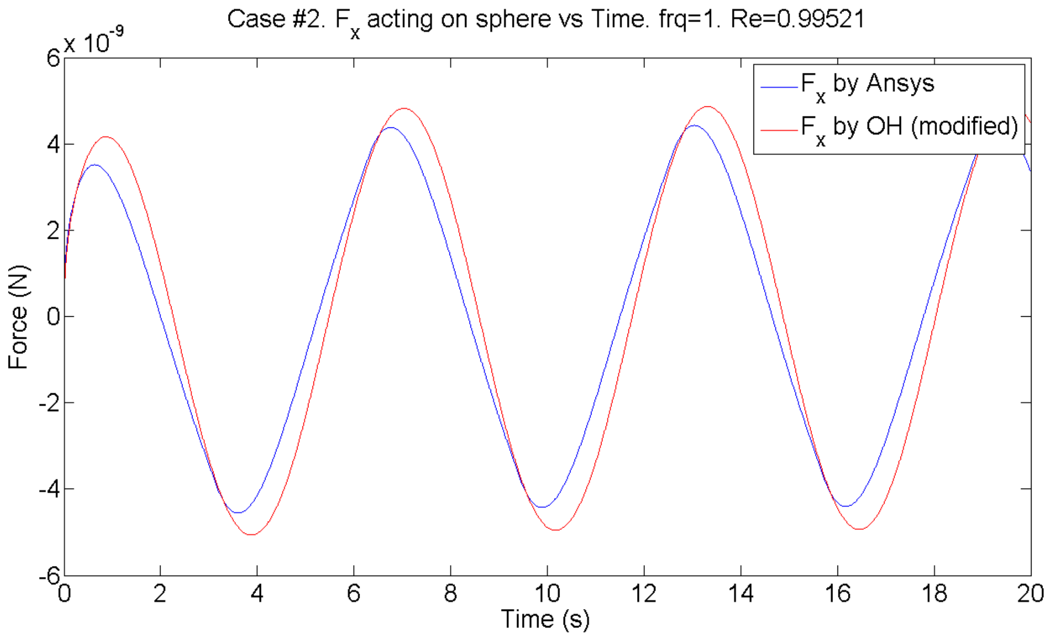

Figure 95: Case 2. $Re = 1. f = 1\ Hz$ *(modified)*

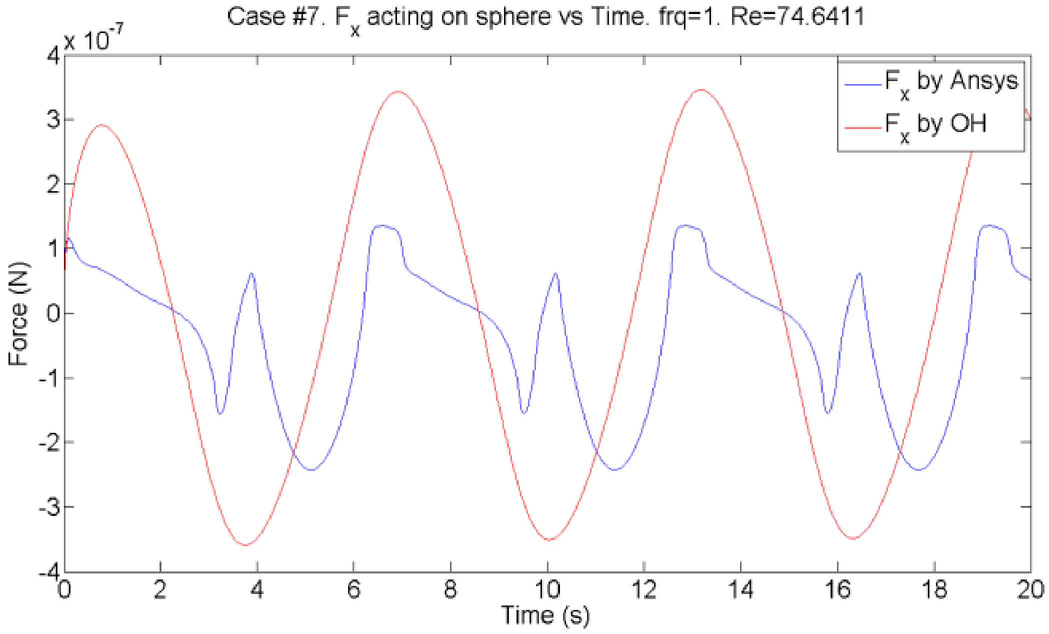

Figure 96: Case 7. $Re = 75. f = 1\ Hz$ *(original)*

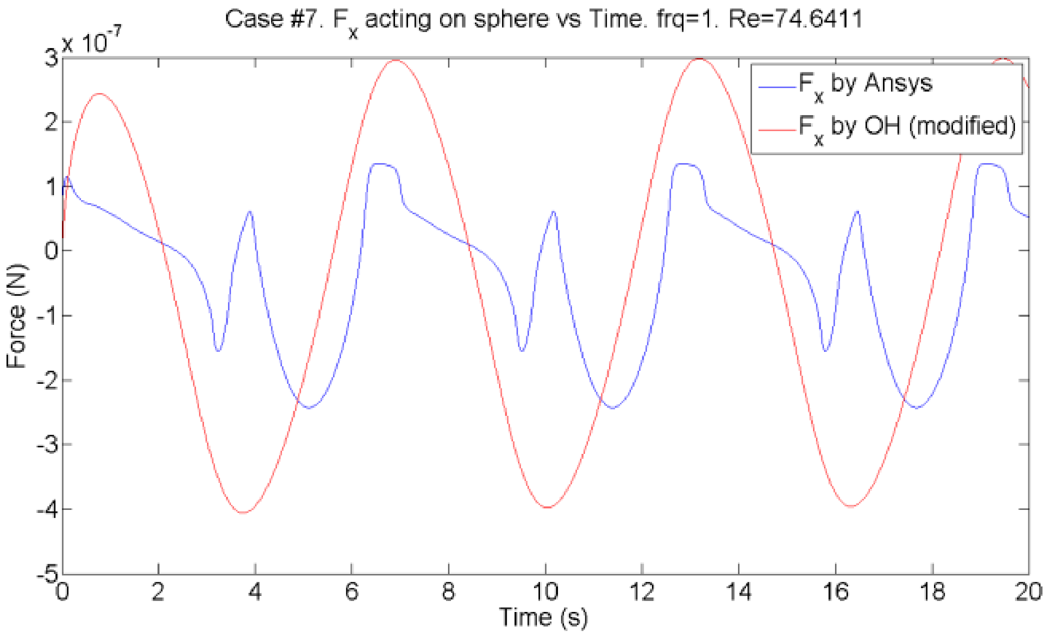

Figure 97: Case 7. $Re = 75. f = 1$ *Hz (modified)*

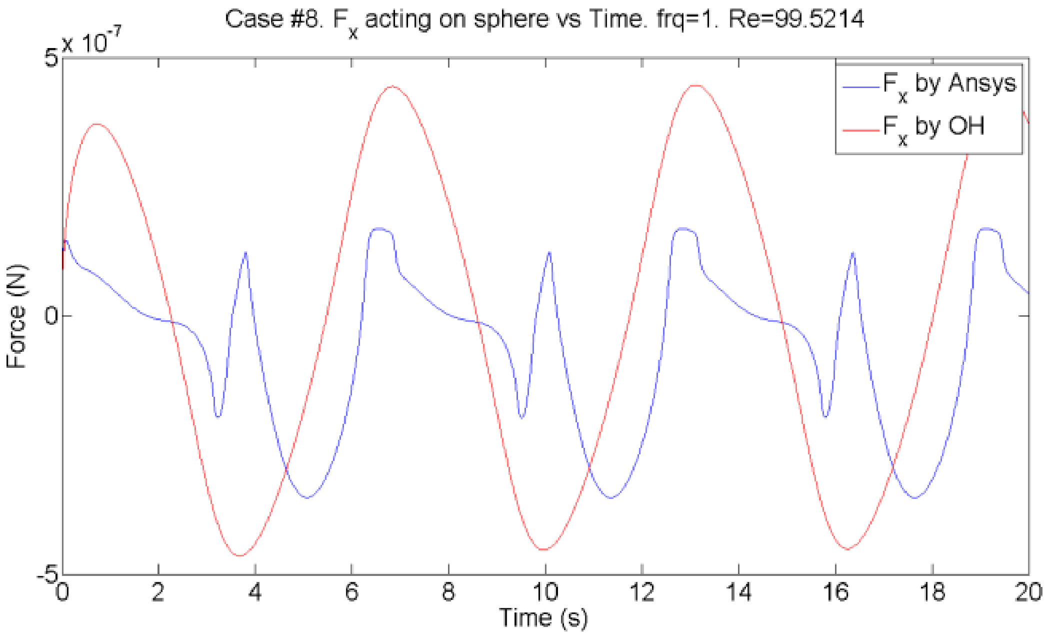

Figure 98: Case 8. $Re = 100. f = 1$ *Hz (original)*

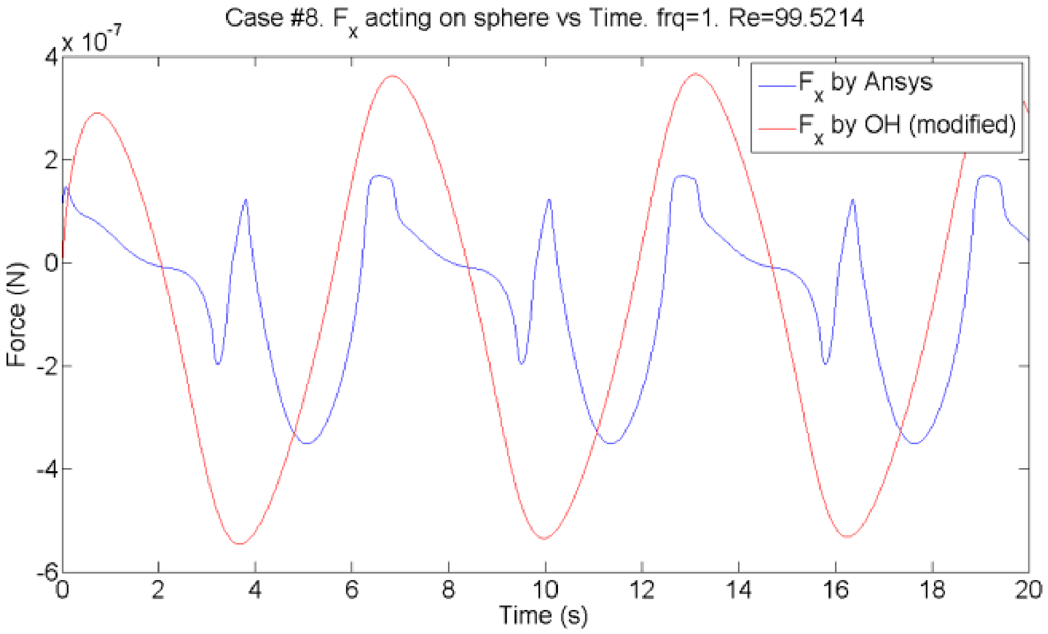

Figure 99: Case 8. $Re = 100. f = 1$ *Hz (modified)*

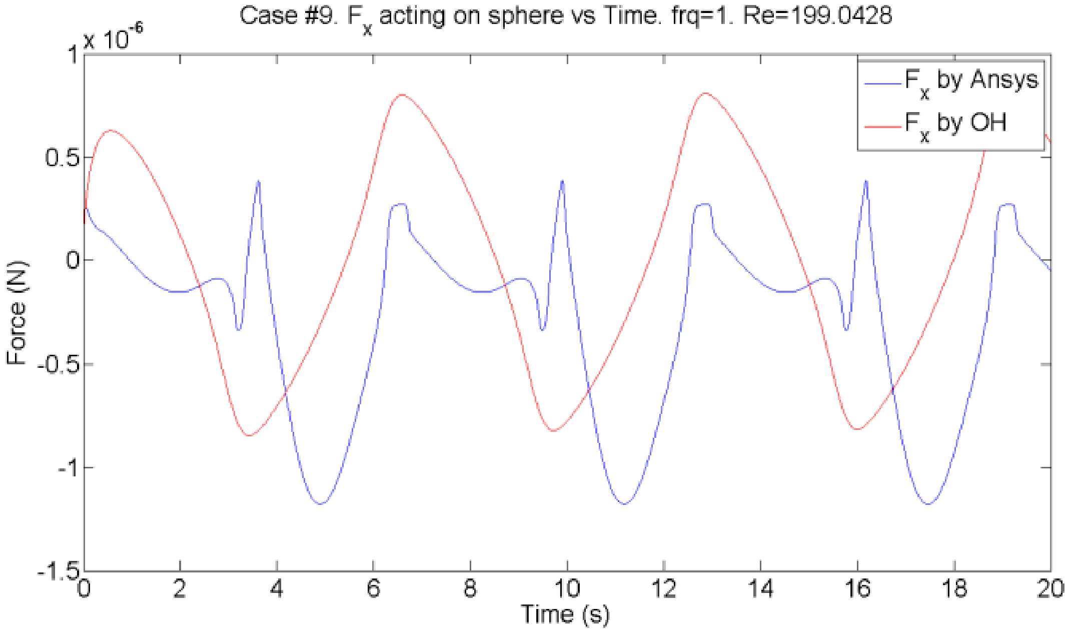

Figure 100: Case 9. $Re = 200. f = 1$ *Hz (original)*

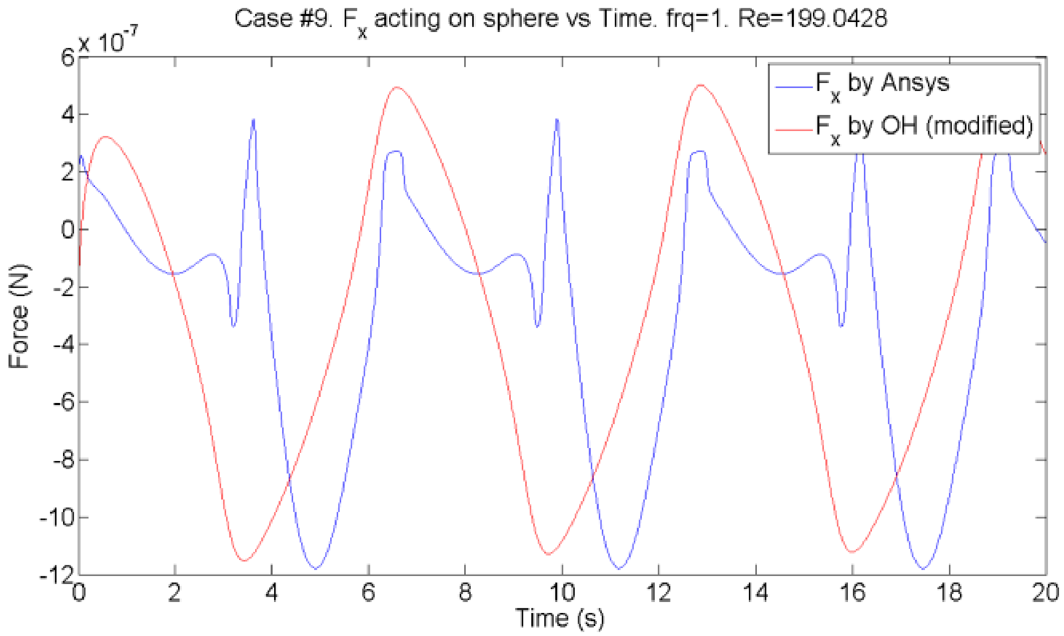

Figure 101: Case 9. $Re = 200. f = 1$ *Hz (modified)*

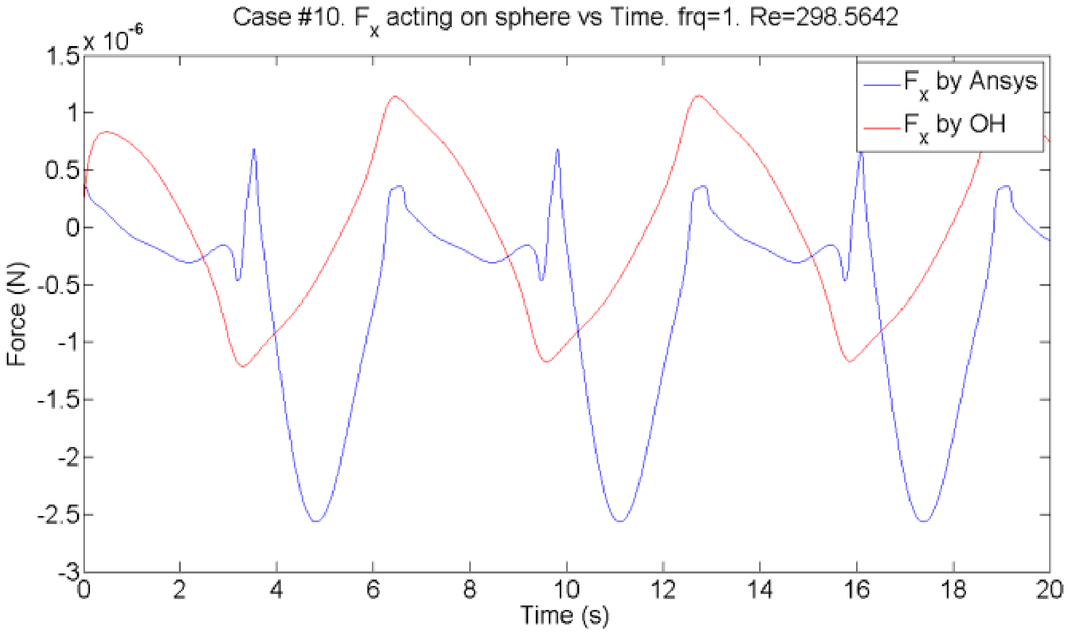

Figure 102: Case 10. $Re = 300. f = 1$ *Hz (original)*

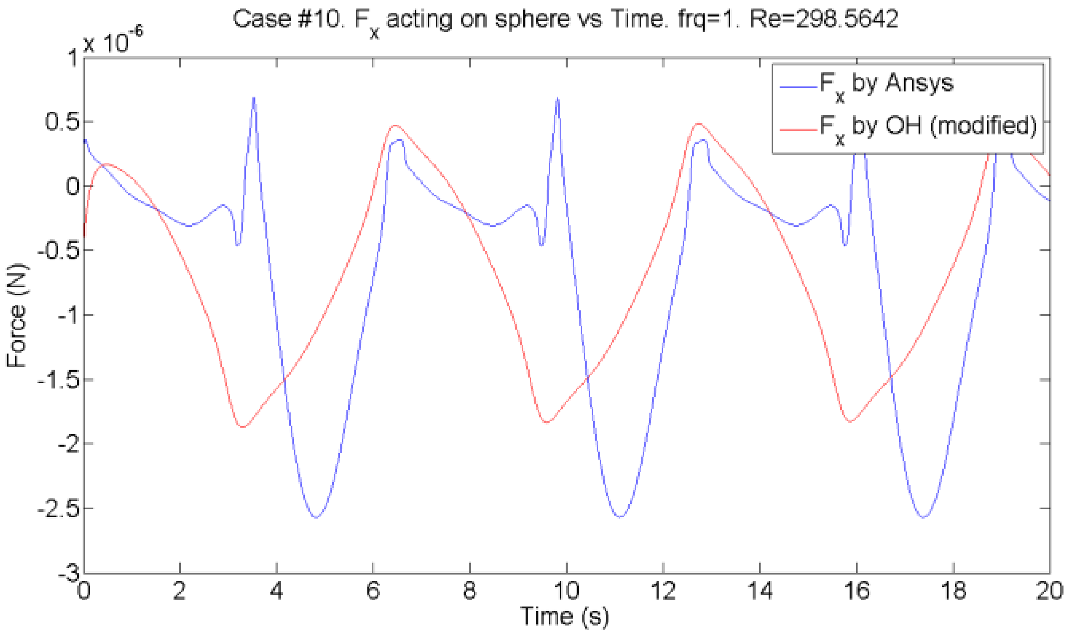

Figure 103: Case 10. $Re = 300. f = 1$ *Hz (modified)*

CONCLUSION

The OH-64 model provides a good approach for the force decomposition of oscillating flow over a particle even for moderate Re flows (up to $\mathrm{Re} < 300$). However, there is a potential field for correction terms derivation. Moreover, the OH-64 model does not accommodate the effects from vorticity, flow separation and wake region formation that start in the flow when $\mathrm{Re} > 24$. One of the ways to analyze and quantify such effects was proposed as to use the hysteresis concept. Also, a correction for the F_x term (and thus for the total force) that depends on the Reynolds number was developed from the power fit for the average F_x difference between ANSYS Fluent© and OH-64. Although, the F_x term can be corrected, in general it was observed that the contribution from the F_x term is less than 10% for most of the cases and thus the main contributor (and the most important force term) to the total force acting on the particle is the drag force.

NOMENCLATURE

Ac	Acceleration number
F_x	Combination of forces excluding drag
S_m	Continuity equation source term
ρ	Density of the fluid
C_D	Drag coefficient
F_{drag}	Drag force
f	Frequency
$F_{history}$	History force (Basset force)
C_H	History force coefficient
i	Index for current time step
t'	Integral variable
Kn	Knudsen number
Φ	Momentum equation source term
N-S	Navier-Stokes equation
OH-64	Odar and Hamilton model
R	Radius of the sphere
Re	Reynolds number
x_i, x_j	Spatial direction
T	Time
F_{total}	Total force acting on a sphere
U	velocity magnitude
u_i	Velocity of the fluid
v_i	velocity of the particle

C_A	Virtual mass coefficient (added mass coefficient)
$F_{virtual\ mass}$	Virtual mass force (added mass force)
μ	Viscosity of the fluid

BIOGRAPHICAL SKETCH

This thesis was written by Aibek Bekkulov. Graduated in 2016 from the University of Leeds (United Kingdom) with a Bachelor of Engineering in mechanical engineering (BEng, 1st class honours). Entered a master's in mechanical engineering program at University of Texas Rio Grande Valley in 2017 and graduating in May 2019. In the past, had two summer internships in his home country – Kazakhstan. One internship was with Eurocopter - Kazakhstan Engineering, a joint venture of Airbus helicopters and Kazakhstan Engineering state company. Another internship was with Institute of Space Techniques and Technology, affiliate of the National Space Agency of the Republic of Kazakhstan. Also, was certified by the Texas Board of Professional Engineers with the title Engineer-In-Training within the State of Texas.

The author published/submitted two conference papers during his research (2017-2019):

1. Bekkulov, A., Xu, B., & Luthen, A. "Experimental study of condensation in different 3d printed regenerators in a thermoacoustic cooler." *ASME 2019 13th International Conference on Energy Sustainability 2019* (under review, submitted in January 2019).

2. Bekkulov, A., Huang, S., Xu, B. "Force Decomposition of Medium Reynolds Number Oscillating Flow Over a Submerged Sphere." ASME International Mechanical Engineering Congress and Exposition, Volume 7: Fluids Engineering. V007T09A032. doi:10.1115/IMECE2018-88187.

Email: bekkulov@gmail.com

Tel: (956) 530-7317